LUND UNIVERSITY

Spatiotemporal imaging of development, disease and regeneration using advanced light-based techniques

Gvazava, Nika

2026

Document Version:
Publisher's PDF, also known as Version of record

Link to publication

Citation for published version (APA):
Gvazava, N. (2026). *Spatiotemporal imaging of development, disease and regeneration using advanced light-based techniques*. [Doctoral Thesis (compilation), Department of Experimental Medical Science]. Lund University, Faculty of Medicine.

Total number of authors:
1

Creative Commons License:
CC BY-NC

General rights
Unless other specific re-use rights are stated the following general rights apply:
Copyright and moral rights for the publications made accessible in the public portal are retained by the authors and/or other copyright owners and it is a condition of accessing publications that users recognise and abide by the legal requirements associated with these rights.
• Users may download and print one copy of any publication from the public portal for the purpose of private study or research.
• You may not further distribute the material or use it for any profit-making activity or commercial gain
• You may freely distribute the URL identifying the publication in the public portal

Read more about Creative commons licenses: https://creativecommons.org/licenses/

Take down policy
If you believe that this document breaches copyright please contact us providing details, and we will remove access to the work immediately and investigate your claim.

LUND UNIVERSITY

PO Box 117
221 00 Lund
+46 46-222 00 00

Download date: 09. Oct. 2026

Spatiotemporal imaging of development, disease and regeneration using advanced light-based techniques

NIKA GVAZAVA
DEPARTMENT OF EXPERIMENTAL MEDICINE | FACULTY OF MEDICINE | LUND UNIVERSITY

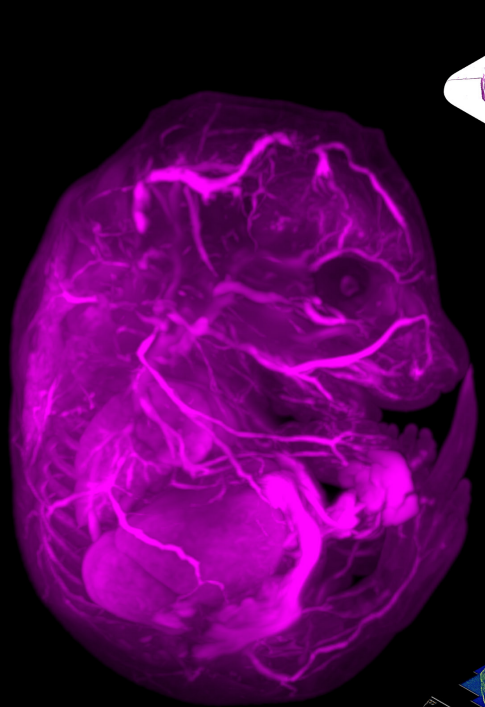

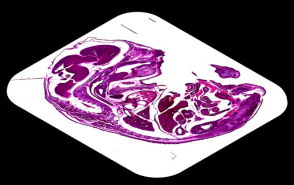

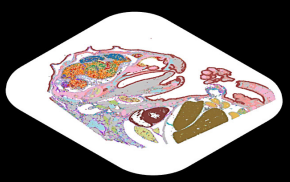

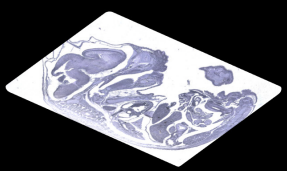

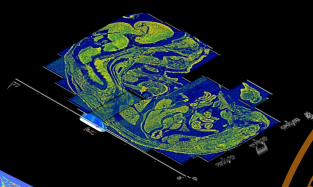

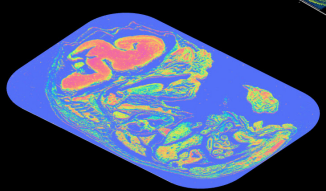

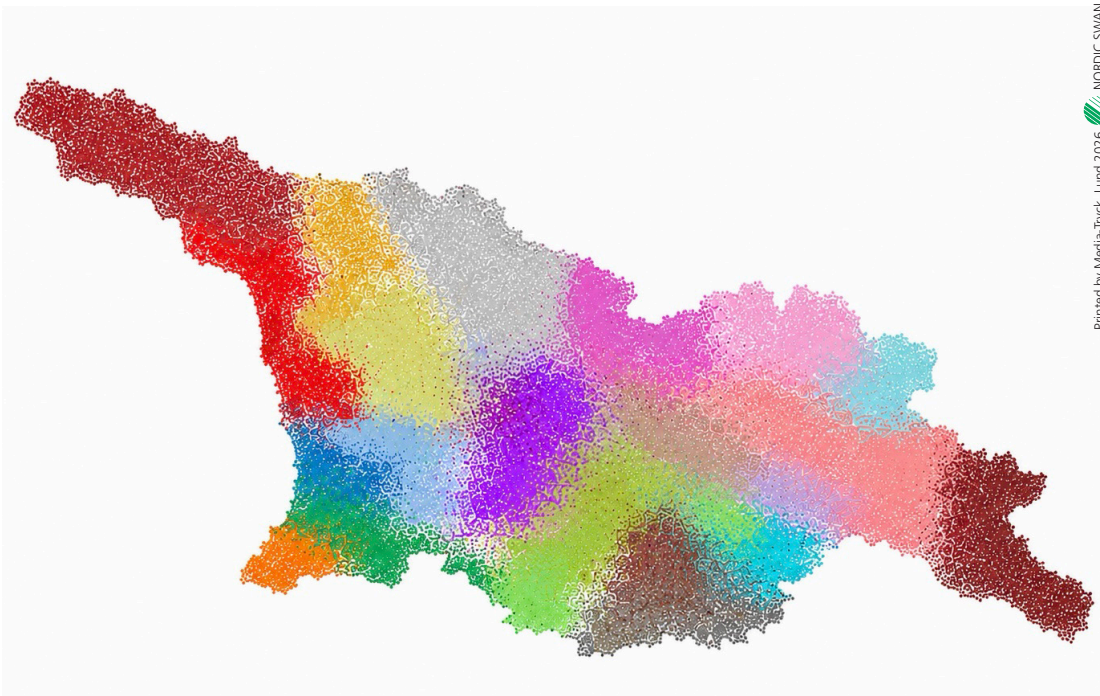

”შენა ხარ ჩემი ჯილდოც, სასჯელიც.
გულზე ახლოს ხარ და ღმერთზე ზემოთ,
ჩემო ტანჯულო, ჩემო მტანჯველო,
დაულეველო სამშობლოვ ჩემო.
შენთან ვარ, მაგრამ მაინც დაგეძებ,
როგორც დაეძებს საჭმელს მშიერი,
და ამ პატარა მიწის ნაგლეჯზე
შემაძრწუნებლად ვარ ბედნიერი”.
ოთარ ჭილაძე

”You are my greatest blessing and my deepest punishment.
You live close to my heart yet stand above God.
My wounded homeland,
my beloved tormentor,
my endless, unquenchable thirst.
I am with you, yet I am forever searching for you,
the way a starving man searches for bread.
And here, upon this little piece of earth, I am terrifyingly happy.”
Otar Chiladze

Printed by Media-Tryck, Lund 2026 NORDIC SWAN ECOLABEL 3041 0903

LUND UNIVERSITY
FACULTY OF MEDICINE

Department of Experimental Medicine

Lund University, Faculty of Medicine
Doctoral Dissertation Series 2026:115
ISBN 978-91-8021-913-6
ISSN 1652-8220

Spatiotemporal imaging of development, disease and regeneration using advanced light-based techniques

Spatiotemporal imaging of development, disease and regeneration using advanced light-based techniques

Nika Gvazava

LUND
UNIVERSITY

DOCTORAL DISSERTATION

By the permission of the Faculty of Medicine, Lund University, Sweden

To be publicly defended in Segerfalksalen A10 Biomedicum Centurm (BMC)

on September 17th at 09.00

Faculty opponent

Charlotte H. Dean, PhD

Imperial Collage London, the United Kingdom (UK)

Organization: LUND UNIVERSITY

Document name: Doctoral dissertation **Date of issue**

Author(s): Nika Gvazava **Sponsoring organization:**

Title and subtitle: Spatiotemporal imaging of development, disease and regeneration using advanced light-based techniques

Abstract: Biological tissues are complex, dynamic and inherently three-dimensional systems whose physiological and anatomical organization is shaped by their native structural and molecular context. Recent advances in three-dimensional and label-free imaging are transforming our ability to interrogate complex biological specimens across molecular, cellular, and organ scales. However, many conventional imaging workflows can disrupt native tissue architecture and obscure transient or physiologically relevant molecular states.

In this thesis, we first explored novel optical photothermal infrared spectroscopy (O-PTIR) as a label-free chemical imaging platform for the analysis of biological specimens under native conditions. We found that O-PTIR enables submicrometer infrared spectroscopic imaging of freshly isolated, fully hydrated biopsies from diverse organs which can be chemically analyzed while preserving their native state.We further found that O-PTIR can distinguish between healthy and amyloid plaque regions in fully hydrated brain slices from APP/PS1 mice. Moreover, O-PTIR enabled molecular imaging of living small vertebrate organisms without compromising their subsequent development, highlighting its potential for non-destructive, in situ chemical imaging of living biological systems.

Further in this thesis, to address key limitations of solvent-based tissue clearing techniques, we developed PROTEUS, a novel solvent-based forward and reverse optical clearing methodology which enables transitioning whole organs in and out of light sheet fluorescence microscopy (LSFM) refractive index matching solutions to enable their use with other standard and state of the art imaging modalities. We demonstrate that PROTEUS preserves endogenous fluorescent proteins, known to be challenging with organic solvent based clearing, as well as other diverse fluorescent molecular probes. This is exemplified in murine brains, transplanted blood vessels and developing murine and chick embryos.

Together, the work presented in this thesis advances two complementary strategies for interrogating biological systems in their native three-dimensional context. O-PTIR provides label-free, submicrometer chemical imaging of hydrated living tissues and organisms, while PROTEUS enables reversible optical clearing of intact organs and embryos for three-dimensional fluorescence imaging followed by downstream multimodal analysis. Collectively, these approaches expand the capacity to extract structural, spatial and chemical information from complex biological specimens and provide a foundation for more integrated and physiologically relevant analysis of tissues in development, homeostasis and disease.

Key words: O-PTIR, Tissue clearing, Alzheimer's disease, Idiopathic pulmonary fibrosis, Light-sheet Flourescence Microscopy

Classification system and/or index terms (if any) Supplementary bibliographical information

Language English **Number of pages**:159

ISSN and key title: **1652-8220**

ISBN: 978-91-8021-913-6

Recipient's notes Price Security classification

I, the undersigned, being the copyright owner of the abstract of the above-mentioned dissertation, hereby grant to all reference sources permission to publish and disseminate the abstract of the above-mentioned dissertation.

Signature Date 2026-08-08

Spatiotemporal imaging of development, disease and regeneration using advanced light-based techniques

Nika Gvazava

LUND
UNIVERSITY

Cover photo by Nika Gvazava (author)

The front image of the thesis cover features an E15.5 mouse embryo, highlighting the multimodal imaging modalities applied to the same specimen. The back image is a map of Georgia created using Microsoft Copilot under supervision, with a design inspired by MERFISH UMAP visualizations of cell-type distributions in the E15.5 mouse embryo, as shown in Figure 59 of this thesis.

Copyright pp 1-159 by Nika Gvazava (author)

Paper 1 © Journal of the American Chemical Society

Paper 2 © American Journal of Physiology

Paper 3 © by the Authors (Manuscript unpublished)

Faculty Of Medicine

Department of Experimental Medical Science

Doctoral Dissertation Series 2026:115

ISBN 978-91-8021-913-6

ISSN 1652-8220

Printed in Sweden by Media-Tryck, Lund University

Lund 2026

Media-Tryck is a Nordic Swan Ecolabel certified provider of printed material. Read more about our environmental work at www.mediatryck.lu.se

MADE IN SWEDEN

Dedicated to my grandparents and parents

ვუძღვნი ჩემს ბებია-ბაბუებს და მშობლებს

Table of Contents

List of publications **11**
Publications included in the thesis 11
Publications not included in the thesis 12
Author's note **14**
Popular science summary **15**
Populärvetenskapling sammanfattning **16**
თეზისის შეჯამება ქართულად **17**
Abstract **19**
Acknowledgements **20**
Key abbreviations **23**
Introduction **24**
Histology: The Architecture of Life and the Baseline for Disease 24
Histology of the lower respiratory system 25
Pathology - the story of disease 28
Idiopathic Pulmonary Fibrosis (IPF) 28
Alzheimer's Disease 32
Organotypic tissue slices 34
Brain tissue slices 34
Precision-Cut Lung Slices (PCLS) 36
Cell Death 40
Apoptosis 42
Escape from Apoptosis 44
Anastasis – living beyond the death 44
Tissue analysis with light-based techniques 45
Light-based microscopy 46

Light Microscopy 47
Fluorescence 47
Fluorescent imaging 49
Resolution 49
Endogenous fluorescent proteins 50
Microscope Selection 51
Tissue Fixation 54
Tissue processing 56
Imaging Thick Tissue 57
Tissue clearing 60
Solvent-based tissue clearing 61
Spectroscopy 62
Ultraviolet–Visible (UV–Vis) Spectroscopy 63
Infrared (IR) spectroscopy 64
O-PTIR 67
Research Aims of the thesis 69
Methodology 70
Animal Models 70
Murine embryos 73
Chicken embryos 74
Human tissue 74
PCLS Generation 74
NucView® 488 & RedDot™ 2 Staining 75
Live imaging 76
Quantification of Apoptosis and Cellular Membrane Damage 77
Water-Soluble Tetrazolium Salt Assay 77
Lactate Dehydrogenase Release 78
O-PTIR 78
eGFP tissue phantom dehydration 79
PROTEUS tissue clearing 80
Light-sheet Fluorescence Microscopy 80
Three-dimensional (3D) volume rendering 81
Deconvolution 81
PCLS generation for Assessment of Archival Formalin Fixed and Paraffin Embedded Samples 82
Reverse optical clearing 84

Agarose/gelatin tissue phantoms for reverse optical clearing and FTIR measurement 84
MERFISH 85
Statistical analysis 86
Use of AI in this thesis 86
Key Results and Discussion 87
O-PTIR can be used in hydrated tissue biopsies and the spectra obtained differs between tissues 88
O-PTIR can distinguish between normal and diseased tissue 89
Local tissue level damage in biopsy punches following O-PTIR imaging 91
Tracking cellular damage after O-PTIR imaging in acute brain slices 93
In Vivo O-PTIR Imaging of *Pleurodeles waltl* Embryo 95
Cellular damage after vibratome sectioning of PCLS 97
Live tracking of cellular damage in precision-cut lung slices (PCLS) following O-PTIR imaging 104
Imaging complex and intricate tissue structures can be achieved using PROTEUS 118
PROTEUS clearing of tissue heterogeneous Early-stage embryos can be achieved 123
PROTEUS is compatible with archival formalin fixed and paraffin embedded tissues 125
Reverse optical clearing preserves chemical, protein and RNA composition for detection 128
Multimodal imaging and spectroscopic analysis of mouse ROC-treated embryos is possible. 131
Conclusions and Future perspectives 137
References 144

List of publications

Publications included in the thesis

Paper I: Nika Gvazava, Sabine Konings, Efrain Cepeda-Prado, Valeriia Skoryk, Chimezie Umeano, Jiao Dong, Iran Augusto Nevas da Silva, Daniella Rylander Ottosson, Nicholas Leigh, Darcy E. Wagner and Oxana Klementieva. **Label-Free High-Resolution Photothermal Optical Infrared Spectroscopy for Spatiotemporal Chemical Analysis in Fresh, Hydrated Living Tissues and Embryos.** *Journal of the American Chemical Society, 2023; 145 (45), 24796-24808*

Paper II: Joanna Nowakowska, Nika Gvazava, Wojciech Langwiński, Kamil Ziarniak, Iran Augusto Nevas da Silva, John Stegmayr, Darcy E. Wagner and Aleksandra Szczepankiewicz. **Optimizing miRNA transfection for screening in precision cut lung slices** *American Journal of Physiology-Lung Cellular and Molecular Physiology, 2024; 327:5, L712-L723*

Paper III: Nika Gvazava, Leonor Simoes, Iran Augusto Neves Da Silva, Angela Zhou, Guillermo Pascual Hellmann, Irakli Nebieridze1, Sondos Odeh, Hannah Swick, Raquel Martinez Curiel, Sara Palma-Tortosa, Kinga Gawlik, Ferenc Borondics, Valerii Skoryk, Sima Babayeva, John Stegmayr, Johan Bengzon, Sabah Hussain, Elena Torban, Sofie Mohlin, Madeleine Durbeej-Hjalt, Zaal Kokaia, Sara S Nunes, Oxana Klementieva, Maia Kokoeva, Darcy E. Wagner. **PROTEUS: organic solvent based forward and reverse optical tissue clearing to preserve endogenous fluorescence and enable multimodal imaging of cleared tissue samples** *(Manuscript)*

Publications not included in the thesis

1. D. E. Wagner, H. N. Alsafadi, N. Mitash, A. Justet, Q. Hu, R. Pineda, C. Staab-Weijnitz, M. Korfei, N. Gvazava, K.Wannemo, U. Onwuka, M. Mozurak, A. Estrada-Bernal, J. Cala-Garcia, K. Mutze, R. Costa, D. Bölükbas, J. Stegmayr, W. Skronska-Wasek, S. Klee, C. Ota, H. A Baarsma, J.Wang, J.Sembrat, A. Hilgendorff, J. Ding, A. Günther, R. Chambers, I. Rosas, S. de Langhe, N. Kaminski, M. Lehmann, O. Eickelberg, M. Königshoff. **Inhibition of epithelial cell YAP-TEAD/LOX signaling attenuates pulmonary fibrosis in preclinical models.** *Nature Communications, 2025 16(1), p.7099.*

2. Gawlik KI, Bölükbas DA, Daoud F, Peruzzi N, Welinder E, Wendt TS, Martinez MA, Tas S, Holmberg J, Gvazava N, Ansar S., Albinsson S., Wagner D., Swärd K., Tran-Lundmark K., Durbeej M. **Laminin γ1 chain is essential for the cardiorespiratory and muscular systems.** *Matrix Biology, 2025, 141, pp.47-66.*

3. P. Prabhala, S. Freiman, N. Gvazava, J. Sharma, S. Wijk, K. Kanzenbach, S. Lang, R. Cattani, J. Wigén, D. Bryder, S. Soneji, J. Flygare, E. Tufvesson, L. Bjermer, D. Wagner, G. Westergren Thorsson, M. Magnusson. **Transcriptional Roadmap of the Human Airway Epithelium Identifying HLF as a Novel Regulator of Basal Stem Cell Function.** *bioRxiv, 2025*

4. N. Silva, S. Kazemi Rashed, L. Hedlund, A. Lidfeldt, N. Gvazava, J. Stegmayr, V. Skoryk, S. Aits, D. Wagner. **Deep learning for rapid and reproducible histology scoring of lung injury in a porcine model**. bioRxiv, 2023

5. Da Silva, N. Gvazava, I. P. Wendi, R. Guinea, F. García Giménez, J. Stegmayr, O. Klementieva, D. E. Wagner. **Formalin-free fixation and xylene-free tissue processing preserves cell-hydrogel interactions for histological evaluation of 3D calcium alginate tissue engineered constructs.** Frontiers in Biomaterials Science, 2023, 43(2), pp.290-303

6. Da Silva, N. Gvazava, D. Bölükbas, M. Stenlo, J. Dong, S. Hyllen, L. Pierre, S. Lindstedt, D. Wagner. **A Semi-quantitative Scoring System for Green Histopathological Evaluation of Large Animal Models of Acute Lung Injury**. *BIO-PROTOCOL, 2022, 12 (16), e4493-e4493*

7. H. Ghaidan, M. Stenlo, A. Niroomand, M. Mittendorfer, G. Hirdman, N. Gvazava, D. Edström, I. A. N. Silva, E. Broberg, O. Hallgren, F. Olm, D. E. Wagner, L. Pierre, S. Hyllén, S. Lindstedt. **Reduction of primary graft dysfunction using cytokine adsorption during organ preservation and after lung transplantation.** Nature Communications, 2022, 13(1), p.4173

8. H. N. Alsafadi, V. Ptasinski, N. Gvazava, I. A. N. Silva, I. Tamargo, E. Rehnberg, T. Volckaert, B. Lindberg, A. Borde, D. E. Wagner, J. Stegmayr**. inFLATION: Infusion of Fluorescently Labelled Antibodies in Tissue of Intact Organs for Visualization of the Rodent Lung Using Light-Sheet Fluorescence Microscopy**. (Manuscript in preparation)

Author's note

As a child, I was always curious about how everything was made. As a consequence, there were many broken toys, ripped teddy bears and a patience from my parents, grandparents and everyone around.

In elementary school, I became fascinated by the perfectly structured cells of an onion. I asked my parents for a microscope and my uncle gladly gave me his own single-ocular light microscope. Since then, I have never left microscopy behind.

Later, during medical school, I worked in the departments of histology, pathology and forensic medicine. Eventually, moved to Sweden with very limited research experience, first joining Zaza Kokaia's lab and then Darcy Wagner's lab as a research assistant. It quickly became clear that I had to learn fast and catch up with scientific advances. At the same time, I realized that, unconsciously, I was always interested about the rationale behind how everything works, that's what led me to pursue a PhD.

This thesis is a summary of years of work. I was very fortunate that my PhD projects were highly interdisciplinary and I am deeply grateful for that. It pushed me to learn across a broad spectrum of fields, ranging from physics to drug discovery. Most importantly, however, it taught me the value of collaboration and interaction with scientists from different disciplines. I have never regretted my choices, in fact, I would make the same ones again.

Looking back, life has not been linear. There have been many ups and downs, sometimes even hurricane and turbulence, but there has always been hope! Hope for a better future!

While writing this thesis, I realized that I am still the same person, only with a little more knowledge, but still with millions of unanswered questions.

Popular science summary

Traditional histopathological assessment of tissue has generated enormous breakthroughs in both biomedical research and clinical diagnostics. For more than a century, thin tissue sections stained and examined under the microscope have formed the foundation of how we understand tissue architecture, development, classify pathological changes and identify disease. Yet, despite their enormous value, traditional histological methods usually look at tissue as a series of 2D sections. However, given the three-dimensional nature of organisms, studying and understanding biological systems requires approaches that preserves their native spatial organization. This is especially important when studying developmental processes, heterogeneous diseases, tissue remodelling and repair.

In recent years, multimodal tissue analysis has emerged as a powerful strategy to extract the maximum possible information from a single biological sample. Instead of using one specimen for one method, the same sample can be studied with several complementary technologies. This approach is particularly valuable when sample material is limited, when spatial registration between modalities is essential, or when structural, molecular and chemical information must be obtained and integrated to understand complex biological phenomena.

However, the rapid development of new imaging and tissue analytical techniques also creates an important challenge, each method must be carefully validated for compatibility with tissue or other methods.

This thesis explores new ways to study biological samples using advanced light-based imaging and analytical methods from both the visible and infrared regions of the electromagnetic spectrum. The overall goal is to analyze tissues and organisms as close as possible to their native state, while preserving their three-dimensional structure, molecular information and compatibility with additional imaging or downstream analysis methods. By combining complementary approaches, this work contributes to a broader shift in biomedical research, by moving beyond 2D flat tissue slides, single-method tissue analysis toward integrated, multidimensional investigation of intact biological samples.

Populärvetenskapling sammanfattning

Traditionell histopatologisk bedömning av vävnad har lett till enorma genombrott inom både biomedicinsk forskning och klinisk diagnostik. I mer än ett sekel har tunna vävnadssnitt, färgade och undersökta i mikroskop, utgjort grunden för hur vi förstår vävnadsarkitektur och utveckling, klassificerar patologiska förändringar och identifierar sjukdomar. Trots deras stora betydelse betraktar traditionella histologiska metoder vanligtvis vävnad som en serie tvådimensionella snitt.

Organismer är emellertid i grunden tredimensionella. Därför kräver en heltäckande förståelse av komplexa biologiska systemanalys av organ, eller till och med hela kroppar, i ett tredimensionellt sammanhang och i deras naturliga tillstånd. Detta är särskilt viktigt vid studier av utvecklingsprocesser, heterogena sjukdomar samt vävnadsremodellering och reparation.

Under de senaste åren har multimodal vävnadsanalys vuxit fram som en kraftfull strategi för att extrahera största möjliga mängd information från ett enda biologiskt prov. I stället för att använda ett prov för en enda metod kan samma prov studeras med flera kompletterande teknologier. Detta tillvägagångssätt är särskilt värdefullt när provmaterialet är begränsat, när spatial registrering mellan olika modaliteter är avgörande, eller när strukturell, molekylär och kemisk information måste erhållas och integreras för att förstå komplexa biologiska fenomen.

Den snabba utvecklingen av nya avbildnings- och vävnadsanalytiska tekniker skapar dock också en viktig utmaning: varje metod måste noggrant valideras för kompatibilitet med vävnaden och med andra metoder.

Denna avhandling utforskar nya sätt att studera biologiska prover med hjälp av avancerade ljusbaserade avbildnings- och analysmetoder från både de synliga och infraröda delarna av det elektromagnetiska spektrumet. Det övergripande målet är att analysera vävnader och organismer så nära deras naturliga tillstånd som möjligt, samtidigt som deras tredimensionella struktur, molekylära information och kompatibilitet med ytterligare avbildnings- eller efterföljande analysmetoder bevaras. Genom att kombinera kompletterande tillvägagångssätt bidrar detta arbete till en bredare förändring inom biomedicinsk forskning: att gå bortom platta tvådimensionella vävnadssnitt och enskilda analysmetoder, mot en integrerad och multidimensionell undersökning av intakta biologiska prover.

თეზისის შეჯამება ქართულად

ქსოვილის ტრადიციულმა ჰისტოპათოლოგიურმა შეფასებამ უდიდესი წინსვლა და სიახლე მოიტანა როგორც ბიოსამედიცინო კვლევაში, ისე კლინიკურ დიაგნოსტიკაში. საუკუნეზე მეტი ხნის განმავლობაში, მიკროსკოპის ქვეშ შეღებილი და შესწავლილი თხელი ქსოვილოვანი ანათლები წარმოადგენდა საფუძველს იმის გასარკვევად, თუ როგორ ვიგებთ/ ვადგენთ ქსოვილის არქიტექტურას, განვითარებას, როგორ ვახდენთ პათოლოგიური ცვლილებების კლასიფიკაციას და დაავადებების იდენტიფიცირებას. თუმცა, მიუხედავად მათი უზარმაზარი მნიშვნელობისა, ტრადიციული ჰისტოლოგიური მეთოდები ქსოვილს, როგორც წესი, განიხილავს ორგანზომილებიანი ანათლების სერიად.

ამასთან, ორგანიზმები ბუნებით სამგანზომილებიანია. შესაბამისად, რთული ბიოლოგიური სისტემების სრულყოფილი გაგება მოითხოვს ორგანოების ან, ზოგ შემთხვევაში,მთელი ორგანიზმ(ებ)ის სამგანზომილებიან კონტექსტსა და მათ ბუნებრივ მდგომარეობასთან მაქსიმალურად მიახლოებულ პირობებში ანალიზს. ეს განსაკუთრებით მნიშვნელოვანია განვითარების პროცესების, ჰეტეროგენული დაავადებების, ქსოვილის რემოდელირებისა და აღდგენის შესწავლისას.

ბოლო წლებში მულტიმოდალური ქსოვილოვანი ანალიზი ჩამოყალიბდა როგორც ძლიერი სტრატეგია, რომელიც ერთი ბიოლოგიური ნიმუშიდან მაქსიმალურად დიდი რაოდენობის ინფორმაციის მიღების საშუალებას იძლევა. ერთი ნიმუშის ასევე ერთი მეთოდისთვის გამოყენების ნაცვლად, იგივე ნიმუში შეიძლება შესწავლილ იქნას რამდენიმე ურთიერთშემავსებელი ტექნოლოგიით. ეს მიდგომა განსაკუთრებით ღირებულია მაშინ, როდესაც ნიმუშის რაოდენობა შეზღუდულია, როდესაც სხვადასხვა მოდალობას შორის სივრცითი თანხვედრა აუცილებელია ან როდესაც რთული ბიოლოგიური ფენომენების გასაგებად საჭიროა სტრუქტურული, მოლეკულური და ქიმიური ინფორმაციის ინტეგრირება.

თუმცა, ახალი ვიზუალიზაციისა და ქსოვილის ანალიზის მეთოდების სწრაფი განვითარება მნიშვნელოვან გამოწვევასაც ქმნის: თითოეული მეთოდი გულდასმით უნდა შემოწმდეს ქსოვილთან ან სხვა მეთოდებთან თავსებადობის თვალსაზრისით.

ეს დისერტაცია იკვლევს ბიოლოგიური ნიმუშების შესწავლის ახალ გზებს, ელექტრომაგნიტური სპექტრის როგორც ხილული, ისე ინფრაწითელი რეგიონებიდან მომდინარე, სინათლეზე დაფუძნებული მოწინავე ვიზუალიზაციისა და ანალიტიკური მეთოდების გამოყენებით. ძირითადი მიზანია ქსოვილებისა და ორგანიზმების ანალიზი მათ ბუნებრივ მდგომარეობასთან მაქსიმალურად მიახლოებულ პირობებში, მათი სამგანზომილებიანი სტრუქტურის, მოლეკულური ინფორმაციისა და დამატებით ვიზუალიზაციის ან შემდგომი ანალიზის მეთოდებთან თავსებადობის შენარჩუნებით. ურთიერთშემავსებელი მიდგომების გაერთიანებით, ეს ნაშრომი ხელს უწყობს ბიოსამედიცინო ვიზუალიზაციაში უფრო ფართო ცვლილებას: გზას გვიკაფავს ბრტყელი, ერთმეთოდიანი ქსოვილოვანი ანალიზიდან ინტეგრირებული, მრავალგანზომილებიანი კვლევისკენ, რომელიც უცვლელი ბიოლოგიური სისტემების შესწავლას ეფუძნება.

Abstract

Biological tissues are complex, dynamic and inherently three-dimensional systems whose physiological and anatomical organization is shaped by their native structural and molecular context. Recent advances in three-dimensional and label-free imaging are transforming our ability to interrogate complex biological specimens across molecular, cellular, and organ scales. However, many conventional imaging workflows can disrupt native tissue architecture and obscure transient or physiologically relevant molecular states.

In this thesis, we first explored novel optical photothermal infrared spectroscopy (O-PTIR) as a label-free chemical imaging platform for the analysis of biological specimens under native conditions. We found that O-PTIR enables submicrometer infrared spectroscopic imaging of freshly isolated, fully hydrated biopsies from diverse organs which can be chemically analyzed while preserving their native state. We further found that O-PTIR can distinguish between healthy and amyloid plaque regions in fully hydrated brain slices from APP/PS1 mice. Moreover, O-PTIR enabled molecular imaging of living small vertebrate organisms without compromising their subsequent development, highlighting its potential for non-destructive, in situ chemical imaging of living biological systems.

Further in this thesis, to address key limitations of solvent-based tissue clearing techniques, we developed PROTEUS, a novel solvent-based forward and reverse optical clearing methodology which enables transitioning whole organs in and out of light sheet fluorescence microscopy (LSFM) refractive index matching solutions to enable their use with other standard and state of the art imaging modalities. We demonstrate that PROTEUS preserves endogenous fluorescent proteins, known to be challenging with organic solvent-based clearing, as well as other diverse fluorescent molecular probes. This is exemplified in murine brains, transplanted blood vessels and developing murine and chick embryos.

Together, the work presented in this thesis advances two complementary strategies for interrogating biological systems in their native three-dimensional context. O-PTIR provides label-free, submicrometer chemical imaging of hydrated living tissues and organisms, while PROTEUS enables reversible optical clearing of intact organs and embryos for three-dimensional fluorescence imaging followed by downstream multimodal analysis. Collectively, these approaches expand the capacity to extract structural, spatial and chemical information from complex biological specimens and provide a foundation for more integrated and physiologically relevant analysis of tissues in development, homeostasis and disease.

Acknowledgements

I would like to begin this thesis with acknowledgement. I truly believe that nothing in life happens without purpose. Every person we meet, every challenge we face, and every joy we experience shapes who we become. This journey has never been mine alone, it has been built on love, patience, mentorship, friendship and belief.

First, I would like to thank my parents and grandparents (especially my grandmother **Natalia**), who raised me with unconditional love, engraved in me the values of respect, hard work and ensured that I had every opportunity to receive an education. Without their sacrifices and devotion, this path would not have been possible. Second, I would like to thank my Scandinavian family**, Zaal Kokaia and Tamara Chikovani**. Since my arrival in Sweden, they have been much more than mentor or friend, you became my family, supporting me through both challenges and successes.

Darcy Wagner- Thank you for your mentorship, for always being on my side (even at 4:00 in the morning during confocal imaging), for believing in me, allowing me to be myself and teaching me how to be a scientist. As I often say, good captains know how to navigate in challenging waters. I truly enjoyed working with you, but what I value most are our scientific discussions. Your curiosity, enthusiasm and passion for science have inspired me throughout this journey. This is not the end, but rather the beginning of a new chapter.

Oxana Klementieva - Thank you for being such a supportive, kind, and productive co-supervisor. I am truly grateful for all the opportunities you have given me and for your guidance throughout this journey.

Hani Alsafadi - Thank you for being my co-supervisor and for teaching me image analysis. I am truly grateful for your guidance, support, and patience throughout this journey. You are a very kind and knowledgeable person, and I have learned a great deal from you.

I would like to sincerely thank all my co-authors for their hard work, dedication and invaluable contributions. I have been fortunate to work alongside such a diverse and talented scientific team. Thank you for generously sharing your knowledge, offering guidance and explanations whenever needed and helping me grow as a researcher.

I would like to thank my opponent - **Charlotte Dean** and committee members: **Alex Evilevitch, Anna Sandström Gerdtsson, Janko Kajtez, Aboma Merdasa, Sandeep Gopal** and my half-time reviewer **Arturo Ibáñez-Fonseca**, for taking the time to review my thesis and publications. I understand the significant effort and time involved in reading and evaluating PhD work, and I truly appreciate your efforts. I am looking forward to our discussion.

Iran Augusto Neves da Silva- thank you for all the moments we have shared throughout this journey and for being annoying. We become not just colleagues but also friends, we

shared many laughs, smiles and unforgettable memories, while also supporting each other through difficult times. It has been truly inspiring to see your development over the years.

John Stegmayr- thank you for being supportive and reliable colleague. I am especially grateful for the time and patience you devoted to teaching me microscopy and tissue clearing.

Valerii Skoryk- thank you for all your help and support throughout this journey. I deeply appreciate your advice, thoughtful guidance, and readiness to lend a helping hand whenever needed.

Shahram Parvaneh- thank you for being such a kind-hearted and truly generous person, a wonderful colleague.

Leonore Tavares De Pina Simeos - thank you for being such a supportive fellow PhD student and for all discussions we have shared over the years. It has been a true privilege to see your development from the bachelor student to becoming a PhD researcher. Your curiosity, dedication and reliability are truly admirable, and I have no doubt that these qualities will continue to lead you to great success.

Indra Putra Wendi - thank you for your thoughtful comments, input and constructive discussions throughout this journey. Special thanks for the many sleepless nights in shared rooms during conferences.

A big thank you to all past and present members of the Lung Bioengineering and Regeneration (LBR) group, on both sides of the Atlantic Ocean, for the warm welcome, friendship and support I received both in Lund and Montreal: **Alfredo Moreno Olmedo, Noelia Redondo Bort, Gaëtan Roudier, Nicholas Vonniessen, Simran Jaffer, Tiago Bressanelli Maffacioli, Guillermo Pascual Hellmann, Deniz Bölükbaş, Sinem Taş, Victoria Ptasinski, Irakli Nebieridze, Martina Saantis** and **Jiao Dong.** A special thank you to **Joelle Hajj** for being such a wonderful person and a supportive colleague. Thank you for the warm welcome during the winter in Montreal.

I would also like to thank all my colleagues from B10, especially **Clair, Sara, Oskar, Alicja, Raquel, Pia** and **Claudia**, for creating such a friendly and supportive working environment. A special thank you to **Emanuella Monni** for teaching me confocal microscopy and generously sharing your expertise, I am deeply grateful for your wise advice, constant support and willingness to help whenever needed.

I would also like to thank everyone at LBIC, and especially to **Sebastian Wasserstrom**, for your support and assistance throughout my PhD journey. A special thank you to **Nils Norlin** for helping me deepen my knowledge of advanced light microscopy. Your expertise, enthusiasm for microscopy and willingness to share your knowledge have been invaluable to my scientific development.

I would also like to express my sincere gratitude to the PhD Student Union at the Faculty of Medicine (MDR), an organization that I had the privilege of chairing for two years. A very special thank you to my two Vice-Chairs, **Juliane Tampe** and **Divya Bali**. Without your commitment, hard work and willingness to take on challenges, our achievements would not have been possible.

Franziska Uhl - thank you for being such a wonderful friend and truly reliable person. Your kindness, generosity and unwavering support have meant so much to me throughout this journey. The world genuinely needs more people like you.

Tania Ramos- Thank you for your friendship, patience, kindness, support and wise advices. **Eduard**- Thank you for bringing light into our lives. I wish you happiness, joy and all the very best in your future life.

Ramaz Chikhladze- Thank you for being an exceptional teacher and mentor. I am deeply grateful for the knowledge, guidance and inspiration you have given me throughout the years and thank you for opening the world of pathology to me**.**

Divya Bali- I want to thank you for being such a wonderful person with a big heart and a kind soul. I also deeply admire how structured and meticulous you are in everything you do. I will never forget your support during some of the hardest times

Kirill- thank you for all your support, patience and understanding during the writing of this thesis. I greatly appreciate it!

I would also like to thank to my Georgian crew and dear friends in Sweden **Temur Potaskaevi, Giorgi Janjalashvili, Natia Gamkrelidze, Nikoloz Bakradze, Ana Solomnishvili, Guga Korkashvili, Aleksandre Oganov, Athanasios Vatalis and Tornike Metreveli** for their unwavering support and friendship throughout this journey**.** A big thanks to all Kokaia Family**: Giorgi, Noemi Schaffer, Marab, Tamara Landia, Givi and Luka**. Special thanks to **Jason**, the most joyful and kind person I know. I would also like to thank my dear friends from Malmö: **Pjetr, Yevgen, Mikhael, Dmitry, Pavel**, and **Fran**, thank you for your friendship, support and for being part of my life. A big thank you to **Karin** for all your support, care, good vibes and for our shared love of Finnish design**. Pavlos**- thank you for the many years of memories, smiles, laughter and care. It meant a great deal to me! I would also like to thank mama Litsa for her warmth and love.

I would like to thank my dear friends**: Giorgi Mikuchadze, Aleksandra Gvenetadze, Mariam Kurashvili, Tamar Katashvili, Giorgi Makhviladze, Davit Kobakhidze, Viviana Bibilashvili,Tamar Matsaberidze, Eko Khomeriki, Mariam Tevzadze, Nino Archvadze, Anano Zazashvili, Giorgi Gorgaslidze and** my childhood friends**: Giorgi Kvinikadze, Temur Nijaradze, Giorgi Kukhalashvili,Natia Tutarashvili,Giorgi Elizbarashvili and Temuri Pantskhava,** for their endless love and support.

To my dear spiritual friends, **Fr. Demetre (Davitashvili), Fr. Gabriel (Batarashvili), Fr. Leonide (Ebralidze), Fr. Saba (Kevlishvili), Fr. Nicodimos (Khvedelidze)** and **Nika Inauri**, thank you for your friendship, prayers, guidance and constant support.

Thank you to my big family, **Gocha, Kristina, Keteva, Shalva, Lela, Maia, Gvantsa**, and my cousins, **Tekla, Tsotne, Atuka, Luka, Zuka**, and **Tamuna,** for their unconditional love and support throughout my life.

During this journey, I had the privilege of meeting many talented and intelligent people through conferences, talks, coffee breaks, and countless discussions. Each of you has taught me something valuable and, in one way or another, helped broaden my knowledge and expertise. Thank you all for being part of this journey!

"Rejoice always, pray without ceasing, give thanks in all circumstances." (1 Thess.5:16-18)

Key abbreviations

Accidental cell death (ACD)
Alveolar epithelial type I cells (AEC1)
Alveolar epithelial type II cells (AEC2)
Amyloid-beta (Aβ)
Amyloid precursor protein (APP)
Confocal laser-scanning microscope (CLSM)
Ethyl Cinnamate (ECi)
Formalin-Fixed Paraffin-Embedded (FFPE)
Glutaraldehyde (GA)
Green fluorescent protein (GFP)
Hematoxylin and Eosin (H&E)
Immunohistochemistry (IHC)
Light-sheet fluorescence microscopy (LSFM)
Optimal cutting temperature (OCT)
Paraformaldehyde (PFA)
Precision-cut lung slices (PCLS)
Programmed cell death (PCD)
Regulated cell death (RCD)
Yellow fluorescent protein (YFP)

Introduction

Histology: The Architecture of Life and the Baseline for Disease

Before we can understand how disease alters a tissue, we must first know how it is built under normal circumstances. Morphology covers the study of tissue across multiple spatial scales, from macroscopical and gross anatomical architecture to the microscopical, intricate cellular and subcellular level. This is the realm of histology, the microscopic study of normal tissue architecture, development and function.

The formal term of "histology" was established by Karl Meyer in 1819, combining the Greek roots histos -tissue and logia-study. However, the conceptual foundation of the discipline was built a century prior when the Italian physician and scientist Marcello Malpighi visualized pulmonary capillaries in frog lungs under a microscope in 1661, validating William Harvey's theory of blood circulation(1). The architectural understanding of the body was then advanced by Marie François Xavier Bichat, who managed to categorize twenty-one distinct tissue types through macroscopic dissection alone in the late 18th century (2). However, later in 1857 Franz Leydig categorized the four fundamental tissue types (epithelial, connective, muscle and nervous), which is still widely accepted (3).

The evolution of histology is inextricably linked to technological advances in science, ranging from the development of tissue staining techniques to major innovations in microscopy and now computational analysis. Traditionally, the baseline for any histological examination relies on the preparation of thin sections of fixed, paraffin-embedded (FFPE) tissue which are then examined under a light microscope. Although these techniques are now routine in clinical and research settings, every step is built on rigorous experimental evidence and prior optimisation, such as the specific fixation times required for different tissue densities (discussed below). Historically, the field advanced through the development of distinct chemical dyes and staining methods e.g. Hematoxylin and Eosin (H&E)(4-6) and Masson's trichrome (7). While often referred to as "basic" stains, they remain the bedrock of clinical diagnosis and pre-clinical research. This morphological foundation was ultimately revolutionized in the latter half of the 20th century by the advent of Immunohistochemistry (IHC) (8-11). By utilizing highly specific antibodies to visualize molecular targets directly within the tissue

architecture, IHC successfully bridged gross morphology with molecular biochemistry.

To demonstrate how perfectly our bodies are built at the microscopic level, with specific niches structurally designed for distinct cell types, the normal histology of the respiratory system will be detailed below as a primary example and I humbly dedicate to the memory of Professor Ewald R. Weibel (12).

Histology of the lower respiratory system

Although the primary role of the respiratory system is gas exchange, it is also a highly dynamic organ network that supports numerous life-sustaining physiological (13, 14), metabolic (15), immunological processes (16-18) and contributes to the maintenance of homeostasis (19). Anatomically, the respiratory system is classically divided into the upper and the lower respiratory tract (**Figure 1**). The upper respiratory tract consists of the nose, nasal cavity, paranasal sinuses, pharynx, and larynx, while the lower respiratory - the trachea, bronchi, bronchioles and the alveolar regions of the lungs.(20, 21). The upper airways play an essential role in conditioning inspired air by warming, humidifying and filtering it before it reaches the distal lung. This region also contains important olfactory sensory neurons, together with ciliated epithelial cells, goblet cells, basal cells and resident immune cells that contribute to first line defence and environmental sensing (21). Recent technological developments, such as single cell sequencing and spatial transcriptomics, have expanded our understanding of the lung as a complex organ made up of more than 40 cell types, which are distributed across distinct anatomical locations and perform specialized functions (22). This thesis focuses primarily on the lower respiratory tract as it is the region of the lung most affected in chronic and acute lung diseases.

After air passes through the larynx, it enters the trachea, which serves as the primary conducting airway of the lungs. At the level of the carina, located approximately at the sternal angle (angle of Louis) and corresponding to the level of the T4-T5 vertebrae, the trachea bifurcates into the right and left main bronchi, which conduct air into the lungs (21, 23). In humans, the lungs are divided into five lobes, with three lobes in the right lung and two lobes in the left lung (24). In order to maintain effective airflow under normal physiological conditions, both the trachea and bronchi must remain open. For this reason, their walls contain cartilage (rings or cartilage plates) that provide structural support and preventing collapse as well as smooth muscle which regulates airway diameter (21).

The trachea and bronchi are lined by a pseudostratified epithelium that forms the first cellular barrier against the external environment. This epithelial layer consists a heterogeneous cellular populations , predominantly of basal cells, secretory cells, goblet and ciliated cells, along with smaller population of specialized cell types such

as tuft cells (brush cells), pulmonary neuroendocrine cells and ionocytes (25, 26). Basal cells are located in the basal layer of the epithelium and serve as resident progenitor cells that maintain and repair the bronchial epithelial lining (27, 28). Secretory cells, including club cells and goblet cells, produce protective factors such as secretoglobins and mucus, which help defend the lung from inhaled particles, pathogens and oxidative stress (29, 30). Ciliated cells are columnar epithelial cells characterized by a dense apical border of microscopic hair-like motile structures projecting into the airway lumen, with highly coordinated, metachronal manner beating at frequency of 10-20 Hz, generating the force required for mucociliary clearance (31). Pulmonary neuroendocrine cells and tuft cells contribute to sensory and immune signalling, whereas ionocytes, which express high levels of ion channels including CFTR, are thought to participate in epithelial ion transport (32-34).

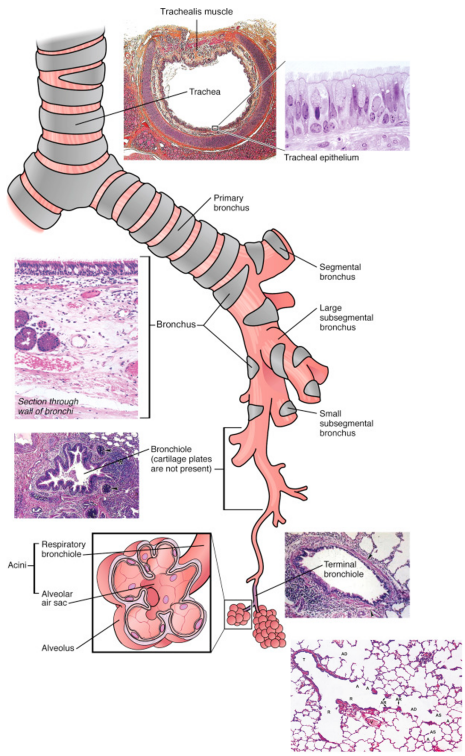

Figure 1. Schematic and representative histological images of major anatomical regions and cell types in lower respiratory tract. Image taken with permission. Figure reproduced from (Carlson *et al*. 2019) with permission.

As they extend into the lung parenchyma, the bronchi divide repeatedly into smaller conducting airways - bronchioles. Approximately 23 generations of branching airways form an extensive and highly organized network in humans to rapidly distribute the air throughout the lungs. Unlike the trachea and bronchi, bronchioles

lack cartilage, which makes their walls more flexible. However, they retain a smooth muscle layer, which becomes particularly important for keeping these airways open in the absence of cartilage. Histologically, the epithelium in the bronchioles is simpler than that of the larger airways and is typically cuboidal, consisting predominantly of secretory cells and ciliated cells. In the human lung, bronchioles can be broadly classified into 1) conducting bronchioles- which primarily serve to transport air and 2) respiratory bronchioles- which represents the transition between the conducting airways and the gas-exchanging regions of the lung (35, 36). The terminal portion of the respiratory system begins where respiratory bronchioles transition into alveolar ducts, which ultimately lead to alveolar sacs. These sacs have a grape-like appearance and contain numerous alveoli (approximately 480 million alveoli in human lungs (37)), which are small (in human 200-300 μm and in mouse 40-80 μm), thin-walled, balloon-like structures closely associated with dense capillary networks (35, 36). The alveoli are the primary sites of gas exchange, allowing oxygen to enter the blood and carbon dioxide to be removed from the circulation.

The alveolar epithelium differs markedly from that of the conducting airways and is composed primarily of alveolar epithelial type I cells (AEC1) and alveolar type II cells (AEC2). AEC1 are simple squamous epithelial cells that form most of the alveolar surface and passively facilitate gas exchange due to how thin they are, whereas AEC2 have a simple cuboidal shape and secrete surfactants, which reduces surface tension and helps prevent alveolar collapse during breathing (38, 39). In addition, AEC2s function as progenitor cells of the alveolar epithelium by self-renewing and giving rise to AEC1 during homeostasis and following injury. The alveolar spaces also contain alveolar macrophages, which serve a critical role in immune defense by clearing inhaled particles and modulating local inflammatory responses (40, 41).

In addition to the airway tree and alveolar compartments, the lungs contain an extensive vascular and lymphatic network which are essential for pulmonary homeostasis (42). While the blood vasculature supports efficient gas exchange, the lymphatic system plays a critical role in maintaining tissue fluid balance, removing excess interstitial fluid and contributing to immune surveillance within the lung (43-45).

Finally, the lungs are surrounded by the pleura, a bilayered serous membrane that encloses them and helps maintain their position within the thoracic cavity. The pleura is lined primarily by mesothelial cells which reside on an underlying connective tissue layer containing fibroblasts, blood vessels, lymphatics and immune cells (46). The pleura consists of two continuous layers: the visceral pleura, which closely covers the surface of the lungs, and the parietal pleura, which lines the inner chest wall, diaphragm, and mediastinum (46). The narrow space between these layers, known as the pleural cavity, contains a thin layer of pleural fluid that

reduces friction during breathing and allows smooth movement of the lungs (46). Surface tension generated by the pleural fluid also helps maintain close apposition between the lungs and the thoracic wall, contributing to lung expansion during inhalation and helping prevent lung collapse (atelectasis) under normal physiological conditions (47).

Pathology - the story of disease

Cells may, for a variety of intrinsic and extrinsic reasons, temporarily or permanently lose their normal function. Such dysfunction can compromise tissue integrity and organ performance, ultimately contributing to the development of disease, as observed in the majority of clinical conditions. Pathology is the discipline that examines the structural, cellular, and molecular alterations underlying abnormal tissue and organ function. It is one of the most important fields in diagnostic medicine because many diseases display characteristic morphological features that can be readily recognized in tissue sections. Histopathological evaluation of biopsy or surgical resection specimens often provides the definitive diagnosis for a wide range of disease such as cancer and fibrosis but also inflammatory, infectious, and degenerative disorders. Beyond establishing a diagnosis, pathology also plays a central role in determining prognosis and guiding treatment by providing information on features such as tumour grade, disease stage, resection margin status, and the expression of clinically relevant molecular biomarkers. Moreover, the integration of high-throughput molecular data with traditional morphological assessment is increasingly central to the advancement of personalized medicine, as it enables treatment strategies to be tailored to the specific molecular alterations identified in a patient's tissue and further reinforces the central role of the pathologist in modern disease classification and management. However, this thesis will focus on Idiopathic pulmonary fibrosis (IPF) and Alzheimer's disease (AD). Although these diseases arise in different organs and have distinct clinical manifestations, both are driven by tissue remodelling following unknown injuries which result in alterations in extracellular matrix (ECM), spatio-molecular changes and excessive cell death.

Idiopathic Pulmonary Fibrosis (IPF)

Idiopathic pulmonary fibrosis (IPF) is one of the most devastating and progressive forms of interstitial lung disease (ILD). It is characterized by excessive extracellular matrix (ECM) deposition, architectural distortion and remodelling of distal lung parenchyma with progressive loss of respiratory function (48). As the term

idiopathic says, the exact cause of IPF remains unclear. However, several risk factors have been associated with disease development such as genetic predisposition, age, cigarette smoking, environmental or occupational exposures, gastroesophageal reflux and repeated viral or micro-injuries to the alveolar epithelium. Clinically, IPF has a poor prognosis, with median survival often estimated at only 2-3 years after diagnosis.

Patients with IPF typically present with progressive exertional dyspnea, persistent non-productive cough, fatigue and weight loss (in some cases) with unknown origin. On physical examination, fine bibasal inspiratory crackles are frequently detected, and digital clubbing may also be present due to chronic hypoxemia. Importantly, IPF is a clinical diagnosis that requires integration of clinical history, radiological findings and when necessary histopathological evaluation.

Radiologically and histologically, IPF is associated with usual interstitial pneumonia (UIP)(49). However, it is important to know that IPF and UIP are not always synonymous terms. Usual interstitial pneumonia was first introduced as a histological term in the 1960-s as a histopathological pattern observed across multiple lung diseases which was differentiated from desquamative interstitial pneumonia, bronchiolitis obliterans interstitial pneumonia, lymphoid interstitial pneumonia, or giant cell interstitial pneumonia. UIP can be seen not only in IPF, but also in several secondary conditions, including chronic hypersensitivity pneumonitis, drug-induced lung toxicity, asbestosis, and genetic disorders such as Hermansky–Pudlak syndrome. Therefore, distinguishing IPF, sometimes referred to as “idiopathic UIP,” from secondary UIP-like diseases is essential. In 2011, 2018 and 2022 the American Thoracic Society/European Respiratory Society/Japanese Respiratory Society/Latin American Thoracic Association (ATS/ERS/JRS/ALAT) adopted new guidelines to better differentiate UIP and encourage radiologist and pathologies to link UIP more with IPF; they also highlighted the need to look for differential diagnosis (50, 51).

Histopathologically, usual interstitial pneumonia (UIP) is characterized by a combination of morphological features such as 1) patchy interstitial fibrosis 2) spatial and temporal heterogeneity 3) architectural distortion 4) a predominantly subpleural and paraseptal distribution and 5) the absence of histological features suggesting an alternative diagnosis, such as granulomas, prominent organizing pneumonia, or marked interstitial inflammation away from fibrotic areas.

At low magnification, fibrotic areas often neighbour regions with relatively preserved and normal looking lung parenchyma, creating a heterogeneous “patchy” appearance (**Figure 2B**). This spatial heterogeneity is one of the most important diagnostic features at lower magnification, because fibrosis in UIP is not diffuse or uniform, but instead affects the lung in an irregular pattern, usually predominantly subpleural and paraseptal regions. The fibrotic process is usually most pronounced

in the subpleural and paraseptal regions, although it may extend deeper into the lung parenchyma as the disease progresses.

However, temporal heterogeneity is present, meaning that fibrotic lesions at different stages of development coexist within the same tissue sample, even in fibrotic regions at lower magnification. Areas of established, "old fibrosis", composed predominantly of dense, relatively acellular collagen and scar tissue, are found alongside areas of active fibrogenesis known as fibroblastic foci (**Figure 2C)**. Histologically, fibroblastic foci appear as small, convex or dome-shaped subepithelial aggregates of spindle-shaped fibroblasts and myofibroblasts embedded within a loose, myxoid extracellular matrix. As fibrotic remodeling progresses, the normal alveolar architecture becomes increasingly distorted. Dense scarring, collapse of alveolar structures, and remodeling of the interstitium lead to progressive destruction of the normal lung parenchyma, leading to microscopical honeycomb change (**Figure 2D**).Histologically, honeycombing consists of enlarged, cystically dilated airspaces embedded within dense fibrotic tissue. The air spaces are typically lined by metaplastic bronchiolar-type epithelium, including ciliated epithelial cells and mucus-producing cells, reflecting bronchiolization and aberrant epithelial repair. Their lumina may contain mucin, macrophages, cellular debris, and variable inflammatory cells. However, the inflammatory component in UIP is usually mild and is generally mostly within fibrotic and honeycombed areas In addition, smooth muscle metaplasia or hyperplasia is frequently present within fibrotic and honeycombed regions and contributes further to the distorted architecture of the lung.

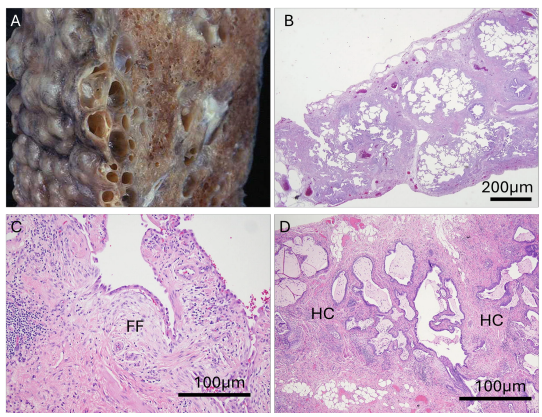

Figure 2. Macroscopic and histopathological features of idiopathic pulmonary fibrosis (IPF) with a usual interstitial pneumonia (UIP) pattern. A) Macroscopic image of an IPF patient lungB) Low-magnification hematoxylin and eosin (H&E) staining of UIP lung tissue demonstrating marked spatial heterogeneity, with patchy fibrosis adjacent to relatively preserved normal parenchyma.C) Higher-magnification view highlighting fibroblastic foci, representing areas of active fibrogenesis.D) Advanced honeycomb changes, characterized by cystic, fibrotic airspaces lined by bronchiolar epithelium, reflecting end-stage architectural remodelling. Figure reproduced from (Lagstein *et al.* 2018) with permission.

As discussed above, mesenchymal cells play a critical role in the pathogenesis of UIP/IPF. However, increasing evidence indicates that epithelial cells are also central to disease initiation and progression. A growing hypothesis suggests that the initial site of injury in IPF may be within the distal alveolar epithelium, involving alveolar type I and alveolar type II cells. As discussed above these cells normally function as progenitor cells for the alveolar epithelium and are responsible for epithelial repair after injury. Repeated or persistent damage to the alveolus can impair normal regeneration and lead to exhaustion of alveolar type II cells or altered cell states (e.g. senescence or acquisition of intermediate cell types). These alterations have been shown to promote epithelial dysfunction which leads to the release of profibrotic mediators that activate surrounding mesenchymal cells (52-54).

Recent studies demonstrated that distal lung epithelial re-programming (also termed aberrant differentiation) is a prevalent feature of IPF. These cells express non-epithelia (e.g. mesenchymal) markers, so called epithelial-to-mesenchymal transition (EMT)(55-57). Several signalling pathways have been shown to contribute to this epithelial plasticity, including TGF-β (58), Wnt (59, 60) and YAP/TAZ (Paper 1, papers not included in this thesis) (54).The reactivation of these developmental and mechanotransductive pathways in the adult lung may initially represent an attempt to restore epithelial integrity after injury. However, in the context of persistent damage and a profibrotic microenvironment, these pathways can become dysregulated, driving epithelial dysfunction, aberrant differentiation, senescence and pathological EMT.

Recent single-cell RNA-seq studies have further substantiated this concept by identifying distinct subpopulations of epithelial cells with aberrant transitional phenotypes in IPF lungs with simultaneously expressing basal epithelial-associated keratins KRT17 and 8, mesenchymal and/or apoptotic and senescence-related markers (55, 56, 61). This supports the idea that the IPF epithelium does not simply lose epithelial identity, but rather becomes trapped in abnormal intermediate states that may interfere with effective alveolar repair.

However, these aberrant epithelial populations represent only a relatively small sub-population of the total lung cells and the origin of this cell is still unclear, which introduces important methodological and conceptual challenges. First, because these cells are rare, conventional 2D histological approaches may fail to detect them. Second, the lung is an inherently three-dimensional organ, with complex spatial organization across airways, alveoli, vasculature and lymphatic systems. Therefore, understanding these aberrant epithelial states requires more than identifying their molecular signature. It is essential to determine where they are located within the tissue, how their spatial distribution changes over time and whether they preferentially emerge in specific microenvironments and how they interact with it. Further if these epithelial populations are distributed across different regions of the lung, an important unanswered question is whether they act as isolated local

phenomena or whether they participate in broader tissue-level communication. They may form spatially separated but functionally related niches that collectively sustain disease progression. Thus, their contribution to IPF pathogenesis cannot be fully understood without resolving their spatiotemporal relationships with surrounding cell populations. Therefore, there is a need of experimental and analytical approaches that preserves the three-dimensional architecture of the lung allowing the study of this sub-population of cells in their native state.

Alzheimer's Disease

Alzheimer's disease (AD) is a progressive neurodegenerative disorder and characterized by memory loss, with further worsening of cognitive abilities with disease progression.

The disease is named after Alois Alzheimer, the German psychiatrist and neuropathologist who first described its characteristic brain pathology in 1907 (62). While examining the brain of his patient Auguste Deter after her death, he observed unusual changes both outside and inside nerve cells. He referred to these abnormalities as cortical miliary foci and intracellular neurofibrillary alterations (63). Today, these changes are known as amyloid plaques and neurofibrillary tangles, which are considered the main pathological hallmarks of AD (**Figure 3**).

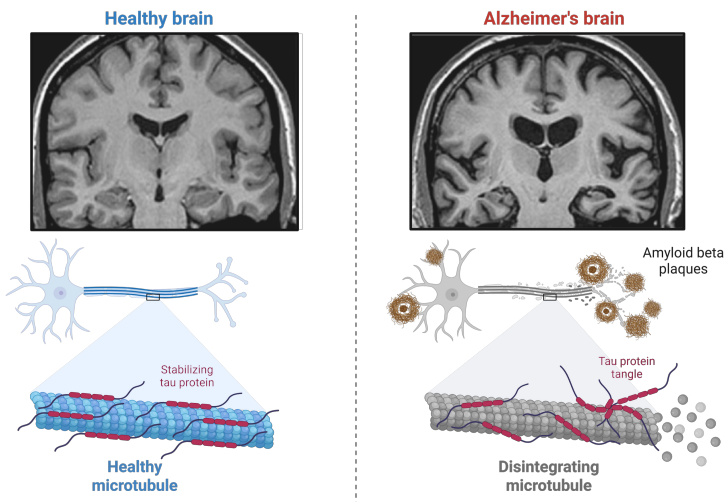

Figure 3. Representative MRI images of a healthy brain and an Alzheimer's disease brain, illustrating neurodegeneration characterized by progressive brain atrophy, including reduced brain volume and enlarged ventricles. The schematic compares healthy neurons with neurons affected by Alzheimer's disease, highlighting the extracellular accumulation of amyloid-β plaques and the intracellular formation of neurofibrillary tangles. Created in BioRender.com

Amyloid plaques consist primarily of amyloid-beta (Aβ) peptides that accumulate extracellularly.(64). Aβ is produced from the sequential cleavage of amyloid precursor protein (APP) (64-66). They occur in different forms, with dense-core plaques and diffuse plaques being the most commonly described (67). Dense-core plaques have a compact fibrillar center surrounded by a less organized halo of Aβ and are typically associated with later stages of the disease (66). Some dense-core plaques are classified as neuritic plaques, meaning that they are surrounded by damaged neuronal processes called dystrophic neurites (67). These abnormal neurites often contain altered tau protein, amyloid precursor protein (APP) or both (68). Plaques are often accompanied by activated microglia and reactive astrocytes, highlighting the strong inflammatory component of Alzheimer's disease (69). Loss of synapses is also commonly seen around these plaques (67, 69, 70).

The other major pathological feature of Alzheimer's disease is the neurofibrillary tangle, an intracellular structure composed mainly of abnormal tau protein. These tangles develop gradually through several stages (71, 72). They first appear as pre-tangles, then mature into fully formed tangles that interfere with normal neuronal function and eventually contribute to their death. Following neuronal death, residual neurofibrillary tangle can remain in the extracellular space, known as a ghost tangles (73). Another tau-related lesion seen in Alzheimer's disease is the neuropil thread, a thread-like accumulation of filamentous tau found throughout affected brain regions (73).

Under normal conditions, tau helps stabilize microtubules and supports axonal transport within neurons (74). In Alzheimer's disease, tau becomes abnormally hyperphosphorylated, which causes it to detach from microtubules and misfold (75). These misfolded tau molecules then aggregate into paired helical filaments, which later form neurofibrillary tangles and neuropil threads. This process contributes significantly to neuronal dysfunction and degeneration (74).

One of the most widely discussed explanations for the development of Alzheimer's disease is the amyloid cascade hypothesis (76). According to this model, the abnormal accumulation of Aβ is an early event that triggers a chain of pathological changes, including tau hyperphosphorylation, tangle formation, neuroinflammation and eventually neurodegeneration (77). These processes are thought to drive the clinical symptoms of the disease.

However, the pathophysiology of AD remains incompletely understood. While extracellular Aβ plaques and intracellular neurofibrillary tangles composed of hyperphosphorylated tau are the defining pathological hallmarks of the disease, the precise mechanisms that initiate and drive AD is under investigation and events associated with disease onset remain unknown. For example, amyloid is known to be able to accumulate decades before symptom onset in some patients and substantial plaque burdens can be observed in cognitively normal individuals. How exactly do amyloid plaques form in real time? Why are certain brain areas such as

the hippocampus and entorhinal cortex affected early, while other regions remain relatively resistant? These are major unanswered questions in the field and new techniques are needed to better understand disease onset and progression, including those which enable the study of living tissue.

Organotypic tissue slices

Organotypic slice culture was first described in 1906 as a method to observe axonal growth during embryonic development (92). In these pioneering experiments, fragments of medullary tube or ectoderm from frog embryos were manually dissected and cultured in lymph fluid. The tissues remained viable for up to four weeks, enabling light microscopic observation of active cilia, muscle contraction and axonal projections. the term “organotypic” was introduced for the first time by the histologist Alexandr Maximow in 1925 in "Maximow double-coverslip assembly" (a modified, sealed hanging-drop culture). This allowed for the long-term cultivation and high-resolution microscopic observation of living tissue explants. Then in 1951, Dame Honor B. Fell described organotypic as “the tissue largely retains its characteristic architecture, remains functional and if derived from undifferentiated material, it may develop in culture in a surprisingly normal way”(78).

Today, organotypic cultures can be generated from a wide range of organs, species and developmental stages. Early methodologies, often referred to as explant cultures, relied on manual cutting to generate tissue pieces typically around 1 mm thick (93-95). However, manual sectioning can introduce human bias and produce uneven slices, both of which may affect experimental reproducibility and interpretation. Furthermore, tissue thickness can be a critical determinant of culture viability, as oxygen and nutrients must defuse from culture medium into the tissue. However, diffusion is limited to around 300-500 μm depending on the tissue type (i.e. how dense and metabolically active it is). Therefore, thick slices are prone to develop hypoxic or necrotic core. The development of vibratome-based sectioning therefore represented a major technical advance, enabling the production of thinner, more uniform, robust, precise tissue slices. This thesis utilized slices from diverse organs but mainly utilized organotypic slices derived from brain and lung for in depth analysis.

Brain tissue slices

Brain is one of the most complex and heterogeneous organs in the human body. The adult human brain contains approximately 80 billion neurons and 40–50 billion glial cells, organized into distinct anatomical and functional regions.

2D cell cultures are among the most widely used model systems in cellular and molecular biology and have contributed immensely to our understanding of physiology, cell signaling, development, and disease mechanisms. However, conventional 2D cultures only partially reproduce the *in vivo* environment. Isolated cells are removed from their native cytoarchitecture and often lack interactions with other cell types, extracellular matrix, blood vessels and neuronal networks.

To overcome some of these limitations, brain tissue slices are increasingly used as *ex vivo* models. Brain slices preserve many features of the native tissue, including cytoarchitecture, regional organization, resident neural and glial populations, ECM and vasculature. Moreover, brain tissue slices provide a unique experimental platform that enables the direct visualization of molecular and cellular processes in real time while preserving much of the native tissue architecture and cellular microenvironment, which is otherwise is very challenging. Therefore, they represent an intermediate model between simplified *in vitro* cultures and complex *in vivo* animal or human studies.

Broadly, brain tissue slices can be divided into two major categories: acute brain slices and organotypic brain slice cultures (79). Acute brain slices are prepared immediately after brain extraction and vibratome sectioning. They are commonly used for electrophysiological recordings, calcium imaging, synaptic transmission studies, pharmacological assays and short-term functional experiments. However, acute brain slices require continuous maintenance in artificial cerebrospinal fluid-like medium, typically with high oxygenation, controlled temperature and balanced ionic composition to closely mimic physiological conditions. Their viability is limited, often 9-10 hours, after which tissue integrity and physiological activity progressively decline and they needs to be converted to organotypic brain slice culture (79). This process involves replacing the serum-, antibiotic/antimycotic -and growth factor-free, highly oxygenated, glucose and physiological salts artificial cerebrospinal fluid (aCSF) with a conventional tissue culture medium e.g. Minimum Essential Medium (MEM), supplemented with serum, usually HEPES buffer, antibiotics/antimycotics, glutamine and additional (80, 81). This culture modification supports the long-term viability of brain slices. Organotypic slices have been shown to retain tissue architecture and multicellular interactions for days to weeks, making them suitable for longitudinal studies, disease modelling, viral transduction, live imaging and drug testing (82).

Brain tissue slices can be generated from both rodent and human tissue (**Figure 4**). Rodent brain slices are commonly prepared from wild-type animals, genetically modified models or disease models, allowing controlled investigation of specific molecular pathways (83). Human brain slices, on the other hand, are typically obtained from neurosurgical resections, including epilepsy surgery, tumor removal, intracerebral hemorrhage-related surgery or tissue collected during ventricular shunt placement (84). In some cases, postmortem human tissue can also be adapted for

organotypic culture, allowing investigation of age- and disease-related mechanisms in human-derived brain tissue.

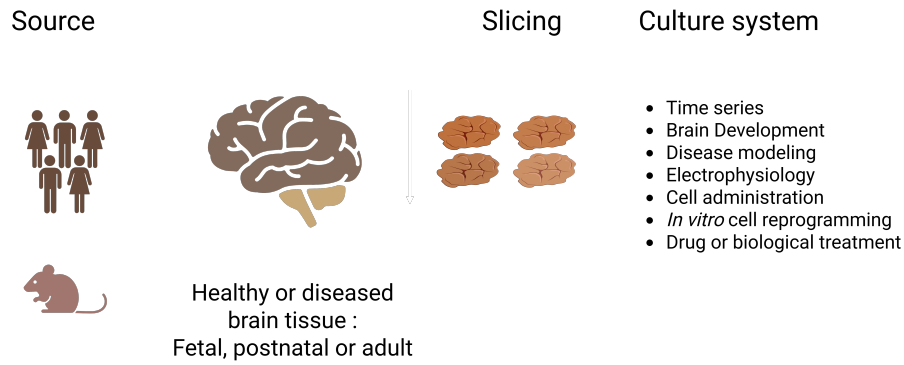

Figure 4. Overview of the generation of brain slices and their application in modelling neurodevelopment, diseases and the therapeutic strategies. Created in BioRender.com by NG

Brain tissue slices are also used for modeling neurological and neurodegenerative diseases. Transgenic mouse models have been widely used to generate slices that reproduce features of Alzheimer's disease. Recently organotypic slices were used for studying amyloid-β accumulation, tau pathology, plaque formation, synaptic dysfunction and neuroinflammation (85).

Importantly, patient-derived postmortem human brain tissue has been explored as a platform for disease modeling. Recent work has demonstrated that postmortem adult human brain explants can retain functional properties in organotypic culture, including responses to electrical stimulation and forms of synaptic plasticity (86).

Overall, brain tissue slice cultures provide a powerful *ex vivo* platform that bridges the gap between simplified *in vitro* models and *in vivo* systems. By preserving native tissue architecture, multicellular interactions, and regional brain organization, they allow more physiologically relevant studies of brain. Although challenges remain, including tissue viability, limited access to human material, culture-induced changes and ethical considerations

Precision-Cut Lung Slices (PCLS)

Lung diseases are among the leading causes of death worldwide and are associated with poor prognoses across diverse patient populations. Although animal models of pulmonary disease have historically contributed to our understanding of lung development, aging and adult disease, there is now strong motivation to develop alternative methodologies. This shift toward alternative models is driven both by

societal efforts to reduce animal experimentation and by the scientific need for *ex vivo* systems composed entirely of human cells and ECM that more faithfully reproduce human lung anatomy and physiology, features that cannot be fully modelled in animals. On the other hand, the use of isolated human cells, monocultures or even co-cultures have been extensively used, but these systems fail to fully recapitulate the complexity of the organ, particularly its multicellular interactions and ECM).

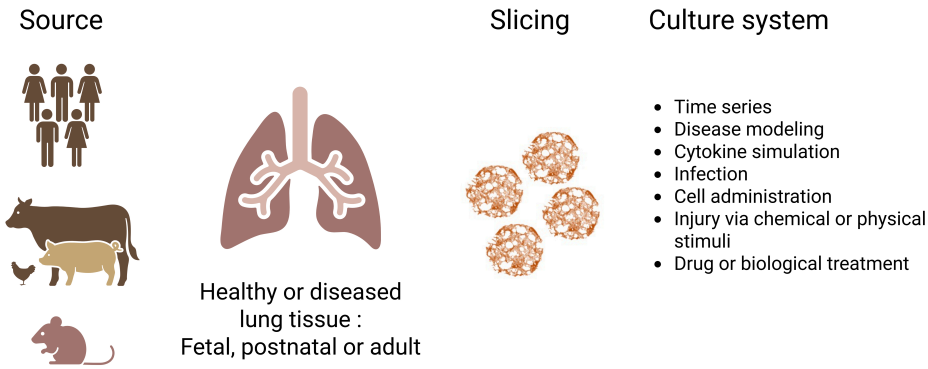

Figure 5. Overview of the generation of lung slices and their application in modelling development, diseases and the therapeutic strategies. Created in BioRender.com by NG

In this context, organotypic cultures of lung tissue represents one of the most attractive alternatives. By preserving native cell types in their spatial locations and maintaining the cell–ECM interactions, organotypic models provide a robust physiological baseline.

The preparation of PCLS (**Figure 5**) is technically challenging (especially from human). Because the lung is highly elastic and lacks structural stability in its deflated state for reproducible sectioning, it is common that the airways are instilled with a supportive hydrogel that makes cutting easier (e.g. with low-melting agarose prior to slicing). Agarose provides the necessary support for precision cutting (a well-inflated lung is much easier to section) under cytocompatible conditions at 4°C, however, its use also introduces potential limitations that must be considered in downstream analyses (for example during RNA isolation) (87).

Importantly, the choice between explant culture and PCLS should always be guided by the specific experimental question (**Table 1)**. Explants remain a powerful and rapid model for addressing fundamental developmental questions. In contrast, studies requiring rigorous paired comparisons, pharmacological screening or

minimization of hypoxia-induced cell death in thicker tissue benefit from the uniform thickness and reproducibility of PCLS.

Table 1. Comparison of lung explants and PCLS highlighting key differences.

	Explant Culture	**Precision-Cut Lung Slices (PCLS)**
Generation Method	Manual dissection	Vibratome
Typical Thickness	> 1 mm (variable)	50–500 μm (highly uniform)
Preparation Time	Rapid (no inflation required)	Slower (requires agarose infiltration)
Major Limitation	High risk of core hypoxia	Specialized equipment and expertise

The potential applications of PCLS, together with the downstream analytical methods used to investigate them, will be discussed in detail in this thesis.

Use of PCLS to study lung development

Lung development is a tightly regulated process that occurs primarily during gestation but continues postnatally in most mammalian species, including humans. Consequently, both explant cultures and PCLS can be generated from prenatal or postnatal lungs, depending on the species and the specific experimental question (88, 89). Interestingly, lung tissue from both rodents and humans appears to retain the biological cues required to support branching morphogenesis and alveolarization *ex vivo* from at least the pseudoglandular stage (89, 90), although some differences compared with *in utero* development have been reported, such as the absence of elastin deposition *ex vivo*(91). Explant cultures, which are typically derived from earlier developmental stages and PCLS, which are generally generated from later stages when more tissue is available, have therefore both been used to study lung morphogenesis in animals and humans across different stages of development (92, 93).

A major advantage of foetal explant cultures and PCLS is that they enable the investigation of key developmental events at the molecular level. For example, the use of PCLS allows live imaging of alveolar septation during alveologenesis, which is currently not feasible to study with cellular resolution *in vivo* (88). Murine PCLS have also been used to examine the effects of hyperoxia on lung development, including its possible role in the onset of bronchopulmonary dysplasia and to

evaluate pharmacological and biological interventions in the same experimental setting (94). In addition, explant cultures and PCLS offer a more controlled platform for studying the relationship between lung development and the intrauterine environment, which remains difficult to investigate *in vivo*.

Recent studies using ex vivo murine fetal explant cultures demonstrated that amniotic fluid from pre-eclamptic mice was sufficient to disrupt fetal lung development in explants derived from healthy mice (95). The same model has also been used to evaluate a novel biological therapy aimed at preventing lung developmental abnormalities associated with pre-eclampsia, namely extracellular vesicles derived from mesenchymal stromal cells (95). Furthermore, PCLS can be used to study the development of murine lungs derived from genetically modified mice to study lung specific versus systemic effects. A recent study (Paper 2, papers not included in the thesis) used PCLS derived from E18.5 mouse embryos to help determine the role of laminin γ1 chain in Tagln positive cells (found in smooth muscle cells and alveolar myofibroblasts). These mice died shortly after birth and were born cyanotic. We used PCLS *ex vivo* culture to evaluate the capacity of the mutant lungs to continue development. We found that loss of laminin γ1 chain in Tagln positive cells resulted in incomplete lung development, including compromised basement membrane development and impaired alveolarization (96).

Use of PCLS to study existing and potential therapies

Since many PCLS replicates can be generated from a single lung, in both rodent and human tissues, this model enables multi-modal analyses under a single experimental condition. Furthermore, PCLS retain patient-specific characteristics and their potential for drug screening, including target identification and validation, has already been demonstrated in several studies (97). PCLS derived from both animal and human tissue have been used to model a wide range of diseases, including acute and chronic lung disorders such as chronic obstructive pulmonary disease (COPD), IPF, asthma, and lung cancer. Both healthy and diseased tissue can be used to generate PCLS, and the choice depends on tissue availability as well as the specific research question being addressed.

However, the generation of PCLS from diseased human tissue remains challenging. In addition, most diseased human samples represent end-stage disease, which is not ideal from a therapeutic perspective, as treatments are preferably administered during earlier stages of disease progression. To address this limitation, several studies have demonstrated the feasibility of inducing lung injury in healthy lung tissue or in histologically and macroscopically normal regions of surgical resections, through exposure to infectious agents, cytokines, enzymes, or other injurious stimuli in order to model disease onset. The suitability of PCLS for drug screening, including evaluation of next generation therapies such as DNA or RNA therapies (98-100), has also been evaluated in multiple studies by assessing whether this

model can generate disease-specific readouts in response to compounds approved for respiratory diseases.

Substantial efforts have furthermore been devoted to extending the viability of these cultures from a few days to several weeks, thereby broadening the experimental window for longitudinal investigations and drug-testing applications. Despite these advancements, significant methodological variability persists in the field. No universally accepted culture protocol exists and experimental procedures differ in critical aspects between laboratories such as agarose type and percentage, culture media formulation and inclusion of a pre-experimental resting period. For example, some protocols recommend overnight recovery following slice generation before initiating experiments, whereas others begin experiments immediately after sectioning. Such differences may influence cellular responses and experimental outcomes. Therefore, standard solutions/strategies are needed to enable comparison between studies which will ultimately save time, resources and make PCLS experiments more reproducible. Alternatively, standard reporting criteria can help make interlab differences more clear. This is especially critical given recent government initiatives to enable the use of PCLS and other ex vivo model systems (i.e. New Advanced Methodologies (NAMs) to replace animals in demonstrating efficacy prior to initial human clinical trials.

Moreover, it is important to recognize a fundamental limitation common to all tissue slice models that they are separated from systemic circulation. Consequently, they lack physiological blood flow, immune-cell recruitment from the periphery, endocrine regulation, and normal nutrient and oxygen delivery dynamics. This renders the tissue intrinsically more vulnerable to injury, metabolic stress and progressive cellular degeneration during *ex vivo* culture. Consequently, cell death becomes an unavoidable component of tissue slices. This may complicate evaluation of cytotoxicity or even other molecular events when evaluating potential therapies. Therefore, a comprehensive understanding of the molecular mechanisms governing cell death is critical for the accurate interpretation of tissue slice studies and for distinguishing between treatment effect from culture-induced artifacts.

Cell Death

Historically, human beings have been fascinated by death because it was a constant and visible part of our life (101). Beyond this observable reality, however death also occurs as a fundamental process at the cellular level (102). Microscopically, cell death is far more than simple cessation of cellular function; it is a highly regulated and essential biological mechanism that plays a central role in development as well as in maintaining tissue homeostasis (103). In the adult human body, approximately 50 billion cells are eliminated each day, which corresponds roughly to the total body weight yearly (104). Physiological cell death is a fundamental biological process

required for proper development, tissue renewal and repair. However, when triggered by excessive stress, injury or disease, cell death can become detrimental, shifting from a homeostatic process to pathological (105). Insufficient cell death may contribute to hyperproliferative disorders, for example cancer (106, 107); excessive cell death can also lead to degenerative diseases, including the nervous system.

Traditionally, cell death has been divided into two broad categories: necrosis and programmed cell death (PCD)(108). Necrosis was classically regarded as an uncontrolled and "accidental" form of cellular collapse caused by acute injury, whereas programmed cell death was understood as an orderly, genetically regulated process driven by developmental or physiological signals (108). However, the identification of RIPK1, RIPK3 and MLKL as central regulators of necroptosis demonstrated that necrosis can also be a regulated form of cell death. According to the Nomenclature Committee on Cell Death (NCCD) recommendations published in 2018 and revised in the 2023 NCCD, cell death can be broadly classified into two umbrella categories: accidental cell death (ACD) which is non-programmed and regulated cell death (RCD) which is driven by defined molecular mechanisms. Further, PCD is generally considered a physiological subset of RCD (**Figure 6**) (109).

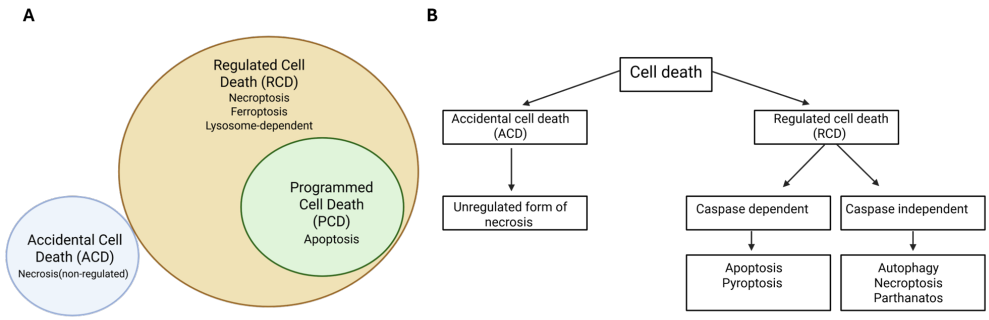

Figure 6. A and B Schematic of different cell death mechanisms according to the Nomenclature Committee on Cell Death (NCCD) recommendations. Created in BioRender.com by NG

As a result, a broad range of additional RCD subtypes have been identified: lysosomal cell death (110), autophagic (111), mitoptosis (112), paraptosis (113), pyroptosis (114), parthanatos (115), NETosis (116), necroptosis (117), immunogenic cell death (118), entosis (119), methuosis (120), ferroptosis (121), autosis (122), alkaliptosis (123), oxeiptosis (124), cuproptosis (125) and erebosis (126). The existence of these diverse pathways reflects the evolutionary development of multiple mechanisms that protect the organism and preserve physiological balance.

Nevertheless, this thesis will focus specifically on apoptosis and how it relates to conditions which may be encountered in *ex vivo* models.

Apoptosis

Extrinsic pathway

Extrinsic apoptosis is initiated when extracellular death ligands, including tumor necrosis factor (TNF)-α, Fas ligand (FasL) and TNF-related apoptosis-inducing ligand (TRAIL), bind to corresponding death receptors at the plasma membrane-TNFR1, Fas/CD95, and TRAIL receptors (127-129) (**Figure 7**). In the Fas pathway, receptor ligation promotes recruitment of the adaptor protein Fas-associated death domain (FADD) together with procaspase-8, resulting in formation of the death-inducing signalling complex (DISC) (127, 128). Within the DISC, procaspase-8 is activated, whereas cellular FLICE-like inhibitory proteins (c-FLIP isoforms) can bind caspase-8 and modulate its activation, thereby influencing whether signalling proceeds toward apoptosis. Activated caspase-8 subsequently initiates the downstream caspase cascade by cleaving and activating executioner caspases, particularly caspase-3, caspase-6, and caspase-7, which mediate the degradative phase of apoptosis (127-129). TNFR1-mediated apoptosis is mechanistically more complex than Fas signalling. Following TNF binding, TNFR1 first assembles a membrane-associated signalling complex, termed complex I, which contains TRADD, RIPK1, TRAF2/5, and cIAP1/2 and generally promotes pro-survival and pro-inflammatory signalling through NF-κB. When these survival checkpoints are impaired, or when RIPK1 ubiquitination and phosphorylation are dysregulated, TNFR1 signalling can shift toward formation of a cytosolic death complex containing FADD and caspase-8, thereby promoting apoptosis (129).

Intrinsic pathway

The intrinsic pathway, also known as the mitochondrial pathway, is activated by intracellular stress signals such as DNA damage, oxidative stress, mitochondrial injury, or in some cases detachment from the extracellular matrix (anoikis). This pathway is tightly controlled by the BCL-2 family of proteins, which includes anti-apoptotic members such as BCL-2, BCL-xL, MCL-1 and BCL-W, as well as pro-apoptotic effectors such as BAX and BAK and BH3-only proteins including BIM, BID, BAD, NOXA, and PUMA (127, 129, 130) (**Figure 7**). In response to apoptotic stress, BH3-only proteins neutralize anti-apoptotic BCL-2 family members and promote activation of BAX and BAK, which oligomerize in the outer mitochondrial membrane and induce mitochondrial outer membrane permeabilization (MOMP). MOMP results in the release of cytochrome c and second mitochondria-derived activator of caspases (SMAC/DIABLO) from the mitochondrial intermembrane space into the cytosol(127, 130). Cytosolic cytochrome c then binds apoptotic protease activating factor-1 (Apaf-1) and procaspase-9 to form the apoptosome, a

multimeric complex that activates caspase-9. Activated caspase-9 subsequently cleaves and activates downstream executioner caspases cascade, caspase-3, caspase-6 and caspase-7 (127). Because mitochondrial damage and caspase activation can amplify one another, intrinsic apoptosis is increasingly viewed as a self-reinforcing network rather than a strictly linear signalling cascade.

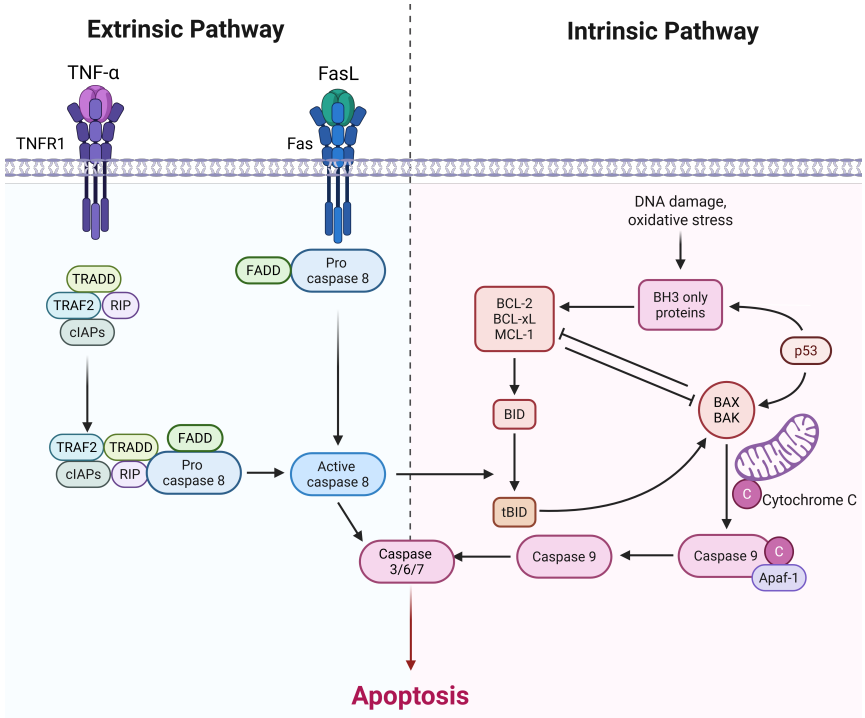

Figure 7. Schematic of extrinsic and intrinsic pathways of apoptosis. Created in BioRender.com by NG

Execution phase of apoptosis

Although the extrinsic and intrinsic pathways are initiated by distinct upstream signals, both converge on a common execution phase mediated by the activation of executioner caspases, such as caspase-3, caspase-6, and caspase-7, and caspase-10. Executioner caspases are structurally distinct, possessing short pro-domains, and their activation commits the cell irreversibly to apoptosis (127). These executioner caspases orchestrate the demolition phase by cleaving a broad spectrum of target proteins. Crucially, they activate a cytoplasmic endonuclease, the caspase-activated DNase (CAD), which degrades chromosomal DNA within the nucleus and drives chromatin condensation. Caspase-3, the most prominent of the executioner caspases and activatable by any initiator caspase, is the explicit activator of CAD (127, 130). Beyond DNA fragmentation, executioner caspases cleave proteases that dismantle nuclear lamins and cytoskeletal proteins, leading to the collapse of the nuclear

structures and the cytoskeleton. This coordinated proteolysis produces the characteristic morphology of apoptosis: chromatin condensation, nuclear shrinkage with further fragmentation (karyorrhexis), cytoplasmic blebbing and the packaging of cellular contents into discrete, membrane-bound apoptotic bodies (127, 130).

Escape from Apoptosis

The mechanisms described above of apoptotic cell death represent the canonical pathways of programmed cell death, activated in response to a wide range of intracellular and extracellular stressors. However, cells do not always fully commit to apoptosis and therefore can escape it maintaining cell viability despite pro-death signals. The most known example of this pathological survival is cancer (131). Cancer cells show multiple or overlapping, mechanisms that enable escape from apoptosis. These include genetic alterations in key regulators of cell death, such as overexpression of anti-apoptotic BCL-2 (132), loss or mutation of tumour suppressor p53 (133), dysregulation or inactivation of caspases (134) and death receptors (DR5).

Importantly, pathological escape from apoptosis is not restricted to cancer. Non-malignant diseases can also exhibit aberrant survival of specific cell populations. For example, in idiopathic pulmonary fibrosis (IPF), myofibroblasts display resistance to apoptosis, leading to their persistence within fibrotic lesions (135, 136). Similarly, certain populations of alveolar epithelial type II (AECII) cells can exhibit dysregulated apoptotic responses, contributing to impaired tissue repair and disease progression (137, 138). These findings highlight that defective apoptotic regulation is a broader pathological feature, extending beyond oncogenesis to fibrotic and degenerative disorders. Therefore, careful evaluation of apoptotic cells in *ex vivo* systems is critical to correctly interpreting disease-specific versus model-specific or stimuli-specific effects.

Anastasis – living beyond the death

Activation of executioner caspases, particularly caspase-3 and caspase-7 has traditionally been called as the “point of no return”. Canonically, once a cell enters the execution phase of apoptosis, death is considered inevitable. However, this concept has been increasingly challenged by evidence showing that “point of no return” is not always an irreversible process. Under certain conditions, cells that have already passed this point can recover and survive if the death-inducing stimulus is removed. This phenomenon is known as anastasis, meaning “rising from death”. Recent studies have shown that apoptosis can be reversed even after activation of executioner caspases, both in cultured cells and *in vivo*. For example, ethanol-induced apoptosis has been shown to be reversible after removal of ethanol and replacement with fresh medium in several cell types, including primary liver and

heart cells, NIH 3T3 embryonic fibroblasts and human cervical cancer HeLa cells. Live-cell imaging of HeLa cells carrying a caspase-3 biosensor showed caspase-3 reporter activation during apoptosis, followed by signal reduction upon washing with fresh medium (139).

At the molecular level, this is particularly interesting because late-stage apoptosis is associated with severe intracellular damage, DNA and nuclear fragmentation. Nevertheless, anastasis has been observed even after these advanced molecular events. Mouse primary hepatocytes and non-cancerous NIH 3T3 fibroblasts exposed to ethanol displayed classical markers of apoptosis DNA strand breaks and nuclear fragmentation. Despite this, after withdrawal of the apoptotic stimulus and restoration of normal culture conditions, a fraction of these cells were able to reverse the death process and survive (140).

However, survival through anastasis may come with important biological consequences. Cells that recover from apoptosis may not return to a completely normal state. Instead, they can retain unresolved or incorrectly repaired DNA damage. Surviving cells have been reported to acquire chromosomal abnormalities, increased micronuclei formation and other signs of genomic instability. In this sense, anastasis may act as a double-edged mechanism: on one hand, it may allow the preservation of cells after transient or sublethal injury and on the other hand, it may permit damaged cells to survive, potentially contributing to malignancy(139) .

Thus, anastasis introduces an important layer of complexity into our understanding of apoptotic cell death. Rather than being a strictly linear and irreversible process, apoptosis may contain a window of reversibility during which cells can either continue toward death or activate recovery. The molecular determinants of this decision remain incompletely understood and it is not known whether anastasis occurs frequently under physiological or pathological conditions *in vivo* or *ex vivo*.

Tissue analysis with light-based techniques

The previous sections of this thesis described the molecular pathways of idiopathic pulmonary fibrosis (IPF) and Alzheimer's disease (AD), mechanisms of cell death and the application of organotypic tissue slices as experimental models. However, the subsequent downstream analysis of these tissues is a crucial step, as it enables the extraction of structural, molecular, biochemical and spatial information that is essential for understanding disease mechanisms and treatment responses. Further, to perform and interpret tissue-based experiments accurately, it is important to understand the methodological principles underlying tissue processing and analysis, as well as the advantages and limitations of each technique.

Therefore, the following sections will discuss the bases of major methodological approaches used in this thesis, including tissue fixation and processing, labelling methods and light-based analytical techniques such as microscopy and spectroscopy.

Light-based microscopy

We interact with light every day, often without appreciating how fundamental it is to both life and society. Sunlight provides the energy that sustains nearly all ecosystems on Earth, further it enables our vision allowing us to navigate the world around us. The studies and manipulation of light led to breakthroughs in fields ranging from astronomy, medicine, engineering, telecommunications and other. But what is this mysterious phenomenon? Light is an electromagnetic radiation (**Figure 8**) that exhibits both wave-like and particle-like properties (141, 142). Simply, it is energy that travels through space at the highest possible speed, behaving both as a wave and as a stream of particles called photons. This is known as the dual nature of light (143).

In this thesis, however, the focus is on how light interacts with matter through processes such as absorption, scattering, reflection and fluorescence. These interactions form the basis of the different imaging modalities used in this thesis, enabling the visualization and characterization of matter across multiple spatial scales.

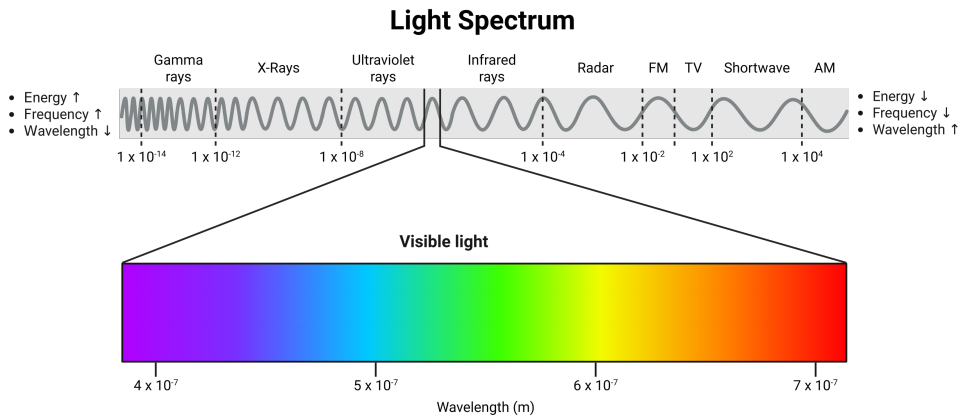

Figure 8. Spectrum of light. Created in BioRender.com

Light Microscopy

Microscopy has long been a fundamental and widely used tool for exploring the microscopic world, revealing structures and processes that cannot be seen with the naked eye. However, microscopy should not be viewed merely as an imaging tool. It is also a scientific challenge that requires careful planning and methodological precision. Successful microscopy depends not only on the instrument itself, but also on the quality of sample preparation and the experimental objectives. Before imaging begins, it is essential to consider how the tissue will be handled, processed, stained and mounted, as well as which structures or cellular features are intended to be visualized. As discussed throughout this thesis, negligence in any of these preparatory steps can result in insufficient tissue quality, poor staining or imaging artefacts. Such issues can compromise the reliability of the data and jeopardize entire experiments, often at considerable cost in terms of time, effort and resources. Therefore, careful experimental design and thoughtful planning before each microscopy-based experiment are critical.

Among the different types of microscopy, the light microscope has held a particularly important because of its relative simplicity, versatility, accessibility Early pioneers such as Robert Hooke and Antonie van Leeuwenhoek used the first light microscopes in the 17th to observe cells and microorganisms (144). What began as basic brightfield microscopy has developed into a wide range of advanced imaging techniques, including phase-contrast, fluorescence, confocal and light-sheet microscopy, each offering improved specificity, contrast and spatial resolution (145). A light microscope operates by using a light source and optical lenses to generate magnified images with high clarity and resolution. In this thesis the main focus will be fluorescence-based microscopes (145-147). Therefore, it is important to understand what fluorescence is, how images are generated and resolution limits of the microscopes.

The development of diverse fluorescent probes, together with the introduction of genetically-engineered encoded fluorescent proteins (which will be discussed separately), has expanded the possibilities for highly specific labelling of different biological structures within tissues (148, 149). These advances have established fluorescence microscopy as a central tool in bio-medical research, enabling detailed investigation of complex tissue organization both in live and fixed samples.

Fluorescence

Fluorescence refers to the capacity of certain molecules to absorb light at a specific wavelength and then emit it at a longer wavelength (150). This phenomenon arises from transitions between electronic states of the fluorophore, commonly represented in a Jablonski diagram (151). When excitation light is absorbed, the molecule is

promoted to an excited singlet state, which can relax through fluorescence emission, non-radiative dissipation or intersystem crossing to the triplet state. However, owning instability of the excited electronic state, the fluorophore eventually returns to a lower-energy state by emitting a lower-energy photon at a longer wavelength. The wavelength difference between excitation and emission, known as the Stokes shift (152) and is essential for separating excitation light from emitted fluorescence using optical filters and dichroic mirrors (153, 154). (**Figure 19**). A complete fluorescence cycle therefore consists of photon absorption followed by fluorescence emission.

Figure 9. Excitation and emission spectra of DAPI nuclear staining. The dotted line represents the excitation spectrum, while the solid line/shaded curve represents the emission spectrum.

However, an important limitation or to say more precisely, side effects of fluorescence imaging are photobleaching and phototoxicity. Photobleaching is the irreversible loss of fluorescence resulting from excessive light exposure and photo-induced chemical damage to the fluorophore which can happen in both live and fixed sample (155). It increases with excitation intensity and generally follows an exponential decay (156). Once bleached, the molecule can no longer emit fluorescence, which is a major limitation in long-term live imaging. The number of fluorescence cycles a fluorophore can undergo before bleaching depends on factors such as temperature, oxygen concentration and the local chemical environment.

Phototoxicity, is actually light-induced damage of specimen and most importantly can occur only in live cells or tissue. There are two types of phototoxicity. One is due to direct absorption of light, particularly high-energy photons and from the ultraviolet (UV) or short-wavelength blue region. These photons carry more energy and can directly damage DNA, proteins, and membranes (157). Therefore, longer-wavelength and lower-energy light is preferred for live imaging. The second one is

indirect: through fluorophore excitation and production of reactive oxygen species (ROS). When ROS levels exceed the cells' antioxidant capacity, oxidative stress develops and progressively compromises cellular integrity leading to DNA lesions, protein dysfunction and lipid peroxidation. Moreover, mitochondria are especially affected, as they are both a source and target of ROS. Oxidative damage to mitochondrial membranes can promote release of cytochrome c and triggering intrinsic apoptosis and leading to programed cell death. Therefore, careful control of light during live imaging experiments is critical to minimize its effect while maximizing its utility as a means to monitor molecular changes.

Fluorescent imaging

After sample preparation and fluorescent labelling, the culmination is image generation, where fluorescent signals are converted into spatial information. Simply put, fluorescence microscopy images are formed by detecting photons emitted from fluorescent dyes or probes that are bound to or inherent to specific structures of interest within the sample (158).

Fluorescence image formation involves three main steps. First, excitation occurs when fluorophores absorb photons delivered through the microscope objective, promoting them to an excited electronic state. Second, during emission, fluorophores relax and emit lower-energy photons at a longer wavelength, named as Stokes shift. Third, these emitted photons are collected and detected by the objective and producing a digital image composed of pixels (150).

Each pixel contains an intensity value proportional to the number of detected photons from a corresponding region of the sample. Therefore, the image represents a spatial map of fluorophore distribution (150). However, in most cases, the generated image is not a perfect representation of the real object. During image formation, the true fluorophore distribution is degraded by several physical and technical factors, mainly optical blur, convolution and noise.

Resolution

However, it is also important to consider the resolution of the microscope, as this determines how much structural detail can be reliably distinguished in the final image. Simply, resolution is the minimum distance at which two closely spaced objects can still be visualized as separate structures (159).

In conventional optical microscopy, spatial resolution is mainly limited by diffraction, which arises because light behaves as a wave and spreads when passing through the objective aperture (160). As a result, a point object is not imaged as an infinitely small point, but as a broadened diffraction pattern, limiting the ability of

the microscope to distinguish very closely spaced structures. This fundamental limit is described by the Abbe diffraction limit:

$$d = \frac{\lambda}{2NA}$$

where d is the minimum resolvable distance, λ is the wavelength of light and NA is the numerical aperture of the objective lens (160-162).

Endogenous fluorescent proteins

Endogenous fluorescent proteins are naturally occurring fluorophores that can be genetically encoded and expressed in living cells. They absorb light at specific wavelengths and re-emit it at longer wavelengths, enabling non-invasive visualization of biological processes in real time without the need for exogenous dyes or labels. The field began with the isolation of green fluorescent protein (GFP) from the jellyfish Aequorea victoria in 1962 by Osamu Shimomura(163, 164). In the 1990s, Martin Chalfie demonstrated that GFP could be expressed in heterologous systems such as Escherichia coli and Caenorhabditis elegans(165), while Roger Tsien clarified the basis of GFP fluorescence and engineered variants with altered spectral properties (166). These contributions led to the 2008 Nobel Prize in Chemistry being awarded jointly.

Following the discovery of GFP, many additional fluorescent proteins were discovered or engineered from marine organisms (**Table 2**). These include cyan fluorescent protein (CFP) and yellow fluorescent protein (YFP), which are spectral variants of GFP(167, 168). However, red fluorescent proteins such as DsRed are derived from Discosoma species (169). Subsequent engineering efforts produced improved monomeric variants including mCherry and mKate. In addition, mNeonGreen was developed as a bright monomeric yellow-green fluorescent protein derived from a fluorescent protein of the cephalochordate Branchiostoma lanceolatum (170). However, this area is constantly developing, with more stable, brighter proteins. Together, these proteins span much of the visible spectrum and enable multiplex imaging of several targets simultaneously.

Fluorescent proteins are widely used as genetic reporters by placing their genes under specific promoters or by fusing them to proteins of interest. However, fluorescent proteins are not without limitations. Their fluorescence can be sensitive to environmental conditions such as pH, temperature, and the physicochemical properties of the surrounding cellular compartment, which may alter signal intensity, folding, or chromophore maturation. In particular, many fluorescent proteins lose signal in acidic environments, and some may perform poorly after fixation or under suboptimal conditions. Consequently, in certain tissue-staining applications, endogenous fluorescence may be insufficiently preserved or too weak

to detect reliably, making antibody-based amplification or immunostaining against the fluorescent protein necessary.

Table 2 Overview of commonly used endogenous fluorescent proteins spanning the blue to far-red spectral range. The table summarizes the excitation and emission peaks of each fluorescent protein, distinguishes naturally from their engineered variants and their evolutionary lineage and relationships among major fluorescent protein.

Spectral class	Protein	Excitation max (nm)	Emission max (nm)	Natural or engineered	Lineage / source organism
Blue	mTagBFP2	399	454	Engineered	eqFP578 lineage (*Entacmaea quadricolor*)
Cyan	mTurquoise2	434	474	Engineered	CFP lineage (*Aequorea victoria*)
Green	wtGFP	395 / 475	509	Natural	*Aequorea victoria*
Green	EGFP	488	507	Engineered	wtGFP lineage (*Aequorea victoria*)
Yellow	EYFP	513–514	527	Engineered	GFP lineage (*Aequorea victoria*)
Yellow	mVenus	515	528	Engineered	EYFP lineage (*Aequorea victoria*)
Yellow	Citrine	516	529	Engineered	EYFP lineage (*Aequorea victoria*)
Yellow	YPet	517	530	Engineered	Venus lineage (*Aequorea victoria*)
Orange/Red	tdTomato	554	581	Engineered	DsRed lineage (*Discosoma sp.*)
Orange/Red	eqFP578	552	578	Natural	Entacmaea quadricolor
Red	DsRed	558	583	Natural	Discosoma sp.
Red	TagRFP	555	584	Engineered	eqFP578 lineage (*Entacmaea quadricolor*)
Red	mRFP1	584	607	Engineered	DsRed lineage (*Discosoma sp.*)
Red	mCherry	587	610	Engineered	DsRed lineage (*Discosoma sp.*)
Far-red	mKate	588	635	Engineered	eqFP578 lineage (*Entacmaea quadricolor*)
Near-IR	iRFP670	643	670	Engineered	Bacterial phytochrome lineage (*Rhodopseudomonas palustris*)

Microscope Selection

Widefield

Widefield microscopy is a conventional and widely used imaging approach in light microscopy in which the entire specimen, or the entire field of view, is illuminated at once. (**Figure 10**). In transmitted-light widefield imaging, such as brightfield microscopy, visible light passes through the specimen and is collected by the objective lens to form an image. Because thick specimens reduce image clarity and increase overlap of structures, samples are typically prepared as thin sections to improve light transmission and contrast; in routine histology, sections are often around 3–5 μm thick, although thicker sections may also be used depending on the application. Widefield microscopy is particularly useful for rapid imaging of general morphology, histological organization, and microorganism distribution, especially in fixed samples, and it can also be applied to fluorescence imaging of labelled structures. Its major advantages include simplicity, relatively low cost, ease of use, and fast image acquisition. However, widefield microscopy has important limitations, including relatively poor axial resolution and substantial out-of-focus background when imaging thicker specimens. In widefield fluorescence microscopy, illumination of the whole specimen can also increase photobleaching in both fixed and live samples.

Confocal

Confocal microscopes provide massive improvement in resolution over conventional widefield microscopes, but their real advantage lies in producing high-contrast images via optical sectioning. By blocking out-of-focus light, a confocal microscope delivers a sharp image derived solely from the focal plane. The key component common to all confocal systems is one or more placed pinhole apertures, developed by Marvin Minsky in 1957 (171) (**Figure 10**). This pinhole ensures that only fluorescence originating from the focal point reaches the detector, light emitted from above or below the focal plane is blocked. In Confocal laser scanning microscopy (CLSM), image is generated pixel by pixel and fluorescence is detected and collected from one focal point at a time (172). In addition, optical sections can be acquired from multiple focal planes along the z-axis. These sequentially captured images can subsequently be reconstructed into a 3D representation of the specimen. However, the confocal microscope has its own drawbacks (172). These include limited imaging speed due to point-by-point scanning, increased photobleaching and phototoxicity (from repeated or intense laser exposure), higher system complexity and cost compared to widefield microscopy. Moreover, confocal microscopy is typically limited to imaging depths of about 50–300 μm (depending on tissue), making it less suitable for thick tissues or whole-mount specimens without specialized clearing techniques.

Light-sheet fluorescence microscopy (LSFM)

Over the past three decades, microscopy development has increasingly focused on overcoming the limitations of conventional widefield and confocal systems while preserving their main advantages, such as the rapid image acquisition of widefield microscopy and the optical sectioning capability of confocal microscopy. This effort led to the development of light-sheet fluorescence microscopy (LSFM), also known as selective or single-plane illumination microscopy (SPIM), which separates the illumination and detection paths and thereby enables selective excitation of a single optical plane **(Figure 10**).

The conceptual basis of light-sheet microscopy dates back to 1903, when Richard Zsigmondy and Henry Siedentopf, introduced the Ultramicroscope, a slit-illumination system that used a thin sheet of light for observation (173). Although this principle was not widely adopted at the time, it was revived in 1993 by Voie and colleagues, who introduced orthogonal-plane fluorescence optical sectioning (OPFOS) for imaging large biological specimens (174). Broader interest in the method emerged after 2004, when Ernst Stelzer and co-workers refined the concept and introduced SPIM as a practical tool for fluorescence imaging of living embryos (175). Both OPFOS and early SPIM implementations commonly used a cylindrical lens to form the excitation sheet, which substantially improved the quality of plane-selective illumination.

The central goal of light-sheet microscopy is to image large specimens rapidly and over extended periods while minimizing photodamage. In this approach, only the plane that coincides with the focal plane of the detection objective is illuminated and the emitted fluorescence is collected by decoupled detection lens. This geometry combines two major advantages: 1) an entire plane can be captured in a single camera exposure, providing the acquisition speed typical of widefield systems and 2) excitation of just the imaging plane reduces autofocus fluorescence and improves the signal-to-noise ratio, similar to the z-sectioning benefit of confocal microscopy.

In most light-sheet microscopes, the optical components remain stationary during acquisition and three-dimensional imaging is achieved by translating the specimen through the light sheet. This is commonly performed using a motorized sample stage with translational axes and in many systems, an additional rotation axis that enables multi-view imaging from different angles. The resulting datasets can then be stitched computationally, which is particularly useful for large specimen.

A major advantage of LSFM is its speed as mentioned before; volumetric datasets that may require minutes to hours on a confocal microscope can often be acquired in seconds to minutes with light-sheet systems.

However, light-sheet microscopy has its own limitations. First, the cost can be substantial, e.g. whole organ antibody labelling and microscope equipment. Second, the data generated by light-sheet microscopy is massive in size, necessitating future and sustainable solutions for data storage, management and analysis. Third, biological samples must be transparent. Due to the inherent opacity of tissues to visible light, consequently, they require processing through a set of techniques known as tissue clearing, which will be discussed below.

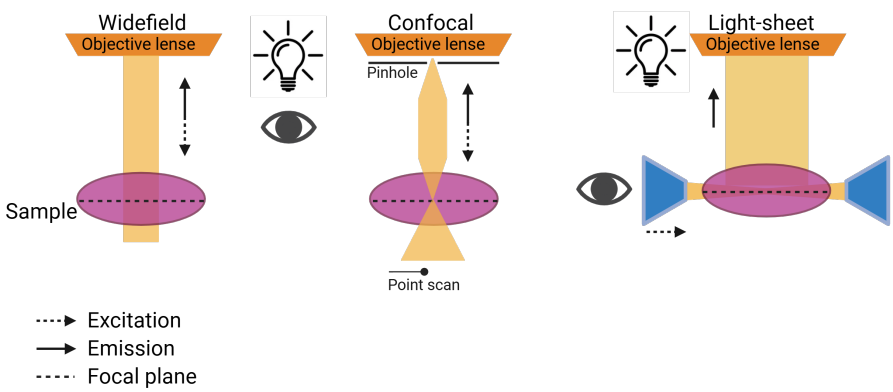

Figure 10. Schematic representation of widefield, confocal and light-sheet microscopes. Created in BioRender.com by NG

As a conclusion, microscopy can be performed on both live and fixed tissues using a wide range of imaging techniques. However, due to the technical challenges associated with live imaging, including specialized instrumentation requirements, maintenance of physiological conditions, phototoxicity and overall sample stability imaging of fixed and thin sections of tissues remains the dominant approach in biomedical research. Therefore, understanding of how fixation and tissue processing affect biological samples helps minimize experimental artifacts and improves the reproducibility and reliability of results. Moreover, careful selection of the appropriate fixative and processing is critical not only to preserve tissue morphology and molecular integrity, but also to ensure compatibility with downstream analyses.

Tissue Fixation

Tissue fixation is a critical first step in preparing any biological sample for downstream analysis. Its primary goal is to preserve molecular architecture and prevent autolysis. Most clinical and research laboratories rely heavily on aldehyde-based fixatives, mainly formalin, paraformaldehyde (PFA) and glutaraldehyde (GA), which preserve tissue by forming covalent cross-links, primarily targeting the primary amine groups of proteins. However, the mechanism of cross-linking differs among aldehyde groups.

Formaldehyde is the active ingredient in both commercial formalin (which usually contains methanol as a stabilizer) and freshly prepared PFA. Fixation occurs through the release of formaldehyde, which reacts primarily with nucleophilic groups on biomolecules. The major targets are lysine ε-amino groups ($-NH_2$), although arginine guanidino groups, histidine imidazole, cysteine thiols and tyrosine and tryptophan residues can also participate in the reaction (176). Formaldehyde additionally reacts with protein N-termini and amino groups present on nucleic acids. Following initial hydroxymethyl adduct formation, formaldehyde promotes the generation of covalent methylene bridges ($-CH_2-$) between neighboring molecules. These crosslinks are most commonly formed between lysine residues on neighboring proteins but can also occur between proteins and DNA or RNA. The crosslinked three-dimensional network stabilizes cellular and tissue architecture by restricting molecular mobility and preserving biomolecular interactions present at the time of fixation (176, 177). In contrast, glutaraldehyde (GA) has two aldehyde groups separated by a sequence of the three methylene groups. Because it is bifunctional, it has the potential to covalently cross-link proteins and stabilize clustered states over variable distances through irreversible cross-linking (177-179).

These chemical differences directly affect how quickly the fixative can penetrate tissue. Formaldehyde penetrates at approximately 1 mm per hour, whereas glutaraldehyde is even slower, often moving at about half that speed (180, 181). To ensure that the core of a sample is fully fixed, tissue blocks must be of adequate size

in relation to the amount of fixative used, with the standard rule of thumb using a fixative-to-tissue volume ratio of at least 20:1.

Recently, there has been growing interest in greener alternatives, particularly formalin-free, alcohol-based (coagulant) fixatives due to their rapid fixation times and their low toxicity. Instead of forming covalent cross-links, alcohols preserve tissue by rapidly dehydrating it and coagulating proteins, essentially locking them in a near-native state (182).

In related work outside the main scope of this thesis, we compared standard aldehyde-based fixatives with alcohol-based fixatives across a variety of mouse organs (**Figure 11,** Paper 5, papers not included in the thesis). When examining standard H&E-stained sections, we observed no discernible differences in morphology between the two methods. However, when we applied these fixatives to sodium alginate–based bioengineered materials (which are known to be challenging to fix with buffered aldehydes) the alcohol-based fixative showed superior performance (182). The ability of alcohol-based fixatives to be used with both native and bioengineered tissues is an important finding as it enables tissue engineered structures developed with alginate to be studied *in situ*.

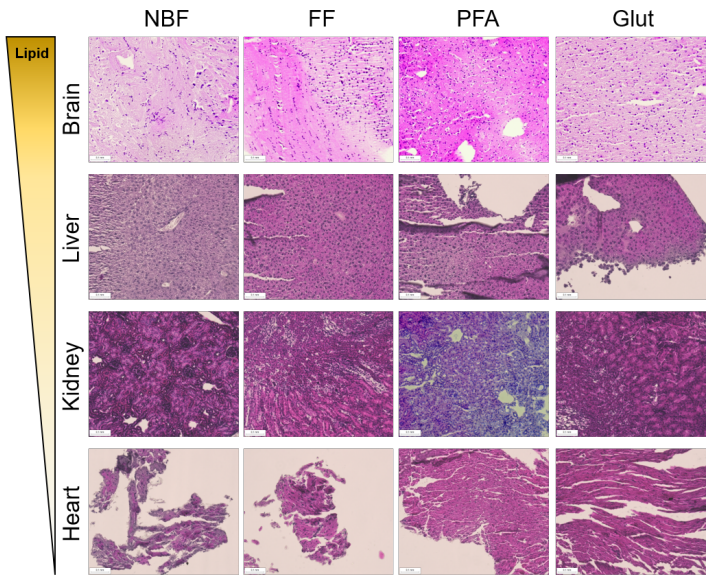

Figure 11. Microscopical images of hematoxylin and eosin (H&E) stained murine organs fixed using neutral buffered formalin (NBF), formalin (FF), paraformaldehyde (PFA) and glutaraldehyde (Glut). Figure reproduced from (Silva *et al*. 2023) with permission

Ultimately, even fixation, which we use routinely on an everyday basis, is not a single universal method. Rather, the choice of fixative must be made based on the specific experimental requirements (183, 184).

Tissue processing

Further preparation of thick, fixed tissues for standard microscopic examination involves tissue processing, which can generally be divided into two main approaches: cryo- and paraffin embedding.

In cryo-, tissue is processed shortly after extraction, sometimes even without prior fixation. The sample is placed in a supporting medium, such as optimal cutting temperature (OCT) and directly frozen for subsequent cryo-sectioning. This method offers several advantages. It is considerably faster than paraffin embedding and allows preservation of certain molecules (e.g lipid), that may be lost or altered during the dehydration steps of paraffin processing. However, cryoembedding also has several disadvantages. Frozen tissue is generally more difficult to section, sections often show higher background and lower morphological quality due to the lack of a dedicated tissue clearing step (i.e. delipidation) and long-term storage can be challenging, as samples usually need to be kept at −80 °C. However, in this thesis, paraffin-embedded tissue was used in most experiments.

The main aim of paraffin embedding is to allow paraffin to penetrate the tissue evenly in order to preserve its architecture and enable sectioning for microscopic analysis. Because paraffin is hydrophobic and immiscible with water, the tissue must first be dehydrated. Dehydration removes intracellular and extracellular fluid and is typically performed using a graded series of increasing alcohol (e.g ethanol) concentrations.(185)

Following dehydration, tissues are cleared by replacing ethanol with an intermediate solvent, most commonly xylene. Because ethanol is not miscible with paraffin, the clearing agent serves as a transitional medium compatible with both ethanol and paraffin, thereby preparing the tissue for the uniform paraffin infiltration.

The final stage is paraffin infiltration, in which the tissue is immersed in warm paraffin for fully infiltration. Once infiltration is complete, the tissue is embedded in paraffin in a defined orientation, depending on how the sample should be visualized microscopically. The duration and conditions of dehydration, clearing and paraffin infiltration must always be adjusted according to tissue type. For example, some bioengineered materials cannot tolerate the standard paraffin temperature of approximately +65°C and therefore require the use of low-melting-point paraffin.

In addition, in studies Paper 4, 5, 6, 7 not included in this thesis, we developed and used a green tissue processing approach in which xylene was replaced with 2-propanol (otherwise referred to as isopropanol). Xylene is a toxic solvent associated with health risks and according to Swedish regulations, requires specific ventilation systems during use. In contrast, 2-propanol is a secondary alcohol with solvent-like properties that can serve as a safer alternative. We validated this greener processing approach in multiple tissue types, organs, embryos, and bioengineered materials,

including samples from human, porcine, rat, chick, and mouse origin. Importantly and similar to traditional histological processing, the duration of each processing step requires optimization depending on the specific tissue type and size of the tissue.

Imaging Thick Tissue

As previously discussed in this thesis, most studies of tissues have traditionally been performed using thin, 2D sections. However, organs are not 2D structures. Even the smallest cells in our body exist in three dimensions and these cells collectively form tissues and organ systems composed of multiple cell types, each with specific physiological functions. This becomes particularly important during disease, where small subpopulations of abnormal cells may be key drivers of the disease, however because of heterogeneity of disease may be difficult to detect using conventional histology alone. Further embryonic development takes place in three dimensions, and therefore embryos would benefit from being studied in their proper 3D context.

This raises a natural question: how can such three-dimensional information be obtained? One possible approach is to section an entire organ, carefully preserve the correct order of all sections and then reconstruct the sample from these serial sections. However, this method is technically challenging. Sections may be lost or damaged, alignment may be imperfect and the overall process is highly labour-intensive. Nevertheless, when performed successfully, serial sectioning historically generated highly valuable maps and atlases with precise spatial information. More recently, advances in synchrotron facilities and X-ray-based microimaging have enabled three-dimensional imaging of formalin-fixed paraffin-embedded (FFPE) samples from a range of organs. However, these facilities remain limited in availability and specialized training is required to obtain high-quality images, especially from biological specimens.

Despite the advances made in microscopy techniques such as confocal, imaging thick biological samples remains challenging because light propagation through tissue is progressively altered by two dominant processes: absorption and scattering. All tissues also show some degree of autofluorescence. In most cases, this is viewed as background “noise” and its signal arises from naturally fluorescent molecules such as collagen, tyrosine, NAD(P)H etc. This background fluorescence, especially in thick samples, reduces image quality by lowering the SNR.

Moreover, most of the tissues have some pigmentation, which contributes strongly to light absorption in tissues. Important absorbing molecules include hemoglobin (in the RBC except crocodile icefish), myoglobin (muscle) and melanin (skin and hair), contributing to tissue colour. To overcome these limitations several decolorization methods have been developed, for example bleaching with hydrogen

peroxide. However, hydrogen peroxide has to be used with caution to avoid damage of tissue structure and can negatively affect fluorescent protein emission. Opacity of tissue to visible light is also a limitation, which will be discussed next.

Tissue opacity to visible light is often explained as a consequence of refractive index mismatch within the sample. Although this explanation is mostly correct, it's not a full picture. A more complete understanding requires asking why does tissue scatter light? As discussed previously, light exhibits both particle-like and wave-like behaviour. However, for understanding scattering, the wave model is the most useful. In the broadest sense, scattering can be defined as the random deviation of a directed flow (for example light waves) from its straight-line propagation.

When light propagates through a material, its oscillating electric field interacts with electrons in atoms and molecules. In most cases, the incoming photon does not have enough energy to induce a real electronic transition or ionization (186). Instead, the electric field transiently displaces the electron cloud, inducing a temporary dipole. The electron cloud then oscillates and re-radiates light (186). Because there is no net loss of photon energy, this process is known as elastic scattering. The scattered light therefore has the same wavelength as the incident light, but its direction may change. This interaction also causes a very small delay in the movement of light through the material (**Figure 12A**). Although each delay is extremely short, many such interactions occur as light travels through different medium (Snell's Law) (**Figure 12B**). This slowing gives rise to the refractive index of a medium. Therefore, refractive index reflects not only molecular density, but also how easily the electrons within a material can be polarized by an electromagnetic field. For example, although water is denser than the lipid-rich cell membrane, the membrane has a higher refractive index because its electrons are more easily polarized.

Scattering is often described as occurring only at interfaces where two materials have different refractive indexes. However, light is actually scattered wherever there are molecules. The important factor is not simply the existence of molecules, but whether the material is optically homogeneous or heterogeneous at the scale relevant to the wavelength of light. In optically uniform materials such as air, water or clean glass, molecules also scatter light. However, because the scatterers are distributed very uniformly, the secondary waves emitted by individual molecules interfere destructively in lateral directions. As a result, very little light is scattered sideways. In the forward direction, however, these waves interfere constructively, allowing light to propagate through the material with minimal loss of directionality. This is why such materials appear transparent.

Biological tissues are fundamentally different because they are not optically uniform. They contain many different components including intracellular and extracellular fluids (RI 1.33) membranes (RI 1.46-1.48), proteins (RI 1.50-1.58), collagen (RI 1.53), each with distinct optical properties (187) (**Figure 11C**). When light travels through thick tissue it scattered many times (188). As a result, the tissue

behaves as if it contains many small light sources that emit light in all directions. This process, known as multiple scattering, gives tissue its typical whitish or cloudy appearance. The size of these inhomogeneous structures also affects how light is scattered. Very small particles, much smaller than the wavelength of visible light, scatter shorter wavelengths more strongly than longer wavelengths. This phenomenon is known as Rayleigh scattering (186). Therefore, longer wavelengths, such as the infrared light used, are scattered less and can penetrate deeper into thick samples. In contrast, larger structures, such as organelles or large proteins, scatter light in a different way, with much weaker dependence on wavelength (Mie scattering). Returning to the original question of why tissue is opaque to visible light, the most accurate explanation is that differences in scattering between different regions of biological material are what produce the diffuse scattering and milky appearance of tissue.

However, the above-described limitations can be overcome using tissue clearing methods (187). Tissue clearing is not intended to prevent scattering completely (this is possible just in vacuum), instead it homogenizes the refractive index throughout the tissue by removing or reducing light-absorbing molecules. (**Figure 12**). As a result, refractive index mismatch is minimized, scattering is reduced, and light can pass more uniformly through the tissue (**Figure 12D**).

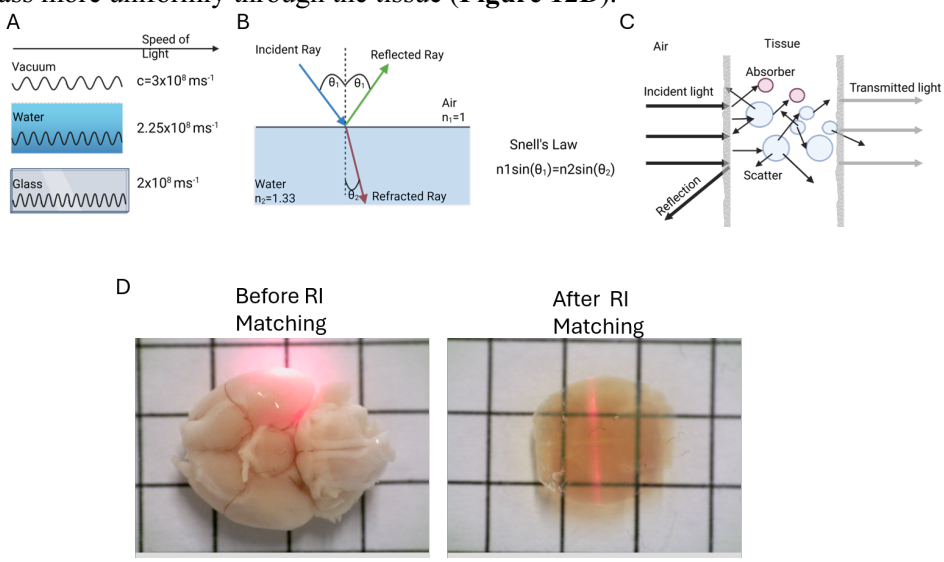

Figure 12. A) Schematic of the speed of light in different media. B) Illustration of Snell's law, showing refraction of light at the interface between two media with different refractive indexes. C) Schematic of light propagation through biological tissue. Schematics created in BioRender.com by NG D) Mouse brain before and after refractive index matching, demonstrating how tissue clearing increases optical transparency and improves light penetration through the sample

Tissue clearing

To reduce light scattering and matching refractive index in biological tissues, a range of clearing methods have been developed. In a very broad sense, a similar effect can also be observed in nature, for example in insects preserved in amber. However, the first tissue clearing method was developed more than a century ago by the anatomist Werner Spalteholz (189). At the beginning of the twentieth century, Spalteholz used a mixture of methyl salicylate and benzyl benzoate to render human organs transparent. Later, modified versions of the Spalteholz method were adopted by embryologists, who replaced methyl salicylate with benzyl alcohol (190).

Over the past two decades, the field of tissue clearing has expanded rapidly, driven by major advances in light microscopy - confocal, 2-photon, particularly light-sheet microscopy and further increasing demand for three-dimensional imaging of intact biological specimens. Modern tissue-clearing methods make it possible to analyse organs and large tissue volumes in their native three-dimensional context with high spatial resolution. By preserving tissue architecture during imaging, these methods reveal structural and cellular relationships that are often lost in conventional 2D sectioning. For example, 3D bone marrow images demonstrated that non-dividing haematopoietic stem cells are located predominantly in perisinusoidal niches(191). In another study, SARS-CoV-2 infection showed a localized, clustered pattern in the ferret upper airways (191). Whereas many earlier studies focused on individual rodent organs, more recent protocols have extended tissue clearing to whole-mouse imaging and are increasingly being adapted for large-animal and human specimens. For instance, recent study on human and whole-mouse samples have shown persistent accumulation of SARS-CoV-2 spike protein along the skull–meninges–brain axis, including the meninges and skull bone marrow, long after infection, suggesting a potential link to chronic inflammation and long-term neurological disease (192). Importantly, this new development has required more than simply prolonging incubation times by development of new strategies for clearing (even combining different clearing methods), labelling and image acquisition in large and structurally complex tissues. Despite these advances, important limitations remain. The size of specimens that can be imaged is still limited, in other words, we cannot fit, for example, an entire human lung into even the largest light-sheet microscope chamber. In addition, large-scale volumetric imaging produces huge datasets, often ranging from a few GB to several TB per sample. This creates major challenges for data storage, management, processing, and quantitative analysis.

Light-sheet microscopy can be used to image living organisms, but this requires thick specimens or tissue to be transparent, or semi-transparent. The majority of tissue clearing methods have been developed for fixed samples. Fixation is a crucial step in many clearing protocols, because the tissue must remain structurally stable during the subsequent removal of lipids. A recent study reported tissue clearing for live animals using tartrazine, a yellow-to-orange, water-soluble monoazo dye

commonly used as a synthetic food colorant, to induce transient and reversible optical transparency in living rodents (193). Another recent study introduced SeeDB-Live, a tissue-clearing method for live imaging that uses high concentrations of bovine serum albumin (BSA) to reduce refractive-index mismatches while maintaining near-physiological osmolarity and tissue viability (194).

However, this thesis focuses on tissue-clearing methods for fixed specimens. More broadly tissue-clearing protocols can be generally classified into 3 different categories: 1) Solvent-based (hydrophobic) 2) Aqueous-based (hydrophilic) 3) Hydrogel-embedding. All the protocols have their pros and cons as shown in the table however in this thesis, solvent based protocols will be discussed in more detail.

Solvent-based tissue clearing

Solvent-based tissue clearing is one of the most widely used clearing approaches because it produces high tissue transparency within a relatively short time. These protocols generally consist of three main steps: dehydration with partial lipid removal, further delipidation, and refractive index matching. Various dehydration agents have been used, but methanol and tetrahydrofuran (THF) are the most common (**Table 3**). In addition to removing water, these solvents also extract lipids. However, further lipid removal is often necessary and is commonly achieved using dichloromethane (DCM). Following dehydration and delipidation, the tissue is reduced to a dense matrix composed mainly of dehydrated proteins, with a refractive index of approximately 1.5. The final step is refractive index matching, for which several solutions have been employed, including benzyl alcohol/benzyl benzoate (BABB), dibenzyl ether (DBE), and ethyl cinnamate. Among these, ethyl cinnamate is considered the least toxic alternative. Nevertheless, although relatively non-toxic, it may dissolve glue and certain other materials. In addition, some tissues require pretreatment before clearing, such as decolorization or bleaching.

As shown in the table below, different solvent-based tissue clearing methods have been developed. However, organic solvent approaches suffer from notable drawbacks, including tissue shrinkage caused by extensive dehydration as well as quenching of endogenous fluorescent proteins (e.g.GFP). GFP and other endogenous fluorescent proteins are known to have reduced fluorescence in methanol-based dehydration and optical clearing protocols (e.g., iDISCO(195)) due to both denaturation and losses in quantum yield. Samples prepared using these types of optical clearing approaches thus require antibody labelling for detection of proteins of interests, which increases both experimental cost and time. To overcome this, alternative strategies have been developed, including the use of longer-chain or branched alcohols as well as heterocyclic compounds for dehydration under controlled pH conditions. For instance, fDISCO utilizes tetrahydrofuran (THF) at +4°C and alkaline pH 9 (196), while 2Eci, another solvent-based clearing method, employs 1-propanol under similar environmental conditions. uDISCO (197) uses

tert-butanol for dehydration and vitamin E as an additive to refractive index matching solution to preserve fluorescence.

Table 3 Solvent based tissue clearing. Overview of commonly used solvent-based tissue-clearing protocols. The table summarizes the fixation methods, dehydration and delipidation solvents employed in each protocol and indicates whether pH control was applied during the clearing process.

Protocol	Fixation	Dehydration	Delipidation	pH regulator	Reference
BABB	PFA	Tert-butanol: ethanol	DCM	-	(198)
3DISCO	PFA	THF	DCM: THF	-	(199)
iDISCO	PFA	THF	DCM: THF	-	(195)
iDISCO+	PFA	Methanol	DCM	-	(200)
iDISCO ace	PFA	Acetone	DCM	-	(199)
uDISCO	PFA	Tert-butanol	DCM	-	(197)
a-uDISCO	PFA	Tert-butanol	DCM	Triethylamine	(201)
Sikin-DISCO	PFA	THF	-	-	(202)
fDISCO	PFA	Tert-butanol	-	Triethylamine	(196)
vDISCO	PFA	Tert-butanol	DCM	-	(203)
Ethanol-ECi	PFA	Ethanol	-	-	(204)
2ECi	PFA	1-Propanol	Ethanol	Triethylamine	(205)
PEGASOS	PFA	Tert-butanol PEG	DCM: Tert-butanol	Triethanolamine	(206)
SHANEL	PFA	Ethanol	DCM	-	(207)

Spectroscopy

As discussed above, light exhibits a wave–particle duality, meaning that it can behave both as a wave and as a particle. As a particle, light consists of photons, each carrying a discrete amount of energy. The energy of a photon is given by Plank's relation, meaning that photon energy increases with increasing frequency and decreasing wavelength. Further the interaction between electromagnetic radiation

and matter can be measured through processes such as absorption, emission, diffraction, resonance and scattering. The study of these interactions is known as spectroscopy.

In this thesis, the primary focus will be on ultraviolet–visible (UV–Vis) and infrared (IR) based spectroscopy.

Ultraviolet–Visible (UV–Vis) Spectroscopy

UV–Vis spectroscopy is a fundamental, non-destructive and label free technique that measures how a sample absorbs or transmits light across the ultraviolet (~190–400 nm) and visible (~400–800 nm) spectrums. At the molecular level, this process is driven by electronic transitions. Functional groups known as chromophores absorb incoming photons, promoting their valence electrons to higher energy states.

While it can be used qualitatively, UV–Vis is predominantly relied upon for quantitative analysis, governed by the Beer-Lambert law. This law describes a linear relationship in which absorbance depends on the concentration of the absorbing molecule and the length of the light path through the sample. In biomedical research, UV-Vis is frequently used due to its speed, low cost and high reproducibility. This method is routinely used for the quantification of nucleic acids and proteins. DNA and RNA exhibit strong absorbance at 260 nm because of the aromatic purine and pyrimidine bases within their structures, whereas protein concentration is commonly assessed at 280 nm, mainly due to absorbance by aromatic amino acids such as tryptophan and tyrosine (208). The A260/A280 absorbance ratio is therefore widely used as a rapid indicator of nucleic acid sample purity. Beyond direct measurement, the technique is the backbone of colorimetric assays. Molecules that lack strong natural absorbance can react with specific dyes or reagents to form coloured complexes, allowing for spectrophotometric readouts in assays evaluating WST-1, LDH release or Bicinchoninic acid assay (BCA).

Recent innovations have also expanded its utility into advanced quality control. For instance, coupling UV-Vis spectroscopy with machine-learning algorithms has enabled the rapid, non-invasive detection of microbial contamination in cell therapies, providing faster sterility assurance (209). Additionally, as explored in Paper 5 not included in this thesis, we successfully utilized UV-Vis to quantitatively monitor the kinetics of hydrogel crosslinking during the chemical fixation of sodium alginate-based bioengineered materials using different chemical fixatives and buffers (**Figure 13**).

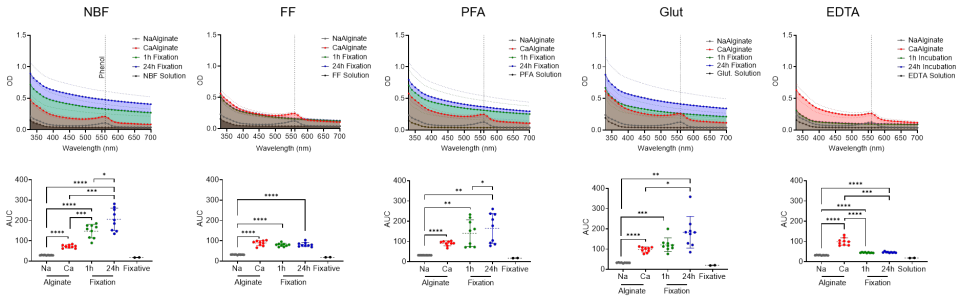

Figure 13. Uv-Vis spectroscopy absorption spectra and AUC analysis of alginate samples following fixation. Uv-Vis absorption spectra were measured across all experimental conditions and fixation time points for neutral buffered formalin (NBF), formalin-free fixative (FF), paraformaldehyde (PFA), and glutaraldehyde (Glut). Spectra are shown for sodium alginate (gray), calcium alginate (red), 1 h fixation (green), 24 h fixation (blue), and pure fixative solution (black). The area under the curve (AUC) was calculated for each condition using the same color coding as in the corresponding UV–Vis spectra. Figure reproduced from (Silva et al. 2023) with permission

Despite its versatility, UV-Vis spectroscopy carries several limitations, largely due to its nature as a bulk analytical technique and lacking spatially resolved chemical or structural information. Furthermore, these optical readouts are highly vulnerable to light scattering, especially from biological samples.

Infrared (IR) spectroscopy

Infrared (IR) spectroscopy is a non-destructive and label free analytical technique utilized to study the molecular structure and chemical composition of a sample. The foundational discovery of infrared light is attributed to Sir William Herschel in 1800, who first detected these wavelengths by measuring temperature escalations beyond the visible red spectrum (210). In contrast to UV-Vis spectroscopy, which probes the electronic transitions of a molecule, IR spectroscopy is vibrational. When infrared radiation interacts with a sample, the energy is partially absorbed, exciting the molecule into a higher vibrational state (211). However, for IR absorption to occur, two strict quantum mechanical and physical conditions must be met: the molecular vibration must result in a net change in the permanent dipole moment, and the energy of the incident IR photon must exactly match the energy gap between the molecule's ground vibrational state and its excited state ($\Delta E=h\nu$) (211). For example, heteronuclear molecules like carbon dioxide or water exhibit changing dipole moments during stretching or bending and are therefore "IR active," whereas homonuclear diatomic molecules like nitrogen or oxygen possess perfectly symmetrical charge distributions that render them "IR inactive."

Because nearly all complex molecules possess distinct, dynamic dipole moments and unique atomic masses, the resulting IR absorption spectrum serves as a highly specific molecular fingerprint. This exceptional specificity allows for the rapid, definitive identification of unknown substances and it is used in diverse applications such as forensics and airport screening.

Historically, early IR instruments were highly inefficient, measuring spectra by individual wavenumbers. This limitation was overcome by the development of the IR interferometer, which captures all infrared frequencies simultaneously to produce a complex optical signal known as an interferogram. To translate this raw, complex signal into a decipherable spectrum, the data undergoes a mathematical transaction known as a Fourier Transform, which converts the signal from the spatial domain into the frequency domain (211). A natural analogue of this mathematical process occurs in the human auditory system. When the ear receives a complex, overlapping mixture of sounds, the mechanical structure of the cochlea functions like a biological Fourier transformer, separating the incoming waveform into its constituent frequencies. This enables the brain to distinguish specific sounds within the mixture. As a result, we can perceive individual voices even within complex music: for example, in Thomas Tallis's *Spem in alium*, where 8 choirs sing simultaneously, yet we are still able to focus on and follow individual vocal lines if needed. The integration of this mathematics gave rise to Fourier-Transform Infrared (FTIR) spectroscopy, dramatically revolutionizing chemical analysis by enhancing both signal-to-noise ratios and data acquisition speeds (212).

While FTIR initially was used in pure chemistry, its application in biomedicine has expanded exponentially in the last few years due to its exceptional sensitivity to the biochemical makeup of tissues. The technique is capable of identifying and distinguishing the distinct vibrational signatures of proteins, lipids, carbohydrates and nucleic acids (**Table 4)**, making it an potential tool for detecting subtle pathological changes at the molecular level (212). For instance, recent studies evaluating FFPE lung sections from bleomycin-induced pulmonary fibrosis models demonstrated that Principal Component Analysis (PCA) of FTIR spectra can successfully cluster tissues based on the duration of disease progression (213). Similarly, in Paper 1 not included in this thesis evaluating therapeutic interventions on bleomycin-induced fibrotic lungs, we used FTIR (**Figure 14**) to assess collagen deposition across groups. This label-free approach enabled quantitative evaluation of fibrosis and treatment-associated changes in extracellular matrix composition.

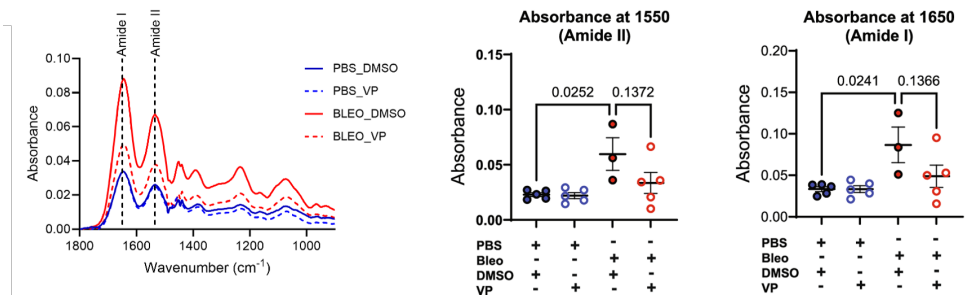

Figure 14. FTIR spectra and peak quantification from lung tissue sections of one cohort from PBS or Bleomycin-treated animals who received VP or DMSO controls. n = 5 for PBS, n = 3 for BLEO-DMSO and n = 5 for BLEO-VP. Figure reproduced from (Wagner et al. 2025) with permission.

Table 4 Main FTIR peaks in biological tissue

Wavenumber (cm^{-1})	Peak Position (typical)	Assignment	Biomolecule / Origin	Notes
3600–3200	~3400	O–H stretching	Water, carbohydrates	Broad; hydrogen bonding
3080–3015	~3070	=C–H stretching	Unsaturated lipids	Olefinic groups
1745–1735	~1742	C=O stretching (ester)	Lipids	Phospholipids, triglycerides
1695–1600	~1650	Amide I (C=O stretch)	Proteins	Secondary structure
1660–1650	~1654	α-helix (Amide I)	Proteins	Dominant component
1640–1625	~1635	β-sheet (Amide I)	Proteins	Strong H-bonding
1400–1390	~1395	COO^- symmetric stretch	Amino acids, fatty acids	Ionization-sensitive
1380–1370	~1375	CH_3 symmetric bending	Lipids, proteins	Methyl groups
1335–1315	~1320	Amide III	Proteins	Structure-sensitive
1245–1230	~1240	PO_2^- asymmetric stretch	Nucleic acids, phospholipids	DNA/RNA backbone
1090–1080	~1085	PO_2^- symmetric stretch	Nucleic acids	DNA/RNA marker
1035–1020	~1030	C–O / C–O–C	Carbohydrates	Fingerprint region

Despite these analytical strengths, standard FTIR is a “bulk” analysis technique and therefore lacks spatial context. Over the past two decades, this limitation drove the coupling of IR spectrometers with optical microscopes to create IR microspectroscopy. This union allows for the generation of hyperspectral images, where each pixel in the spatial field contains a complete, spatially resolved IR absorption spectrum. However, traditional FTIR and IR microspectroscopy suffer from critical limitations when applied to biological tissues, most notably the strong absorption of water. The bending vibrational mode of liquid water near 1640 cm^{-1} directly overlaps with the Amide I band of proteins, entirely masking crucial

secondary structural data (214). Consequently, biological samples cannot be easily analyzed in their native, fully hydrated states. Tissues must undergo standard histological processing, including rigorous chemical fixation, dehydration and delipidation (as above in **Figure 14**), which alters their native architecture and volumetric dimensions. Furthermore, the spatial resolution of traditional IR microspectroscopy is strictly governed by the Abbe diffraction limit, restricting resolution to roughly 3–20 μm depending on the wavelength. Highly heterogeneous biological samples also frequently suffer from pronounced Mie scattering artifacts. Ultimately, while FTIR is a formidable analytical tool, simultaneous interrogation of diverse biological molecules in their fully hydrated, native state with high spatial resolution remains impossible utilizing traditional IR spectroscopy alone.

O-PTIR

To overcome the above-mentioned limitations of infrared based techniques, optical photothermal infrared microscopy (referred as OPTIR, O-PTIR or Mid-infrared Photothermal Microscopy - MIP) has recently been developed. The basic principle of O-PTIR can be understood as a pump–probe microscopy approach, in which two co-linear laser beams are used: a tuneable mid-infrared beam (pump), and a shorter-wavelength visible beam (probe) (**Figure 15A**) (215). The infrared pump provides photothermal expansion, whereas the visible probe detects the physical changes induced by infrared absorption. Because detection is performed with visible light, the spatial resolution is no longer limited by the long wavelength of IR.

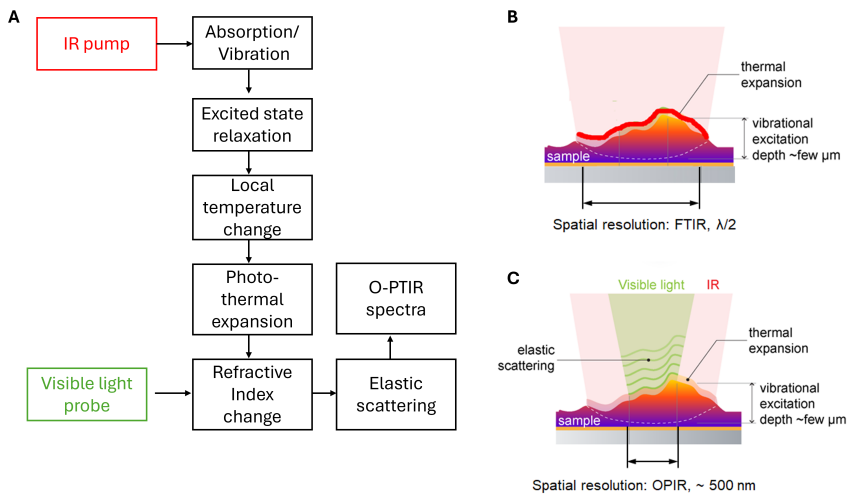

Figure15. A) Schematic of major mechanism of OPTIR work B,C) schematic of O-PTIR microscopy on biological sample

However, it is important to understand how exactly O-PTIR operates. After the sample is illuminated with mid-infrared radiation, molecules absorb light and cause vibration using the same principle as other IR based techniques. After excitation,

the absorbed energy is predominantly dissipated through nonradiative relaxation, converting vibrational energy into heat (216). This produces a localized temperature increase in the irradiated and absorbing/vibrating region. Therefore, the infrared-absorbing/vibrating structure itself becomes the source of the photothermal signal. This localized temperature rise induces several physical changes in the sample. These include thermal expansion, photomechanical pressure (Grüneisen parameter) and refractive index changes (217) (**Figure 15 A-C**). Among these effects, thermal expansion and refractive-index changes are particularly important for O-PTIR detection because both directly influence the scattering of the visible probe beam (217). As the local temperature increases, the absorber undergoes a small expansion, accompanied by changes in density and polarization (218). These changes are often approximately proportional to the temperature increase, allowing the visible scattering response to be used as an indirect measure of infrared absorption(215). Thus, when the infrared pump is absorbed by the sample, the resulting photothermal expansion and refractive-index modulation alter the scattering of the visible probe beam, producing a detectable signal that reflects the local infrared absorption(215, 218). Therefore, O-PTIR, the visible probe beam does not directly detect infrared light. Instead, it senses the transient optophysical changes caused by infrared. Further the O-PTIR signal is commonly obtained by measuring the difference in visible scattering intensity between the IR-on and IR-off states (218). Thus, the contrast generated in O-PTIR reflects both vibrational absorption by molecular bonds and the surrounding microenvironmental properties

O-PTIR was first adopted in materials science for the chemical characterization of polymers, composites and coatings as a label-free chemical mapping with high molecular specificity with submicrometer spatial resolution overcoming FTIR microscopy. However, its application was expanded into life science, O-PTIR has been successfully used to analyze hydrated living cells from pancreatic and breast cancer 2D cell cultures distinguishing between different parts of the cell as well as they were able to distinguish amide I band from living cells in aqueous solution, which with FTIR microscopy is not possible (219). In addition, another study showed that O-PTIR measurements were possible in C. elegans and could even distinguish between different parts of the nemotid (215). However, both 2D cell cultures and C. elegans are semi-transparent, whereas the majority of tissues are not transparent, raising the question of whether tissue opacity interferes with spectral acquisition. Furthermore, both of these experiments were terminal endpoint analyses; therefore, the extent of cellular or tissue-level damage following O-PTIR imaging remained unknown. OPTIR thus holds potential in assessing biological samples but the limitations previously listed and other open questions regarding complex biological samples are important to understand prior to this approach being used in biomedical research.

Research Aims of the thesis

Multimodal tissue analysis is increasingly recognized as a strategy to maximize extracted data from biological samples, enabling use of the same sample across different modalities. However, the rapid development of novel methodologies necessitates careful validation of their compatibility, both with one another and with established workflows as well as within specific disease contexts, to ensure preservation of tissue integrity, signal fidelity and interpretability across modalities. Therefore this thesis aims to leverage and evaluate recent advances in multimodal tissue analysis for use in diagnostic pathology (paper I and III) as well as in therapeutic evaluation (paper II). It covers the use of both live (paper I and II) and fixed (paper III) tissues and organisms

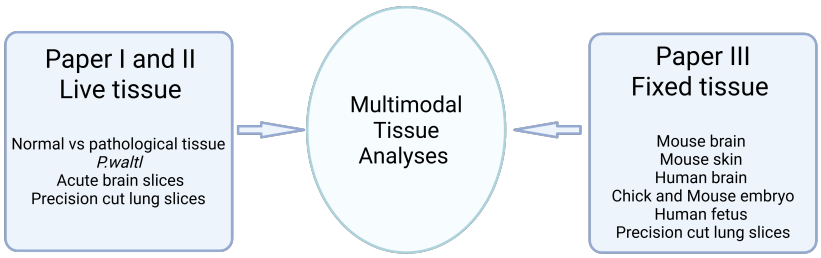

- Evaluate the capabilities of O-PTIR on fully hydrated, non- fixed and-processed normal and diseased tissue biopsies (Paper I)
- Characterize the extent of photothermal-induced damage following thermal expansion in living tissue after O-PTIR imaging (Paper I)
- Determine the optimal post-vibratome sectioning recovery timeline for PCLS (Paper I and II)
- Develop a novel organic solvent-based tissue clearing method that preserves endogenous fluorescence protein signals in large tissue constructs (Paper III)
- Establish feasibility for multimodal downstream analysis after forward and reverse optical clearing of large tissue samples (Paper III)

Methodology

This section will provide key methods used in this thesis. However for more details please refer to the papers amended to this thesis.

Animal Models

Paper 1

Mouse

To compare healthy and diseased brain tissue regions, we utilized the APP/PS1 transgenic mouse model, one of the most widely used models of Alzheimer's disease. This model is characterized by progressive amyloid-β plaque deposition, primarily in the cerebral cortex and hippocampus, recapitulating key pathological features of the human disease. Amyloid plaques begin to appear at 3 month post gestation ages and increase in abundance with disease progression. The timeline of amyloid pathology development in the APP/PS1 mouse model is shown in **Figure 16**. APP/PS1 mice (hAPPswe, PSEN 1dE985Dbo/Mmjax) were obtained from Jackson Laboratories, USA, and all mice were screened for the presence of the human APP695 transgene by PCR. All mouse experiments were compliant with the requirements of the Ethical Committee of Lund University (M11908–19).

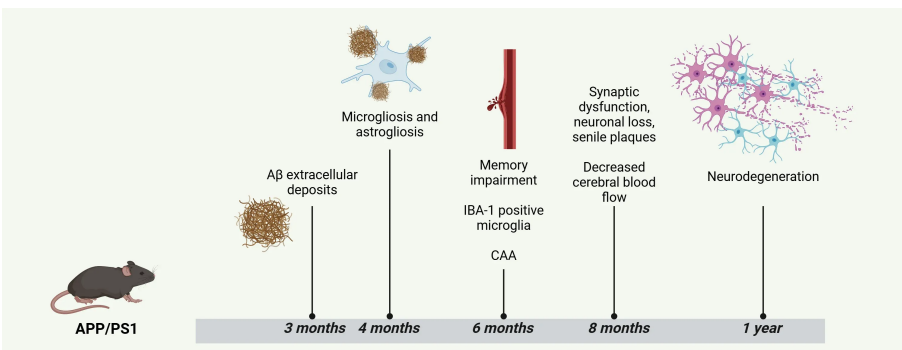

Figure 16. Timeline of APP/PS1 mouse model

Pleurodeles waltl

To monitor potential damage induced by O-PTIR imaging, we utilized wild-type Pleurodeles waltl embryos. Embryos at developmental stage 34 (11 days post-fertilization, dpf) were obtained from the colony maintained at Lund University. According to Swedish regulations (Jordbruksverkets föreskrift L150, §5), experiments involving vertebrate embryos prior to the onset of independent feeding do not require Institutional Animal Care and Use Committee approval. The selected developmental stage precedes independent feeding.

Embryos were reared in conditioned tap water at +20–22°C (55 g Tetra Marine Salt, 15 g Ektozon salt, and 2.5 mL Prime water dechlorinator per 100 L water). For imaging, embryos were manually removed from their protective jelly coat using fine-tip forceps at 10 days post fertilization (dpf). At 11 dpf (stage 34), embryos were anesthetized in 0.025% tricaine prepared in conditioned tap water (pH 7.0). Once fully anesthetized, embryos were transferred to a microscope slide and subjected to O-PTIR imaging. Following imaging, embryos were returned to conditioned tap water (pH 7.0) and allowed to continue developing into larvae. Subsequent monitoring of larval development and morphology was performed to assess any imaging-induced damage.

Paper 2

Lung tissue was obtained from healthy C57BL/6J mice (n = 4). In line with the 4-R principles, we utilized excess tissue from animals scheduled for euthanasia for tissue harvest in other studies. Mice were anesthetized via an intraperitoneal injection of sodium pentobarbital (40–50 mg/kg) prior to organ harvest. Specific preparation of mouse lung tissue (e.g. agarose instillation for PCLS or whole organ fixation) are described below for each specific experimental section.

Paper 3

Mouse

LepR-Cre x tdTomato Mouse

All animal procedures were carried out in accordance with the recommendations of the Canadian Council on Animal Care (CCAC) and have been approved by the local McGill University Animal Care Committee. LepR-Cre (220) mice were crossed with tdTomato (Ai9-lsl-tdTomato) reporter mice to generate mice expressing tdTomato in LepR neurons (LepR-Cre x tdTomato) (221).

Lectin and Dextran labelling

Adult male, C57BL/6 mice (10-12 wks. old, The Jackson Laboratory) were used for vascular labeling and permeability assessment. To evaluate permeability, mice received a tail vein injection of tetramethylrhodamine conjugated dextran, (10k Da, lysine fixable, catalog number: D1817, Invitrogen/Thermofisher) at 150uL per mouse (20mg/mL in sterile PBS). The following day (approximately 20 hours later) mice received a tail vein injection of fluorescently conjugated Lycopersicon Esculentum (Tomato) Lectin (DyLight® 649, 1 mg, catalog number: DL-1178, MJS Biolynx) at 100ul per mouse (1mg/mL, as supplied by manufacturer) to label vasculature. Fifteen minutes following lectin administration, mice were anesthetized with a ketamine (50mg/kg) and xylazine (5 mg/kg) cocktail and transcardially perfused with 0.9% NaCl followed by 10% formalin 30 min post lectin administration. Brains were post-fixed overnight at +4°C in the same fixative, shielded from light and with gentle agitation. The next day, brains were transferred to sterile PBS and stored at +4°C until whole brain clearing. Mice were deeply anesthetized with a ketamine (100mg/kg)/xylazine (10 mg/kg) cocktail and transcardially perfused with 0.9% NaCl followed by 10% formalin. All procedures were in accordance with the Canadian Council on Animal Care (CCAC) and approved by the McGill University Animal Care Committee (AUP # MUHC-5703).

Microvessel isolation and transplantation

Microvessels (MVs) were isolated from epididymal adipose tissue of male GFP rats (SD-Tg(UBC-EGFP)2BalRrrc;RRRC). Adipose tissue was mechanically dissociated by mincing and further digested with 2 mg/ml collagenase type I (Worthington, LS004197) in DPBS containing 0.1% BSA (A9418, Sigma-Aldrich) and 1 mg/ml DNase-1 (DN25, Sigma-Aldrich) at +37°C under agitation for 6.5 minutes. Digested tissues underwent size-selective sieving as previously described in (222) to separate MV fragments from large tissue debris and single cells. After centrifugation at 210 g for 5 min, MVs were resuspended in 3mg/mL rat tail type 1 telocollagen gel (354249, Corning) at a density of 20,000 MVs/mL. MV collagen constructs were polymerized by incubation at +37°C for 30 min. MV construct implantation was adapted from a previous publication (223). Briefly, MV constructs were implanted into the dorsal skin fold of male B6.129S7-Rag1tm1Mom/J (Rag1-/-) mice fitted with a titanium window chamber (SM100, APJ trading). One day prior to implantation, clippers and Nair cream were used for hair removal of the dorsal skin. The explantation timepoint was determined using serial intravital imaging of the construct within the window chamber using a Zeiss AxioZoom.V16 upright macroscope. Imaging was performed until the first day implanted microvessels became perfused with host blood. The construct shown was implanted for 7 days. To harvest the constructs and underlying host skin, mice were euthanized and the titanium window chamber was removed. Collagen hydrogel with underlying

skin was excised and fixed in 4% PFA (28908, PierceTM) on an orbital shaker overnight at 4°C. After 3 PBS washes for 1 hour at RT, samples were permeabilized in 2% Triton-X 100 (X100, Sigma-Aldrich) in PBS (Sigma-Aldrich, P3813) for 24 hours at RT. Next, grafts and skin tissue were blocked with 10% normal donkey serum (S30-M, Sigma Aldrich), 1% Triton-X 100, 2.5% DMSO (D136, Fisher Chemical) for 2 days at 4°C. Primary antibodies (Paper III, Supplemental Table 3) against rat and mouse CD31 (AF3628, R&D Systems) were diluted in 1% normal donkey serum, 0.2% Triton-X 100, 2.5% DMSO in PBS and incubation was done for 4 days at 4°C. Samples were then rinsed with washing buffer (3% NaCl and 0.2% Triton-X 100 in PBS) 3 times for 1 hour at RT and then overnight at 4°C. Secondary antibodies (A-21447, Invitrogen) were then diluted in 1% normal donkey serum, 0.2% Triton-X 100, 2.5% DMSO and incubated with the graft and skin for 2 days at 4°C. Samples were rinsed with washing buffer for 1 hour 3 times at RT and overnight at +4°C and then PBS 3 times for 15 min. Following washes, samples were incubated with DAPI (CST) 1:1000 dilution (0.1 mg/mL) for 1 hour at room temperature and then were rinsed with PBS 3 times for 1 hour. Finally, samples were embedded in 1.5% low-melting-point agarose (A9414, Sigma- Aldrich, USA) to facilitate handling and ensure stable positioning during mounting on the light-sheet microscope arm.

Murine embryos

Murine embryos from both McGill University and Lund University were used. Pregnant female WT mice were sacrificed by cervical dislocation. Embryos were dissected at day 10 and day 15 of gestation and directly placed in 10% NBF(Sigma-Aldrich, catalog number: HT501128-4L) for 48h at +4°C for fixation. Experiments were approved by the Malmö/Lund (Sweden) Ethical Committee for Animal Research (ethical permit numbers M173–19 and M2780–24), in accordance with guidelines from the Swedish Board of Agriculture. All experiments were performed in line with the laws and regulations issued by the Swedish Board of Agriculture.

C57Bl/6 male and female mice were mated overnight, and the plug was checked the next morning. Appearance of the plug is considered as 0.5 days post coitum (embryonic day 0.5 (E 0.5). The pregnant dams were sacrificed at E15.5. The embryos were dissected out, washed in cold PBS and fixed in 10%NBF solution for 48h hours at 4°C.All animal work was conducted according to the Canadian Animal Care Guidance with approval by the Animal Care Committee of McGill University Health Center Research Institute, ACC protocol 7606.

Chicken embryos

Chick embryos were acquired from commercially purchased fertilized eggs and incubated at +37.5°C until embryonic days E3 and E5. Work on chick embryos followed the guidelines set by the Malmö-Lund Ethics Committee for the use of laboratory animals and were conducted in accordance with the European Union directive on the subject of animal rights (ethical approval nr. 5.8.18-00878/2025).

Human tissue

Human fetal tissue was obtained from elective abortions at Skåne University Hospital, Sweden (ethical approval Dnr 6.1.8-2887/2017).

Human embryos were collected in a custom-made hibernation medium (Life Technologies). Embryonic/fetal stages were determined by ultrasonography. Embryos were dissected for the selected tissue (trunk part of the embryonic body), transferred to 4% PFA and fixed at +4°C overnight. Following fixation, fetus tissue was permeabilized in Triton X-100 for 1 h at room temperature. Samples were then incubated with primary antibodies diluted in a blocking solution consisting of 15 mL phosphate-buffered saline (PBS), 1 mL dimethyl sulfoxide (DMSO) and 4 mL fetal bovine serum (FBS). Mouse anti-HNK-1 antibody (DSHB, clone 3H5) at a dilution of 1:10 was used as a primary antibody. Primary antibody incubation was performed for 7 days at room temperature with continuous agitation.

Following primary antibody incubation, samples were washed five times for 30 min each in PBS containing Tween-20 (PBS-T), followed by three 30-min washes in PBS. Samples were subsequently incubated with goat anti-mouse Alexa Fluor 568 secondary antibody (Thermo Fisher Scientific, A11004; 1:1000 dilution) for 72 h at room temperature with continuous agitation. All primary and secondary antibodies were diluted in the same blocking solution.

After secondary antibody incubation, samples were washed three times for 15 min in PBS . Prior to tissue clearing, human fetal samples were bleached in 3% hydrogen peroxide for 24 h at +4°C with continuous agitation. After bleaching, samples were processed for PROTEUS tissue clearing described below.

PCLS Generation

Since our initial goal was to monitor temporal changes in specific airways and their surrounding alveolar spaces for Paper I,II,III and Paper 2 not included in the thesis, it was essential to maintain these structures in an open state to reliably identify the same region during live imaging. To preserve alveolar architecture and facilitate

tissue slicing, 1.5% low-melting-point agarose (A9414, Sigma- Aldrich, USA) was used. Precision-cut lung slices (PCLS) of 300 µm thickness were prepared using a vibratome (Campden Instruments, 7000smz-2).

Slices were cultured as previously described (59) in DMEM-F12 medium supplemented with 1% penicillin/streptomycin and 0.1% fetal bovine serum and maintained in a standard humidified incubator (37 °C, 5% CO_2). A 4-mm biopsy punch was used to generate slices of uniform size, which were cultured individually in 100 µL of complete medium in 96-well plates, with daily medium replacement (one 4 mm diameter slice per well).

NucView® 488 & RedDot™ 2 Staining

Due to the preservation of native lung architecture and resident cell populations, PCLS offer a powerful tool for visualizing and studying cell types and their native microenvironment using a range of microscopy-based techniques. Moreover, because PCLS can be maintained *ex vivo* for extended periods and lung in particular has higher transparency than other internal organs, they provide an excellent platform for live-cell imaging.

A recent study (88) monitored early apoptotic activity during alveologenesis in PCLS by qualitatively assessing caspase-3 activity using NucView™ 488 (Biotium; Cat. No. 30029-T). However, in the present work, our aim was to simultaneously monitor early apoptosis as well as membrane-compromised (late apoptotic/necrotic) cells over time in living PCLS. To achieve this, we employed the NucView® 488 & RedDot™ 2 Apoptosis & Necrosis Kit (Biotium; Cat. No. 30072).

The NucView™ 488 Caspase-3 substrate is a fluorogenic probe that enables real-time detection of caspase-3/7 activity in intact cells. This substrate consists of a DNA-binding dye coupled to the DEVD peptide sequence; DEVD is a synthetic four-amino-acid peptide sequence (Asp-Glu-Val-Asp) that acts as the highly specific, preferred cleavage site for activated caspase-3/7. In its intact form, the dye is non-fluorescent and unable to bind DNA. Upon entering the cell, active caspase-3/7 cleaves the DEVD peptide, releasing the dye, which then translocates to the nucleus and emits bright green fluorescence upon DNA binding. This allows simultaneous detection of caspase activity and visualization of nuclear morphology in apoptotic cells. Unlike FLICA-based assays, which rely on irreversible caspase inhibitors, NucView 488 does not interfere with enzyme activity, enabling continuous, real-time monitoring.

To identify membrane-compromised cells, RedDot™ 2 was used. This far-red fluorescent dye is impermeable to intact cell membranes and selectively stains nuclei of dead or late apoptotic cells. Its emission at ~695 nm (Cy®5 channel) is spectrally well separated from NucView 488, allowing multiplexed imaging.

For staining, RedDot™ 2 (200X stock) was first diluted to 20X by mixing 1 µL of stock solution with 9 µL of DMEM-F12 medium. For each 200 µL of staining solution, 5 µL of NucView 488 substrate and 5 µL of the diluted RedDot™ 2 were added, resulting in final concentrations of 5 µM NucView 488 and 0.5X RedDot™ 2. The staining solution was applied to PCLS and incubated at room temperature for 30 minutes. Subsequently, samples were washed three times with fresh DMEM-F12 medium (5 minutes per wash) to remove excess dye prior to imaging.

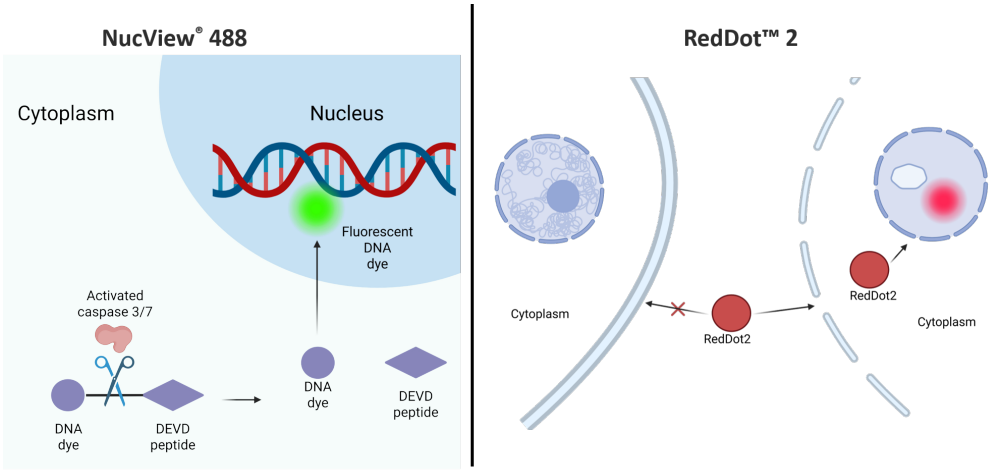

Figure 17. Schematic of NucView® 488 & RedDot™ 2 Staining. Created in BioRender.com by NG

Live imaging

The majority of tissue imaging is done on fixed samples, which are non-viable and therefore don't fully show dynamic cellular processes. However, capturing cellular dynamics in real time remains of hight interest. As discussed in this thesis, imaging of fixed tissues presents several technical challenges. Live cell/tissue imaging introduces additional layers of complexity, requiring careful experimental design and optimization prior and during imaging.

The main goal of live cell/tissue imaging is to image tissue without compromising viability, causing minimal damage, and maintaining conditions as close as possible to the *in vivo* scenario. Therefore, several considerations must be taken into account. First is the choice of labeling methods compatible with live imaging, preferably using longer wavelength excitation. Second is the selection of the microscope, ideally equipped with a live imaging chamber to control CO_2 and temperature during imaging.

Third is reducing phototoxicity during image acquisition; therefore, the lowest possible laser intensities and shortest exposure times should be used. However, in some cases, increasing the gain is essential to improve the signal-to-noise ratio.

In our experiments on PCLS live imaging, we used a Leica STELLARIS 5 confocal microscope (Leica, Germany). Prior to imaging, the live imaging chamber was turned on and allowed to reach +37°C and 5% CO_2. The PCLS were then placed on a 35 mm glass-bottom imaging dish (Ibidi) containing DMEM-F12 medium supplemented with 1% penicillin/streptomycin and 0.1% fetal bovine serum.

For laser setup, unstained control samples were used to avoid saturation in stained samples. FITC and Cy5 laser settings were set to 15% and 6% excitation intensity, with gains of 107 and 29 and an exposure time of 10 ms. Identical laser settings were used for all experiments and across all time points with a 10× dry objective (NA = 0.4). Z-stacks of approximately 140 µm total thickness were acquired with a z-step of 5 µm. The Z-stack size, along with exposure time and laser settings, were carefully optimized to minimize tissue toxicity as much as possible. All images From Paper I and II are deposited online in BioImage Archive (224) accession number : S-BIAD1284.

Quantification of Apoptosis and Cellular Membrane Damage

Confocal image analysis was performed in ImageJ using the in-built Analyze Particles function. Threshold values were defined separately for each fluorescence channel and subsequently applied consistently across all images and experimental conditions. To restrict quantification to regions with optimal image quality, an approximately 50 µm-thick volume was manually selected from the interior of each PCLS, avoiding poorly focused or peripheral tissue regions. Within this volume, every second z-plane was analysed to avoid double counting of individual cells, given our 5 µm z-step interval. For each condition, particles with cross-sectional areas between 25 and 85 µm² were quantified. This range corresponds approximately to nuclear diameters of 4.5-10.5 µm, covering to be approximately 6-7 µm nuclear size range in distal murine lung tissue (225). In addition to particle counts, other parameters such as cross-sectional area, circularity and solidity were extracted and evaluated.

Water-Soluble Tetrazolium Salt Assay

Tissue viability was evaluated by measuring metabolic activity using the water-soluble tetrazolium salt WST-1, a cell-permeable reagent which is reduced on the

membrane of mitochondria in living cells (226). Following intracellular cleavage of WST-1 by cellular mitochondrial dehydrogenases into formazan, which is released into the surrounding culture medium and can be quantified colorimetrically using a standard UV-visible plate reader (227). Because formazan production reflects mitochondrial enzymatic activity, absorbance values are generally proportional to the number and metabolic activity of viable cells. For the assay, 1.5 mm biopsy punches of murine organs were incubated in a mixture containing 90 µL of culture medium of DMEM-F12 and 10 µL of WST-1 reagent (Roche, Sigma-Aldrich, USA). Samples were maintained for 1 h at +37°C in a humidified incubator with 5% CO_2 (227). Following incubation, optical density of the supernatant was measured at 440 nm and 650 nm using an Epoch plate reader (BioTeck, USA). Absorbance at 440 nm was used to quantify WST-1 conversion by metabolically active cells, whereas the 650 nm measurement served as a reference wavelength to correct for nonspecific background absorbance. Cell culture medium of DMEM-F12 with WST-1 and without tissue was included as a negative control.

Lactate Dehydrogenase Release

LDH is a soluble cytosolic enzyme that is released extracellularly when the plasma membrane is compromised, making it a widely used indicator of cell membrane damage and cytotoxicity (228). Therefore, increased LDH levels in the culture medium reflect reduced cellular integrity and can be used to assess tissue injury. The release of lactate dehydrogenase (LDH) was assessed according to the manufacturer's protocol using the Cytotoxicity Detection Kit (Roche, Germany) Briefly, 10 µL of supernatant culture media from 4 mm PCLS was collected 30 min after slicing and prior to O-PTIR imaging ("0 h") and after 24 and 48 h and then stored at −20°C until analysis. For analysis, 2 µL of collected supernatant or fresh cell culture media, used as a background control, was gently mixed with 98 µL of LDH reaction gently mixture while avoiding bubble formation. The mixture was incubated for 1 h at room temperature, protected from direct light. Subsequently, the optical density was measured at 492 nm with a reference wavelength of 650 nm using a multiwall plate reader (Epoch, BioTek, USA).

O-PTIR

Optical Photothermal Infrared Spectroscopy of E15.5 mouse embryo

For O-PTIR microspectroscopy, 10 µm tissue sections were mounted on standard histological glass substrates, deparaffinized and washed with double de-ionized water. Measurements were performed using a mIRage system (Photothermal Spectroscopy Corp., Santa Barbara, CA, USA) at MJOLNIR – the MAX IV Joint Offline Lab for Nano Infrared Spectro-Microscopy (MAX IV Laboratory, Lund,

Sweden). The system employs a pulsed, tunable quantum cascade laser (QCL) operating at a 100 kHz repetition rate as the infrared source, inducing localized photothermal expansion in the sample. This expansion is detected by a co-aligned 532 nm probe laser, enabling quantitative absorption measurements. O-PTIR images were acquired at 1540, 1740 and 1656 cm-1. O-PTIR spectra were collected in the range of 1450–1780 cm^{-1} using an avalanche photodiode (APD) detector. The IR and probe laser powers were set to 22% and 0.5%, respectively, following optimization described in Paper I. Each spectrum represents the average of six scans to improve the signal-to-noise ratio. Background spectra were collected from an inbuilt internal reference. Further methodological details are provided in the cited references. The acquired spectra were analysed using Quasar-M data mining software. A linear baseline correction was applied to remove systematic offsets, followed by vector normalization to account for variations in overall signal intensity. To enhance discriminative spectral features, Savitzky–Golay smoothing was applied using a 13-point window and a second-order polynomial.

eGFP tissue phantom dehydration

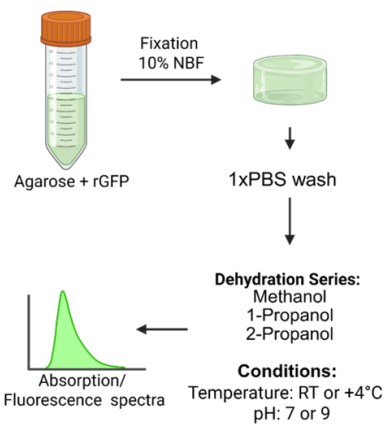

Figure 18. Schematic of eGFP tissue phantom dehydration experimental overview. Created in BioRender.com by NG

A 3% low-melting point agarose (A9414, Sigma-Aldrich, USA) solution was prepared by dissolving the powder in deionized water and heating via microwaving until it was visually clear. The solution was then cooled to approximately +40°C before recombinant Green Fluorescent Protein (RayBiotech) was gently mixed by manual swirling into the liquid agarose to ensure homogeneous distribution. The rGFP-agarose mixture was immediately pipetted into a 96-well polystyrene microplate (833924, Sarstedt) and subsequently placed at +4°C for 30 minutes. Following complete solidification, the rGFP-agarose gels were chemically fixed by 10% Neutral Buffered Formalin (HT501128-4L, Sigma-Aldrich) for 1 hour at room temperature. The fixed gels were then washed three times with a 1x Phosphate-Buffered Saline (18912-014, Gibco) solution (5 minutes per wash). The initial fluorescence intensity of the fixed, hydrated gels was measured immediately after the final PBS wash using a Cytation5 multimodal plate reader (Biotek, Winooski, Vermont) with excitation of 395nm and emission range of 488-700nm with a 10nm step size. Next, a gradual dehydration series was performed by replacing the PBS with increasing concentrations of organic solvents.

Three different alcohols methanol (67-56-1, Fisher Scientific), 1-propanol (71-23-8, Thermo Scientific), and 2-propanol (67-63-0, Fisher Scientific) were tested. Gels were incubated in concentrations of 20%, 40%, 60%, 80% and 100% for 1 h and 100% overnight at room temperature or +4ºC at each, covered and wrapped with parafilm for overnight incubations. All alcohol solutions used in the dehydration series were adjusted at each concentration to pH values of 7 or 9 using 1M NaOH using a pH meter (Fisher Scientific). Fluorescence intensity was quantified after each dehydration step using a Cytation5 plate reader as previously described.

PROTEUS tissue clearing

The PROTEUS tissue clearing protocol was performed using freshly prepared solutions comprised of molecular biology grade 2-propanol (Fisher Bioreagents), deionized water, 1M sodium hydroxide (NaOH), dichloromethane (DCM) (Sigma-Aldrich), and ECi (Sigma-Aldrich). The pH of a graded series of 2-propanol solutions (20%, 40%, 60%, 80%, and 100%) was adjusted to ~9.0 using 1M NaOH. The tissue dehydration series was then carried out at +4°C under light-protected conditions with constant rolling with 50 rpm. Tissues were immersed sequentially in 20%, 40%, 60%, 80%, and 100% 2-propanol for one hour each, followed by an overnight incubation in 100% 2-propanol. The delipidation process began by transferring tissues to a 2:1 (v/v) mixture of DCM and 2-propanol for an overnight incubation, the duration of which was adjusted based on the tissue's lipid content. This was followed by two 15-minute washes in 100% DCM. For final clearing and RI matching, tissues were transferred to ECi and incubated until optical transparency was achieved (typically overnight) with gentle rolling at 5 rpm. From our experience gentle rolling reduces intratissue bubble formation.

Light-sheet Fluorescence Microscopy

Two light sheet fluorescence microscopy (LSFM) systems were used in the current study, UltraMicroscope Blaze (Miltenyi Biotec) and Aurora (M Squared Lasers). The UltraMicroscope Blaze system, utilizing a Gaussian beam-based static planar light sheet, was equipped with a 4.2 MP sCMOS camera (PCO) with a resolution of 2048×2048 pixels and multi-immersion planar objectives with dipping caps (with correction for imaging in RI of 1.56. For all samples, double-sided illumination and dynamic focusing was employed. The detection objective used is specified in the figure legend of each image.

The Aurora MSquared system, utilizing an Airy beam-based digitally scanned light sheet, was equipped with Hamamatsu Orca Flash4 4.2 MP sCMOS camera, with a

resolution of 2048×2048 pixels and two Navitar Special Optics multi-immersion objectives for imaging in RI 1.33-1.56 (one for illumination and one for detection).

All samples were imaged in ECi regardless of LSFM system used. For mounting the samples in the UltraMicroscope Blaze, silicone-based glue was used to fix the samples on top of the provided microscope sample holder and for the Aurora system a magnetic silicone clamp was used to hold the samples in place in the imaging chamber.

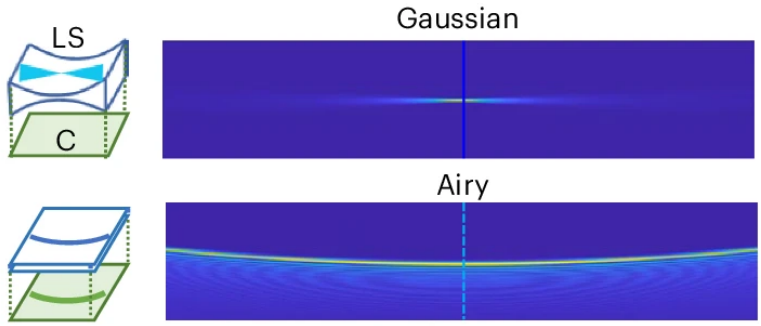

Figure 19. Schematic of Gaussian and Airy light sheet. Figure reproduced from (Qi et al. 2025) with permission.

Three-dimensional (3D) volume rendering

Three-dimensional (3D) volume rendering was performed on light-sheet fluorescence microscopy (LSFM) image datasets using Arivis Vision4D (Zeiss) and Imaris (Oxford Instruments) software platforms. Raw image stacks acquired from LSFM were imported into the respective software platforms in their original format without prior modification. Following import, individual channels were assigned pseudocolors using the built-in LUT of each software package. Display ranges were manually adjusted for each channel to optimize signal visualization and ensure that the majority of the fluorescence signal was represented.

Deconvolution

Deconvolution is a computational method used to recover image that were altered during acquisition. Although it was first developed for astronomical imaging, it was introduced into microscopy in the 1980s and has since become an important image-processing technique for biological imaging. In microscopy, image quality is affected by optical blurring caused by diffraction during image formation, as well as by noise. Deconvolution seeks to computationally improve, or to say more precisely, restore spatial resolution and reveal finer image details. For images

acquired using the Aurora microscope system, image stacks were subjected to deconvolution prior to 3D reconstruction. Deconvolution was performed using the manufacturer-recommended algorithm and factory calibrated point spread function (PSF), depending on acquisition settings. Iterative deconvolution (Richardson–Lucy algorithm) was applied to improve axial resolution, enhance signal-to-noise ratio and reduce optical blurring inherent to light-sheet imaging. The number of iterations and regularization parameters were kept constant across samples within each experimental group.

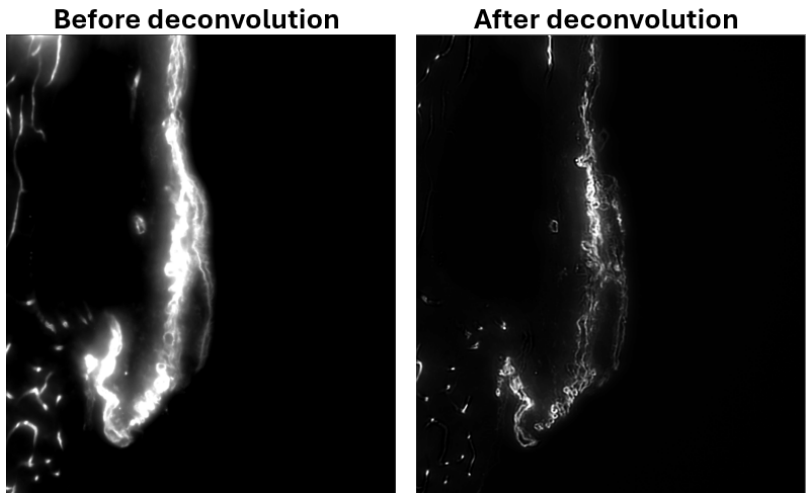

Figure 20. Representative images of the same single plain LSFM image of mouse brain vasculature labelled with lectin fluorescence dyes before and after deconvolution.

PCLS generation for Assessment of Archival Formalin Fixed and Paraffin Embedded Samples

300 μM thick PCLS were prepared using a vibratome (Campden Instruments, 7000smz-2). Lungs were filled with 1.5% low melting agarose (Sigma 9414) and let to solidify at +4°C for 1 hour prior to vibratome sectioning. PCLS were then punched using a 4mm biopsy punch and fixed using NBF for 60 minutes followed by tissue processing as we have previously described but with modifications optimized for PCLS with shortening dehydration steps to 20 min each. Samples were then embedded in paraffin and stored for at least 7 days. In order to remove paraffin prior to performing tissue clearing, FFPE PCLS blocks were incubated at ~65°C in an oven (Binder ED56) for 1 h to ensure complete paraffin removal. Following bulk paraffin removal, 4 mm PCLS punches were transferred to xylene

(Fisher scientific) or Histo-Clear (National diagnostics, USA) and rotated at 25 rpm at room temperature for 2 h. The solution was refreshed every hour by transferring the PCLS into fresh xylene or Histo-Clear II. Following paraffin removal from PCLS, samples were then gradually rehydrated to 100% PBS. The samples were subsequently prepared for whole mount immunofluorescence (IF) staining alongside fresh control PCLS samples (non–tissue-processed and non–paraffin-embedded). Prior to staining, samples were transferred into 12-well plates (Sarstedt). PCLS samples were first permeabilized using 0.1% Triton X-100 (Sigma-Aldrich) at room temperature for 1 hour with agitation at 25 rpm, followed by two washes with 1% BSA (Saveen Werner AB) in PBS. Samples were then blocked for 2 hours in 5% BSA. After blocking, the samples were incubated with the primary antibody (α-tubulin antibody) (Paper III, Supplemental Table 3) diluted in 1% BSA solution for 48 hours at +4°C with gentle agitation (10 rpm) while protected from direct light. After primary antibody incubation, the PCLS samples were washed three times with 1% BSA and then incubated with the secondary antibody, Alexa Fluor 647 goat anti-rabbit, overnight at +4°C with agitation at 10 rpm.

The following day, samples were washed again 3 times with 1% BSA and embedded in 2% low-melting agarose (Sigma, A9414) for 1 hour at +4°C until the agarose solidified. Embedded samples were then transferred into 50 mL tubes and cleared using the PROTEUS clearing protocol described above, while protecting the samples from light. Briefly, samples were gradually dehydrated in 2-propanol, followed by delipidation with DCM under constant rolling at 50 rpm. ECi was

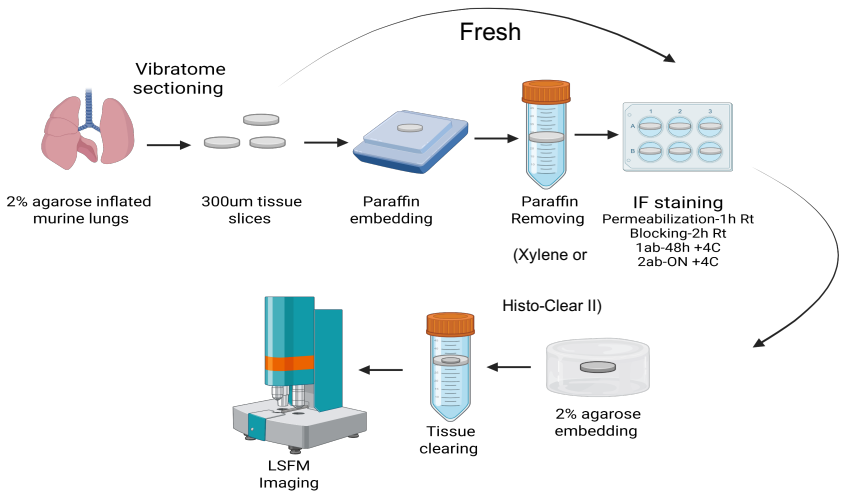

Figure 21. Schematic of PCLS paraffin removal and following fluorescence staining and tissue clearing. Created in BioRender.com by NG

subsequently used as the RI matching solution with slow rolling at 5 rpm. Cleared tissue was imaged using Ultramicroscope Blaze. Laser power was determined by ensuring there was no fluorescence signal detected in cleared PCLS which were incubated with secondary antibody but without primary antibodies.

Reverse optical clearing

Two mouse lungs were used after CO2 chamber euthanasia. One lung was used for optical and reverse clearing and the other as a control for comparison. All lungs were inflated with 1% low melting agarose via the trachea to prevent structural collapse. Lungs were fixed in 10% NBF for 15 min using gravitational fixation through the trachea and submerged for 24 hours. Samples were cleared using iDISCO (195) and imaged in ECi. Next, the lung was sectioned in 6 pieces using a scalpel and transferred to individual 5 mL polypropylene tubes containing an ECi soluble solvent to facilitate its removal from the tissue. These solvents were ethanol, methanol, 2-propanol, acetone, ethyl acetate and DCM. The tubes were then placed inside 50 mL Falcon tubes and incubated on a roller at 50 rpm for 3 hours, with the solvent refreshed every hour.

Agarose/gelatin tissue phantoms for reverse optical clearing and FTIR measurement

Tissue phantoms were generated using 3% low melting agarose (Sigma-Aldrich, A9414) gel containing 5 mg/mL gelatin type A was prepared in 1× PBS, poured into Petri dishes, and incubated at +4°C for 1 h until solidification. After solidification, 8 mm diameter discs were generated using a biopsy punch. The tissue phantoms were immediately transferred to 10% neutral buffered formalin (NBF) and fixed for 24h at +4°C under rolling agitation (50 rpm). After fixation, the tissue phantoms were washed and stored in PBS. For dehydration, individual tissue phantoms were placed in 50 mL tubes containing 20 mL solution and gradually dehydrated in 2-propanol (20%, 40%, 60%, 80%, and 100%), with 1h incubation at each step, followed by overnight incubation in 100% 2-propanol. After overnight incubation, 3 samples were retained in 2-propanol as control samples, while the remaining samples were subjected to PROTEUS forward tissue clearing procedure using DCM/2-propanol (2:1) incubation for 24h, followed by two 15min washes in 100% DCM. All steps were performed with rolling agitation at 50 rpm. Following DCM treatment, the tissue phantoms were transferred to ECi and incubated under rolling agitation (5 rpm) for 24h until complete transparency was achieved. After this incubation, 3 samples were retained in ECi as ECi control samples. Thereafter, cleared transparent tissue phantoms were then subjected to reverse optical clearing

using 100% 2-propanol. Samples were individually transferred into 50 mL tubes and incubated in 2-propanol for 1, 2, or 3 h, with the 2-propanol replaced after each hour (n = 3 for each timepoint). At each time point (1 h, 2 h, and 3 h), FTIR spectra were collected in transmission mode using a diamond ATR accessory on a Cary 630 FTIR spectrometer with KBr optics (Agilent). Spectra were acquired over a wavenumber range of 4000–650 cm^{-1} at a spectral resolution of 2 cm^{-1}, with 8 scans collected as background and 8 scans per sample, and the spectra were averaged for analysis. Control samples maintained in 2-propanol and Eci served as controls. The ATR crystal was thoroughly cleaned with three sequential washes of 2-propanol between each measurement and new background was collected prior to each sample.

FTIR spectral datasets were imported into the Quasar software. For each experimental group, n = 3 spectra were included in the analysis. Analysis was restricted to the fingerprint region and spectral data matrix (wavenumber vs. absorbance) was then subjected to PCA using the built-in Quasar multivariate analysis module. The first two principal components (PC1 and PC2), which explained the majority of the variance, were used to generate score plots to visualize clustering and separation between experimental groups.

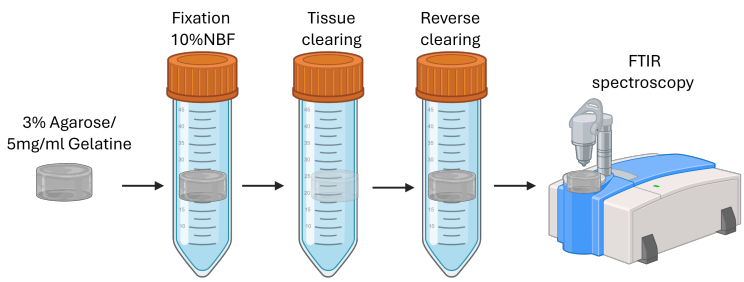

Figure 22. Schematic of reverse clearing and FTIR measurements of agarose/gelatine tissue phantoms. Created in BioRender.com by NG

MERFISH

Once the internal quality control was performed using RNAscope to confirm transcript presence, ROC and control paraffin-embedded embryos in separate blocks were sectioned into 5µm sections in an RNase free environment. Blocks were rehydrated in UltraPureTM Distilled water (Invitrogen, 10977015) at +4°C. A new blade (Fisher Scientific, 360992334) and UltraPure^{TM} Distilled water were used to cut and extend the samples on a +45°C bath. The MERSCOPE Large Slides (Vizgen, 10500131), which have a dimension of approximately 3cm^2 of imageable area, were taken out of -20°C 15 min before placing the freshly cut sections within the labeled imaging window. The two embryos were laid in a distinguishable

manner, to enable subsequent annotation of each of the conditions. Samples were imaged using the MERSCOPETM Ultra (Vizgen) and a ~900 predesigned embryology gene panel (Paper III, Supplemental Table 4). MERFISH single-cell spatial transcriptomics data was loaded from an .h5ad object and partitioned into control and ROC groups based on the spatial coordinate centre 'y'. Cells with a low transcript count were filtered out following standard quality control criteria. Gene expression values were standardized, and dimensionality reduction was performed using PCA. A k-nearest neighbours' graph was constructed, and cell clusters were identified using the Leiden algorithm (resolution=1.0, chosen following manual expert assessment). Cell types were identified for each cluster following manual, expert assessment of genes which were differentially expressed and present in the majority of cells within each cluster. UMAPs were used for the visualization of the cellular manifold. The number of transcripts per cell was extracted separately for each cluster for control and ROC embryos. Plots were generated independently for each embryo to enable direct comparison of transcriptional activity across clusters.

Statistical analysis

Paper I

Differences in β-sheet signal intensity between living and fixed tissues were assessed using one-way ANOVA followed by Tukey's post hoc multiple-comparison test. LDH release measurements were analyzed using one-way ANOVA with Šidák's correction for multiple comparisons.

Paper II

Differences in NucView 488 and RedDot2 staining in PCLS were quantified using one-way ANOVA with Šidák's correction for multiple comparisons.

Paper III

We used Mann–Whitney U test or one-way ANOVA with Brown-Farsythe and Welch multiple comparisons test, as appropriate and based on the underlying distribution of the data and the number of comparisons performed as indicated in the corresponding figure legend. All analyses were performed using GraphPad Prism v11.

Use of AI in this thesis

ChatGPT and Microsoft Copilot PRO were used as generative artificial intelligence (AI) tools to support English language editing and grammar correction during the writing of this thesis. Google Gemini was used under the supervision to create the schematic illustration shown in Figure 50A. The author retains full responsibility for the content, interpretation and accuracy of the work presented in this thesis.

Key Results and Discussion

Spatiotemporal alterations in the chemical composition and structural organization of biomolecules are fundamental determinants to distinguish normal from pathological processes in tissue. However, every pathological process begins with submicron-level alterations before any visible morphological or clinical manifestations can be detected, e.g. by histological of immunohistochemical staining. Therefore, studying very early transformation phases and processes is vital to understand disease pathophysiology, for developing targeted therapy as well as early diagnosis, which may ultimately improve treatment outcomes.

Therefore, alternative techniques such as infrared imaging have attracted increasing attention. Specifically, infrared microspectroscopy (μIR) has been increasingly used in biomedicine and clinical diagnostics. As discussed in the introduction, infrared microspectroscopy is a label-free, non-destructive and highly sensitive technique that simultaneously provides information about diverse biomolecules (e.g. Proteins, DNA, RNA as well as their structural organization. However, μIR has significant drawbacks when applied to biological tissues, since water strongly absorbs infrared light and masks signals from protein vibrations. In addition, light scattering prevents the use of thick samples. Therefore, tissue must be thinly sliced prior to analysis. Consequently, biological tissues must typically be chemically fixed and dehydrated before being sectioned. Thus, studying fresh tissue biopsies using conventional IR alone is not feasible.

However, the recent development of O-PTIR has overcome several limitations of conventional μIR by employing two simultaneous lasers. O-PTIR uses a visible probe beam (532 nm) to detect photothermal responses induced by infrared absorption. As mentioned above O-PTIR was used on relatively transparent biological samples, such as 2D cell cultures and C. Elegans; these studies did not address the potential impact of tissue opacity on spectral acquisition. In addition, because these experiments were limited to endpoint measurements, the effects of O-PTIR imaging on subsequent tissue viability and integrity was not assessed. Accordingly, our primary questions for Paper I were:

1. Can we obtain interpretable, high-quality spectra from fully hydrated, unprocessed tissue biopsies?
2. Does the thermal expansion that occurs during O-PTIR imaging damage the tissue?

O-PTIR can be used in hydrated tissue biopsies and the spectra obtained differs between tissues

To investigate the use of O-PTIR imaging on fully hydrated, unprocessed samples, we extracted different mouse internal organs (lung, heart, liver, kidney, salivary glands) and skin (the entire mouse tail (**Figure 23A**). First, we had to optimize the acquisition settings. In **Paper I**, we observed that both IR laser power and acquisition speed affected spectral quality in hydrated samples. Moreover, IR laser energy higher than 22% led to spectral artifacts, such as alterations in the amide II-to-amide I ratio. However, we showed that at 22% IR laser intensity, together with a high scan rate (1000 cm^{-1}/s), it was possible to obtain spectra with a low signal-to-noise ratio from all hydrated tissues mentioned above.

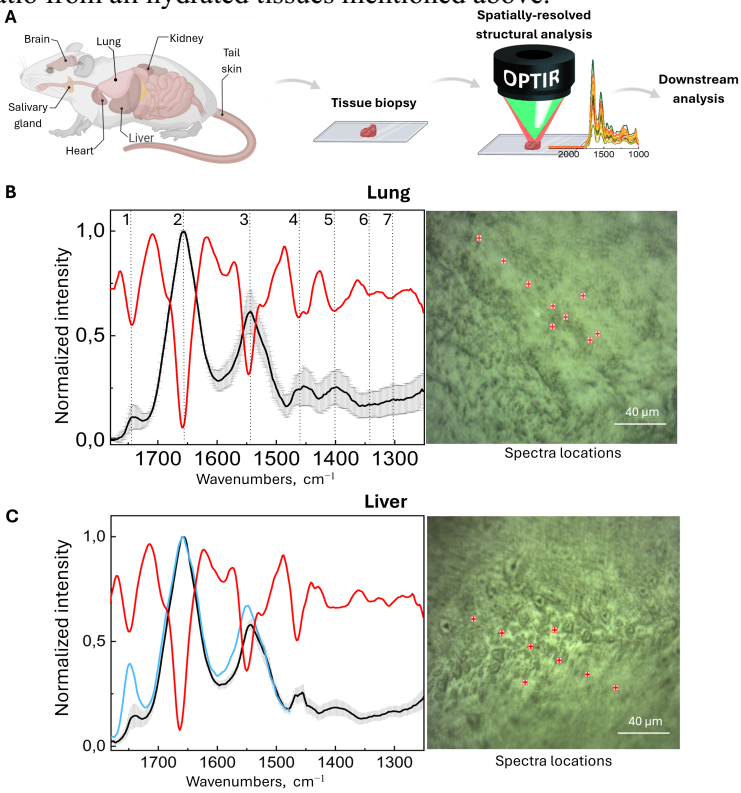

Figure 23. A) Experimental overview (created with BioRender.com). B) and C Livet tissue.Normalized and averaged O-PTIR spectra (black line) and second-derivative (red line) with representative bright-field images of the samples. The gray error bars represent s.d.; N = 3–10 areas from 3–4 tissue biopsies per organ. Red crosses indicate representative spectrum acquisition points, randomly selected for analysis. Peaks identified with second derivative spectroscopy are listed in Table 1. The blue-colored spectrum trace was acquired at the location indicated and revealed a signal increase at 1740 cm–1, which corresponds to elevated ester levels. Figure reproduced from (Gvazava et al. 2023) with permission.

Furthermore, we used second-derivative analysis to identify the expected major peaks corresponding to amide I (1656 cm^{-1}), amide II (1546 cm^{-1}), nucleic acids (1396 cm^{-1}), collagen (1340 cm^{-1}), and amide III (1306 cm^{-1}) in all organs (**Figure 23B**,**C**). Moreover, we could also detect lipids, including ester groups (1740 cm^{-1}) and the cholesterol esters (1464 cm^{-1})(229, 230). Detection of lipids is particularly challenging in biological samples using other IR-based imaging methods because, as mentioned above, samples must typically be dehydrated with alcohols and xylenes (or other nonpolar solvents to enable paraffin embedding), which removes the majority of lipids. However, in diseases such as non-alcoholic fatty liver steatosis, altered lipid metabolism plays a key role in pathogenesis (230). In addition, we observed organ-specific and sub-tissue-specific spectra. For example, in liver biopsies, we could distinguish regions with elevated intensity at 1740 cm^{-1} in certain areas. We also noted a significant increase in the peak area centered at 1452–1396 cm^{-1}, previously described as arising from methylene groups of proteins and lipids and shown to be important for salivary gland characterization (231) (**Figure 23C**). We also recorded O-PTIR spectra directly from mouse tail skin, allowing detection of spectral bands corresponding to amide II (1500–1590 cm^{-1}), amide I (1600–1700 cm^{-1}), and a prominent peak at 1515 cm^{-1}.

Therefore, we showed that O-PTIR can be used to acquire highly specific spectra for label-free assessment of fresh, non-processed, and hydrated biopsies immediately after sampling.

O-PTIR can distinguish between normal and diseased tissue

All tissue biopsies described above were obtained from wild-type (WT) animals, therefore, these tissues did not exhibit significant pathological alterations. However, it was also important to determine whether O-PTIR could distinguish between healthy and diseased regions within the same tissue sample. Once the O-PTIR measurement parameters for living tissue had been established, we used brain slices from the APP/PS1 Alzheimer's disease mouse model. In this model, mouse/human amyloid precursor protein (APP) and mutant human presenilin 1 (PS1) are co-expressed, leading to amyloid-β aggregation in the brain parenchyma(232). We used freshly extracted brains from 12-month-old APP/PS1 mice and prepared 275 μm-thick brain slices. To preserve tissue viability, the slices were maintained in oxygenated buffer at room temperature (**Figure 24A**). Cortical tissue was examined, as this region consistently contains β-sheet-rich amyloid plaques at this age. Plaques were located using rapid hyperspectral array scanning over an extended area. Amyloid plaques were identified from the surrounding tissue by a spectral shoulder between 1640 and 1620 cm^{-1} (**Figure 24B,C**), previously assigned to β-sheet structure (233).

Following label-free O-PTIR spectroscopy, these slices were further processed to visualize amyloids using the highly specific probe AmytrackerR (**Figure24D**). Taken together, these results provide evidence that O-PTIR imaging can successfully detect amyloid plaques in freshly prepared, hydrated brain tissue slices. Furthermore, these results show that O-PTIR can be used to distinguish pathological from normal tissue, highlighting its clinical potential, for example, for rapid surgical diagnosis during tissue resection. Interestingly, we also observed differences between fixed and fresh samples, which raises the important question of how fixation alters tissue structure and composition.

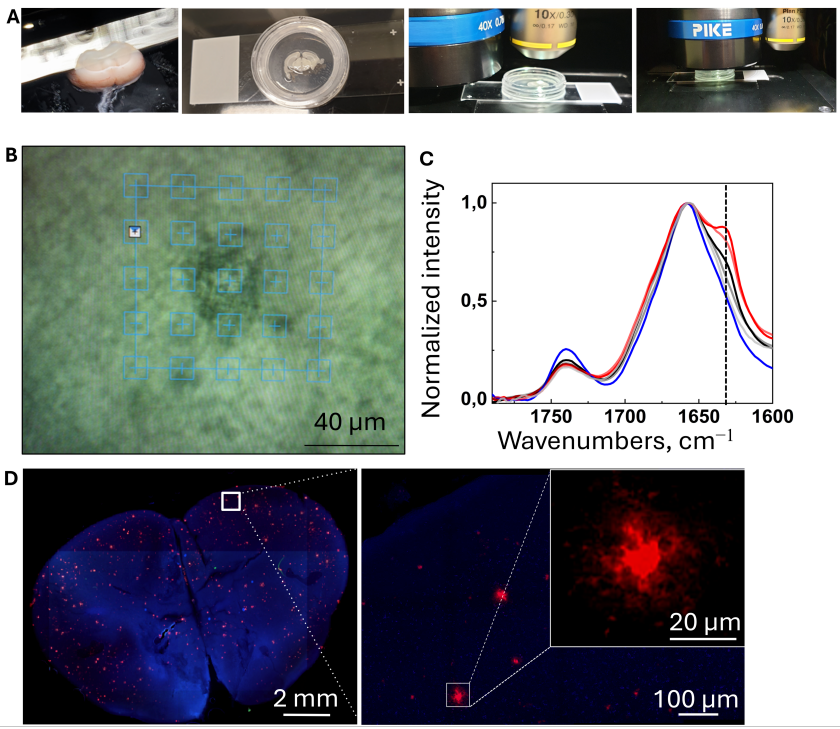

Figure 24. A) Acute brain slices section with vibratome into 275 µm thick sections, followed by incubation in a custom imaging chamber containing oxygenated artificial cerebrospinal fluid (aCSF, "brain media") at room temperature. The tissue was imaged in this custom-built chamber using O-PTIR under low (15×) and high (60×) magnification objectives. B) Brightfield images show representative brain plaque regions, with boxed areas indicating locations selected for spectral acquisition. C)Normalized O-PTIR spectra were collected from the positions indicated in panel .The arrow highlights the ~1630 cm^{-1} shoulder, characteristic of amyloid fibrils. Spectra shown in red correspond to positions marked by red squares. D)Post–O-PTIR imaging, the same tissue section was stained with Amytracker™520R to visualize amyloid plaques (red signal). Tissue autofluorescence was acquired using a DAPI filter on a Cytation 5 multimode imager (4× objective). E) Higher magnification imaging of the same plaques, including 20× imaging on the Cytation5 and F) confocal microscopy image of the same amyloid plaque. Figure reproduced from (Gvazava et al. 2023) with permission.

Interestingly, we observed fixation-induced alterations in protein secondary structure when comparing fresh and 4% PFA-fixed tissue. In particular, an increase in β-sheet content was observed following fixation, accompanied by a shift in the amide I band from 1630 to 1634 cm^{-1}, indicative of changes in protein conformational organization (**Figure 25A**). Further, we quantiatively confirmed a significant increase in β-sheet signal intensity in fixed tissue relative to living samples (**Figure 25B**). This suggest that amyloid structure may undergo structural alteration during the fixation, therefore highlighting the additional need of evaluating amyloid structures in their native state for example during different anti-amyloid therapies.

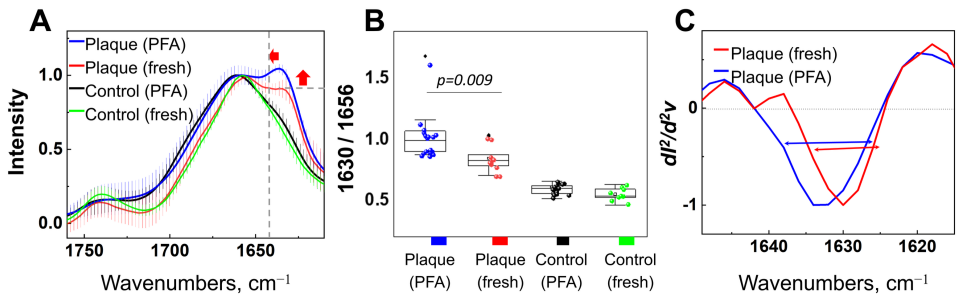

Figure 25. A) Normalized and averaged O-PTIR spectra of fresh and tissue fixed in 4% PFA. Arrows indicate an increase in the intensity of β-sheet (up) and changes in structural content; band position shift from 1630 cm–1 to 1634 cm–1. Error bars are s.d. B) β-sheet signal intensity in living and fixed tissue. Tukey's post-hoc test; N = 8–10 spots. Data are the mean ± s.d. C) Second derivatives of IR absorbance spectra. Arrows indicate changes in bandwidth. Figure reproduced from (Gvazava et al. 2023) with permission.

Local tissue level damage in biopsy punches following O-PTIR imaging

Next, we investigated whether thermal expansion caused by IR laser during O-PTIR imaging induces tissue-level damage. Cell viability in 1.5 mm tissue biopsies from O-PTIR irradiated and non-irraqdiated controls were assesed using the colometric Water-soluble tetrazolium salt-1 (WST-1) assay (**Figure 26A,B**). While we observed metabolic activity after OPTIR imaging, biopsy size and tissue heterogeity differences may contributed to the differences observed in the groups. Moreover, WST-1 asseses metabolic activity in all tissue, therefore it is chellenging to distinguish between OPTIR irradiation and other factors contributing to cell viability.

Therefore, in an attempt to evaluate potential structural alterations, the same tissues were subsequently fixed in 10% neural buffered formalin (NBF), tissue processed

and paraffin-embedded prior to subsequent sectioning and Hematoxylin and eosin (H&E) staining (**Figure 26A,B**). Histological examination did not reveal any noticeable morphological differences between O-PTIR imaged and control tissue. However, O-PTIR imaging was perfomed on an approximatly 0.5µm^2 area, which is challenging to follow without specific markers over the time especially after tissue processing. Tissue processing dehydrates tissue resulting in shrinkage, while parrafin embedded is challenging to maintain exact orientations prior to generating thin sections; as a consequence, precise correlation between the original O-PTIR imaging site and the corresponding H&E-stained section is challenging.

Nevrertheless, these resuls however demonstrate the ability of downstream analyses (e.g. H&E staining) after OPTIR imaging , which again highlights potential use of this technique in histopathology. The ability to perform label-free chemical imaging prior to standard tissue processing and staining supports the potential use of O-PTIR as a complementary technique in histopathology, where molecular information could be obtained from fresh or minimally processed tissue before subsequent morphological evaluation.

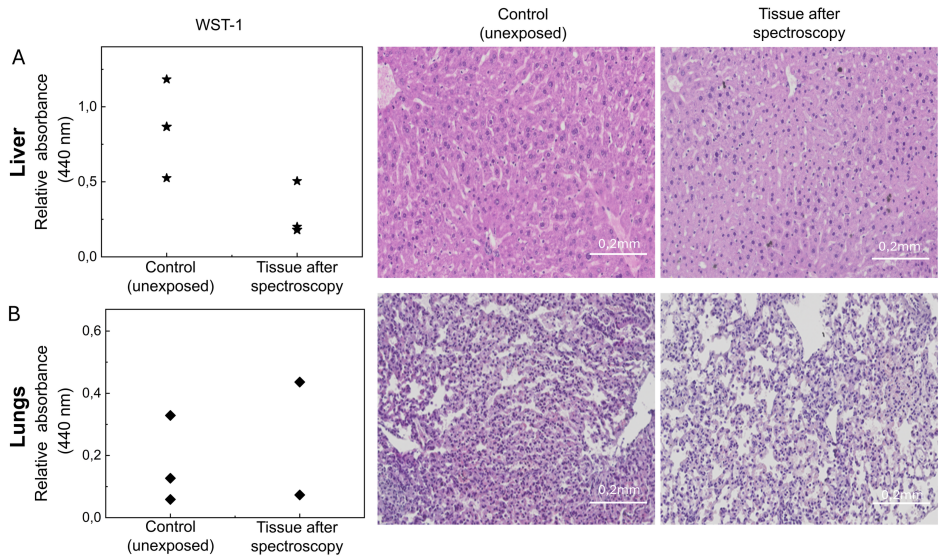

Figure 26. WST-1 assay (water-soluble tetrazolium salt) performed on 1.5 mm liver (A) and lung(B) biopsy punches, comparing unexposed controls and O-PTIR–exposed samples, with representative H&E staining of the same tissues. Figure reproduced from (Gvazava et al. 2023) with permission.

Tracking cellular damage after O-PTIR imaging in acute brain slices

To assess tissue level damage in a more robust manner, we utilized 275 µm thick acute brain slices (**Figure 27A**) because we could image and follow the same anatomical region of the brain. In addition, organotypical slices of different organs is incresingly used in drug testing, tissue remodeling and other applications. We therefore focused on the retrosplenial cortex (RSC), a small dorsomedial cortical region that can be reliably identified across imaging platforms (234). The RSC is also functionally well characterized and contains distinct populations of pyramidal neurons. Using a custom-made sample holder with N-methyl-d-glucamine (NMDG) artificial cerebrospinal fluid (aCSF) media formulation, acute brain slices were imaged in aqueous conditions. Single-frequency O-PTIR maps were acquired in the RSC at 1656 cm^{-1}, corresponding to the strongest O-PTIR signal in brain spectra. Maps covering 250 × 400 µm were collected using identical O-PTIR settings and a 500 nm step size(**Figure 27B**). Following O-PTIR imaging, pyramidal neurons within the irradiated area retained elector-physiologically active and firing properties (**Figure 26 C**), demonstrating that functionally active cells remained present after OPTIR imaging.

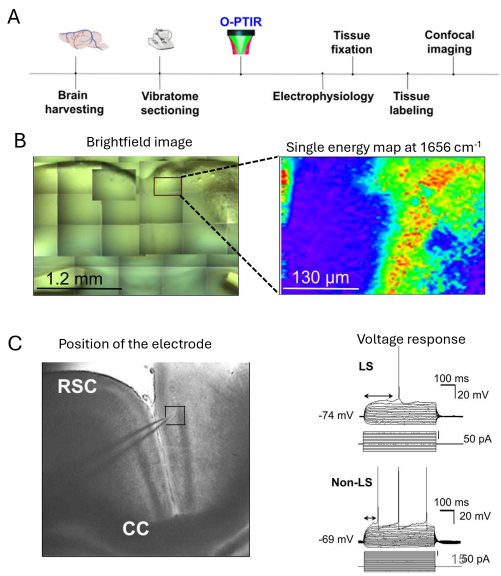

Figure 27. A) Experimental overview B) Bright-field image showing the location of a single energy map acquired at 1656 cm–1 in the retrosplenial cortex (RSC). C) Differential interface contrast (DIC) images showing the position of the electrode during the electrophysiological recording in RSC of acute (living) tissue slices exposed to O-PTIR. Voltage responses to current injection of two different pyramidal neurons recorded in current clamp mode after O-PTIR measurements. Late-spiking (LS) and non-late spiking pyramidal cell (non-LS). Figure reproduced from (Gvazava et al. 2023) with permission.

Further we evaluated potential tissue damage at the molecular and cellular level. OPTIR irradiated acute brain slices were fixed and immuno stained. Neuronal morphology was assessed using microtubule-associated protein 2 (Map2), a dendritic marker used to evaluate dendritic integrity. In parallel, apoptosis-associated changes were examined using AnnexinV, which binds phosphatidylserine residues which is translocated at the plasma membrane during early apoptotic processes (235). No substantial loss of neurons or disruption of Map2 staining was observed in regions exposed to O-PTIR. Similarly, Annexin V staining did not show a noticeable increase in the irradiated areas (**Figure 28**).

However, a drawback of acute brain slices is that it is a short-term model (~hours) and needs to be converted to organotypic tissue culture, with further medium and culturing formulation changes, which induces its own morphological, cellular adaptations and tissue remodeling over time. Furthermore, post-mitotic neurons are considered relatively resistant to apoptosis compared to other more proliferative cell types, as part of evolutionary defence mechanisms (236, 237).

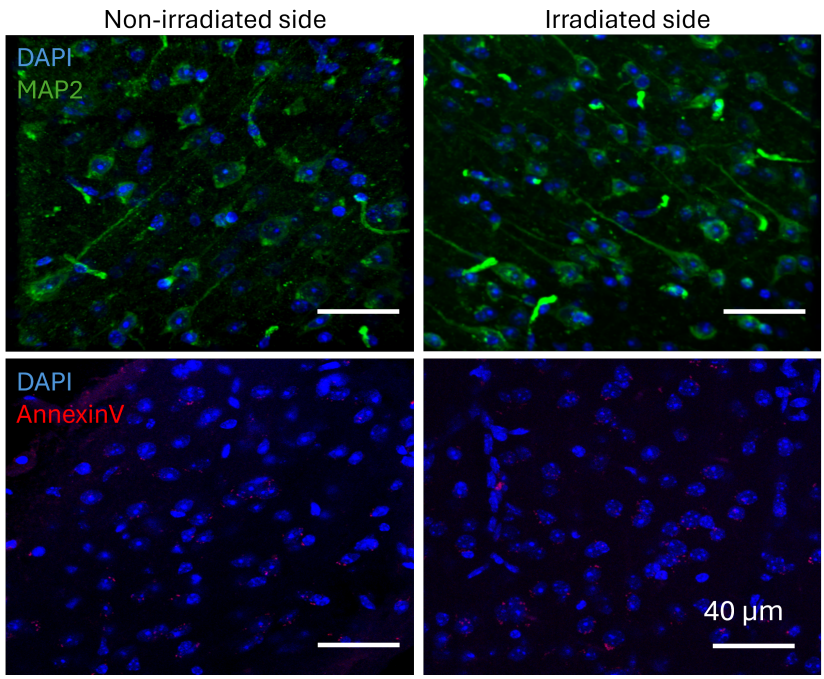

Figure 28. Confocal images showing MAP2-positive neurons retaining their morphology after the spectroscopic measurements compared to the unexposed tissue. High-resolution images of AnnexinV (red dots) in tissue after spectroscopy and unexposed tissue. Figure reproduced from (Gvazava et al. 2023) with permission.

In Vivo O-PTIR Imaging of *Pleurodeles waltl* Embryo

To further investigate the potential of O-PTIR spectroscopy as a non-destructive, *in vivo* imaging modality we chose to use a developing embryo model of the vertebrate *Pleurodeles waltl*. This model is increasingly used in developmental and regenerative biology and characterized by a two-week embryonic phase followed by a ten-week larval stage prior to metamorphosis. We specifically selected stage 34 embryos (approximately 11–13 days post-fertilization) for this study(238). At this developmental stage, major organ systems are formed, but still they are under a developmentally fragile stage. We therefore hypothesized that tissue level alterations caused by O-PTIR may cause developmental abnormalities.

Embryos were placed on the histological glass slide and in the O-PTIR microscopes. We microscopically observed droplet-like structures on the skin surface of the embryos (**Figure 29**). To determine their structural components, OPTIR spectra were measured from those droplets. We observed a strong peak at 1748 cm–1, indicating a high amount of esters (−C═O, −C═OOH), characteristic of lipids (**Figure 30 B**). Further we acquired hyperspectral maps of 1748, 1656, 1640, and 1470 cm–1 and reconstructed chemical maps of the dorsal side of the embryo, showing that both lipids and proteins were identified (**Figure 30C, D**). Demonstrating the ability of label-free *in vivo* O-PTIR imaging of embryos.

Detection of lipid-rich structures are particularly important. Lipids are a well known energy source and it showed critical role in amphibian metamorphosis and survival (239). Therefore, any alteration may compromise their development.

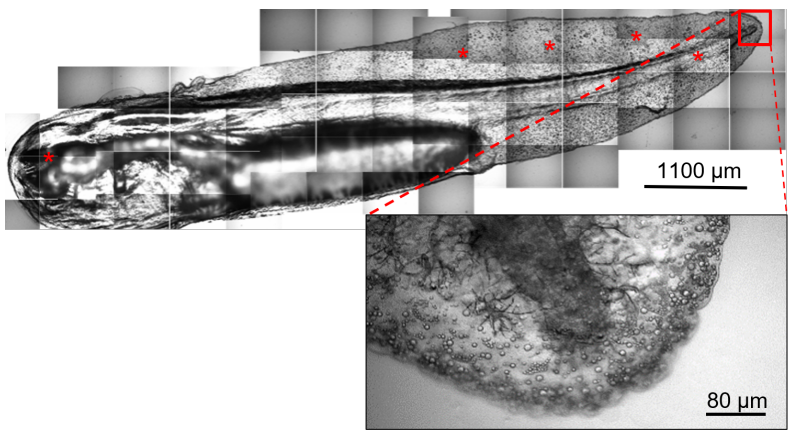

Figure 29. Bright-field mosaic of the *P. waltl* embryo. Asterisks indicate the O-PTIR spectrum acquisition points. Red rectangle indicates the O-PTIR map position and the embryonic tail showing lipid droplets on the skin. Figure reproduced from (Gvazava et al. 2023) with permission.

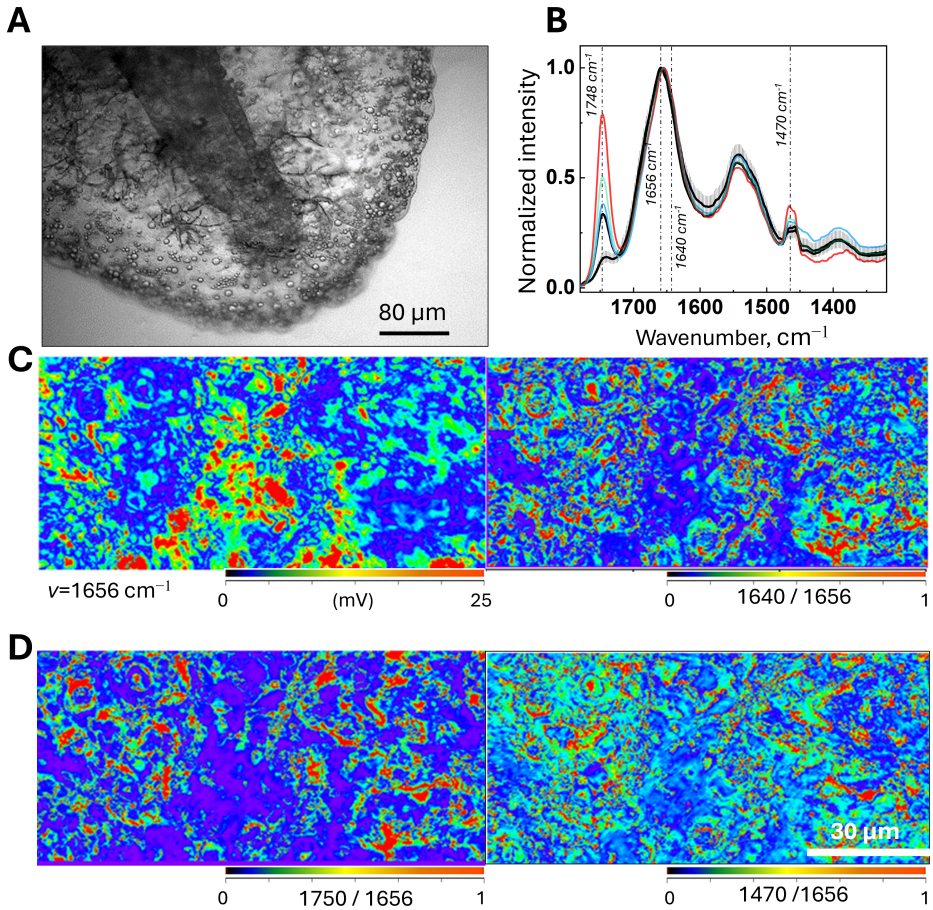

Figure 30. Normalized O-PTIR spectra acquired at different locations are shown in A) Bright-field image B) Black traces, spectra acquired from spots outside lipid droplets; error bars, s.d. for black-trace spectra; N = 6 animals. Colored traces are spectra acquired from the lipid droplets. C) Single-frequency IR maps were acquired at the same spot at two energy levels corresponding to proteins (1656 cm–1 and 1640 cm–1). D Single-frequency IR maps acquired at the same spot at two energy levels corresponding to R-CO-OR groups (1750 cm–1 and 1470 cm–1), showing the distribution of lipids. Figure reproduced from (Gvazava et al. 2023) with permission.

In order to, to investigate whether OPTIR imaging compromised *Pleurodeles waltl* development, embryos were maintained for an additional 14 days after imaging and compared with non-exposed control embryos. Foremost, all embryos survived O-PTIR imaging (n = 6) and developed similarly to controls not exposed to the O-PTIR (n = 6) with no obvious defects in gross morphology or developmental progression. These findings indicate that, under the imaging conditions used here, O-PTIR did not overtly compromise *P. waltl* development (**Figure 31**).

However, *P.walts* are recognized for their cellular plasticity and highly regenerative ability, which raises the possibility that minor localized alterations could be compensated. In addition, embryos continuously grow and undergo morphological remodeling, while the skin is subject to constant renewal. Consequently, it becomes difficult to precisely locate and evaluate the exact region that was previously exposed to O-PTIR.

Further studies using more standardized, spatially traceable and less regenerative models will be required to assess potential local tissue effects with higher precision.

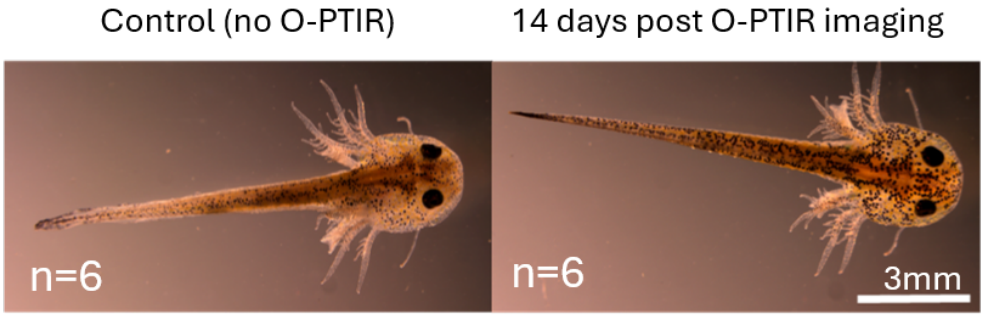

Figure 31. Representative images of *P.waltl* after 14 days of O-PTIR imaging, alongside non-irradiated control samples. Figure reproduced from (Gvazava et al. 2023) with permission.

Cellular damage after vibratome sectioning of PCLS

To further characterize the local damage induced by O-PTIR, we decided to use agarose-inflated lung tissue to generate precision-cut lung slices (PCLS) with a defined thickness of 300 µm (**Figure 32**). The use of agarose-inflated lung tissue offers several important advantages for our experimental aim. First, published protocols already exist for the extended *ex vivo* culture of PCLS, allowing lung tissue to remain viable and functional for several days. This provides a substantially longer observation window compared with acute brain slices. Second, inflated lung tissue retains distinct and recognizable morphological features, e.g. shape of the airways or alveolar regions (**Figure 32**). These visible morphological features make it possible to identify the same spot and follow it over time, thereby overcoming limitations encountered in both acute brain slices and *P. waltl* embryo models.

However, before using PCLS to O-PTIR damage assessment, it was necessary to identify live-imaging compatible stains (or markers) that are sufficiently sensitive and capable of distinguishing different levels of cellular damage. Recent studies have used activated caspase-3 as an early apoptotic marker to monitor cell death during lung development (88). However, caspase-3 activation represents only an early phase of apoptosis, but we aimed to distinguish between different stages and

severities of cellular damage. For this purpose, we selected a dual-staining RedDot2 and NucView 488 staining kit . RedDot2 is a membrane-impermeant far-red nuclear dye that selectively labels cells with compromised plasma membrane integrity. In contrast, NucView 488 is a cell-permeable however in its intact form, the dye is non-fluorescent and unable to bind DNA. NucView 488 consists of a DNA-binding dye coupled to the DEVD peptide sequence. After entering the cell, active caspase-3/7 cleaves the DEVD peptide, releasing the dye, which then translocates to the nucleus and emits bright green fluorescence upon DNA binding. Together, these markers provide complementary information: RedDot2 - loss of membrane integrity, whereas NucView 488- early apoptotic marker.

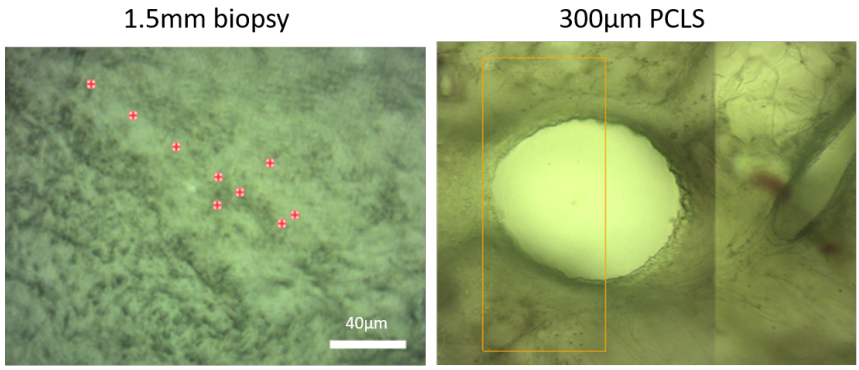

Figure 32. Brightfield images comparing lung tissue biopsies (1.5 mm) and precision-cut lung slices (PCLS) of 300 µm

However, because this staining kit was originally developed for cell-based assays, its applicability to organotypic tissue cultures, such as PCLS, had to be validated. Therefore, we performed staining immediately after vibratome sectioning; PCLS were punched using a 4 mm biopsy punch, stained and subsequently live imaged with a confocal microscope. As described in **Paper II**, the laser settings for the FITC and Cy5 channels were adjusted using subsequently cultured unstained control PCLS, without detectable background signal (same settings were used in **Paper I**).

In the stained PCLS, we first confirmed that the tissue slices could be stained and live-imaged using this kit. We observed that some cells (particularly at the edges of the PCLS) were predominantly positive for RedDot2. Overall, freshly sectioned PCLS showed increased plasma membrane permeability, as assessed by RedDot2 nuclear staining, together with activation of caspase-3/7, detected by NucView 488 (**Figure 33**).

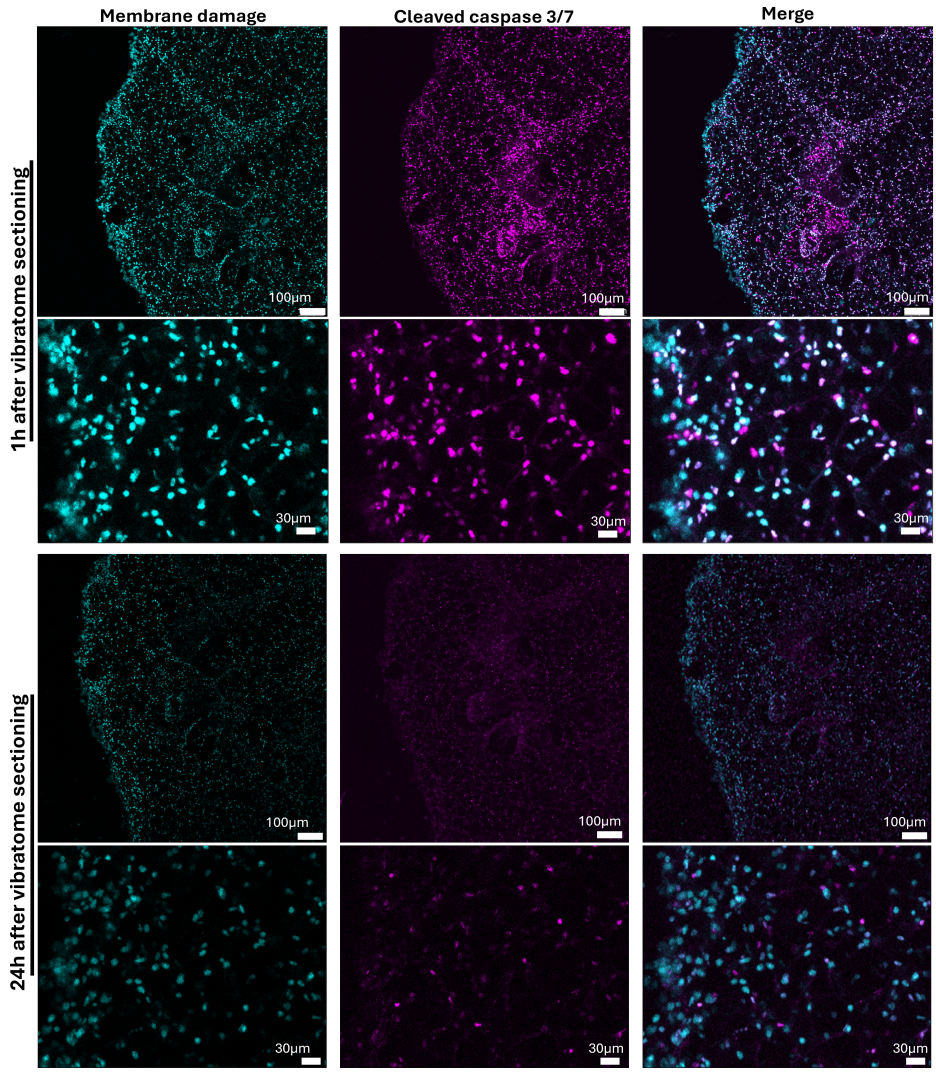

Figure 33. Maximum intensity projection (MIP) of live confocal imaging of PCLS stained immediately after sectioning and after 24 hours in culture. Membrane damage is visualized using RedDot™2 nuclear staining (pseudocolored cyan), while apoptosis is detected by cleaved caspase-3/7 activity using NucView®488 (pseudocolored magenta). Relanalyzed for this thesis

However, when the same PCLS samples were re-imaged after 24 h of incubation, the signal from both markers was reduced (**Figure 34B**). Moreover, the NucView 488 signal was significantly decreased (**Figure 34C**). This observation supports the widely accepted practice in the PCLS field of including a post-sectioning "resting period." Most studies using cultured PCLS describe an overnight or 24 h recovery period, allowing the slices to recover from the mechanical stress induced by tissue sectioning (240). Our findings indicate that slicing itself induces some cellular

damage, including increased membrane permeability. This is an important consideration when designing experiments using PCLS, particularly in studies assessing tissue injury or the efficiency of delivery agents as it shown in Paper I and II, where slicing-induced damage may interfere with the interpretation of experimental outcomes. To further assess this effect, we stained PCLS that had been allowed to rest for 24 h before staining(**Figure 34B**). In these rested samples, both RedDot2 and NucView 488 signals were reduced compared with freshly sectioned slices (**Figure 34C**).

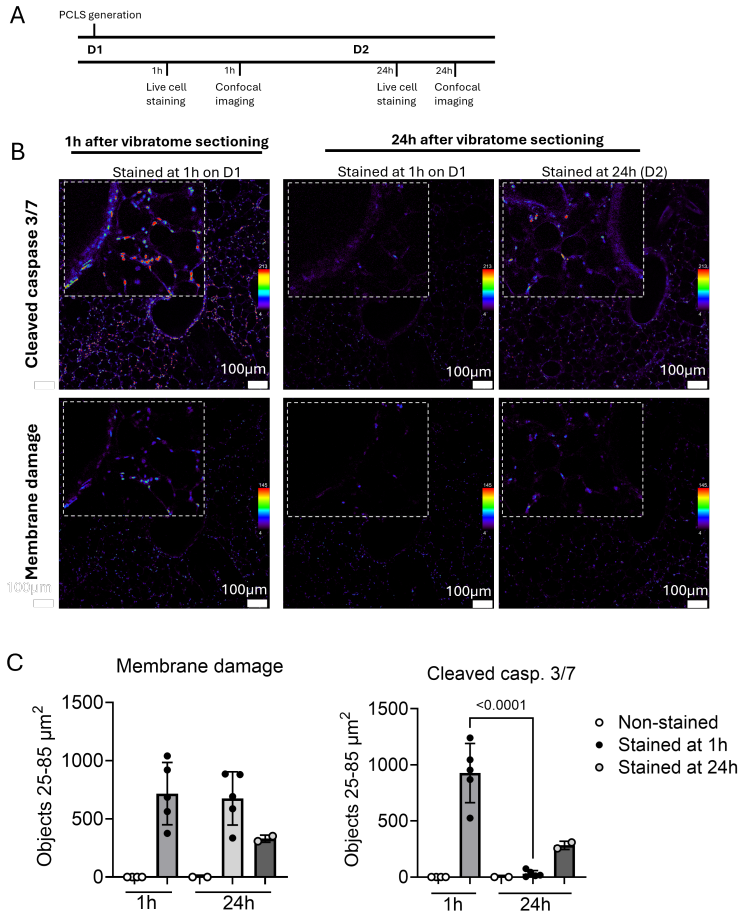

Figure 34. A) Experimental overview and B)Single, representative z-plane acquired with confocal microscopy and stained live immediately or 24 h after vibratome slicing; unstained controls; pseudocolored with a multicolor LUT to represent pixel intensity (n = 2 male mice with 2–5 PCLS per condition). B: quantification of objects corresponding to murine nuclei to assess membrane damage (RedDot2 nuclear stain) and cleaved caspase 3/7 staining (NucView 488 nuclear stain) immediately or 24 h after vibratome sectioning; P value < 0.05 considered significant; one-way ANOVA with Šidák correction for multiple comparisons. Figure reproduced from (Nowakoska et al. 2024) with permission.

We interpret this reduction as evidence of the recovery capacity of PCLS during *ex vivo* culture. Although PCLS are disconnected from the circulation, they remain viable tissue cultures that preserve the native extracellular matrix, lung architecture, and multiple resident cell types. These features may support tissue recovery and partial self-repair following sectioning-induced damage. Therefore, based on these observations, we recommend including a resting period before staining, imaging, or performing downstream experiments with PCLS based on experimental needs.

To verify that the reduction in fluorescence observed in the previous experiments, particularly for NucView 488, was not caused by confocal microscope induced photobleaching or dye instability, we performed additional control experiments using hydrogen peroxide to trigger cellular damage. PCLS were treated with 150 µM hydrogen peroxide immediately after slicing. Following the staining 24 h after slicing (Day 2) without any additional staining at later time points. The slices were imaged immediately after staining and then re-imaged 24 h later, therefore 48 h after slicing and hydrogen peroxide treatment.

We observed that in hydrogen peroxide-treated PCLS, fluorescence was maintained over time (**Figure 35B**). Moreover NucView 488 staining increased, while RedDot2 staining remained (**Figure 35C**). These findings suggest that both dyes were stable under the experimental and imaging conditions used. Therefore, the reduction in fluorescence observed in previous experiments is unlikely to be explained by photobleaching or dye instability, but instead most likely reflects recovery of the PCLS after slicing induced damage.

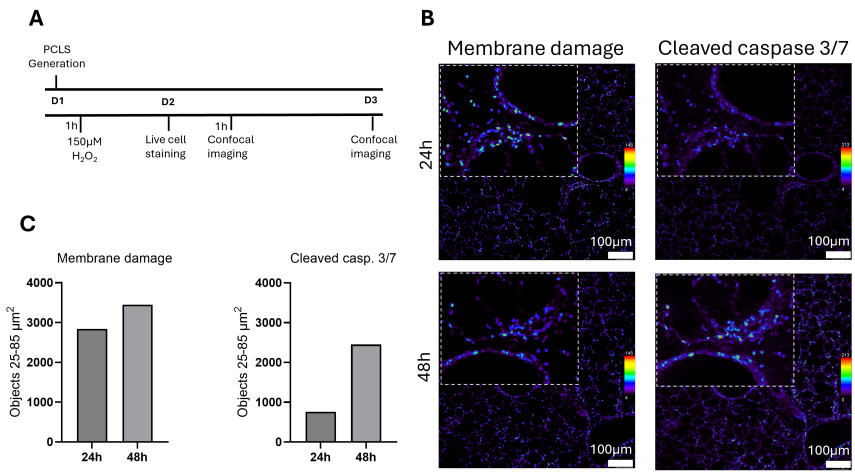

Figure 35. A) Experimental overview; PCLS were treated with 150µM of hydrogen peroxide for 24h followed by live cell staining and confocal imaging at 24h and 48h after slicing. B) Representative single plane images pseudo colored with a multicolor scale to represent pixel intensity. All images were collected with identical laser settings and look up tables (LUTs) as those in Figure 1. C) Quantification of the number of nuclei in a representative 50µm thick volume of PCLS; z-planes every 10 µm were quantified. Figure reproduced from (Nowakoska et al. 2024) with permission.

Furthermore, we extended the analysis of nuclear signal beyond object quantification by measuring several morphological parameters, including- area, circularity and solidity (**Figure 36**). Area reflects the size of each detected particle, in our case the labelled nucleus, and can indicate whether the detected objects fall within the expected size range for cell nuclei. Circularity describes how closely the shape of an object resembles a perfect circle, with values approaching 1- highly circular object and lower - more elongated, irregular or fragmented. Solidity measures how compact or structurally regular an object is by comparing its area to the area of its convex hull. A solidity value close to 1- smooth and compact object, reduced solidity suggests membrane irregularity, nuclear deformation, or other shape abnormalities. Taken together, these complementary analyses help to further interpret our data.

Following this analysis, we observed that the size distribution of the quantified particles remained consistent across individual PCLS and time points. This suggests that the image segmentation approach reliably identified nuclear-sized structures in analyzed images. In addition, the measured particle sizes were in agreement with previously reported nuclear dimensions in murine lung tissue (241).

Despite this stable size distribution, both circularity and solidity size distributions decreased after 24 h of culture in nuclei labelled with either NucView 488 or RedDot2, independent of whether staining was performed immediately after slicing or following the resting period. This indicates that, although the overall nuclear size remained relatively unchanged, nuclear morphology became progressively less regular during culture. Reduced circularity and solidity are consistent with previously described apoptotic nuclear changes, including nuclear condensation, deformation and fragmentation. These observations are also in line with previous histological findings in PCLS, where increasing culture time was associated with progressive alterations in nuclear morphology (59).

Taken together, these findings support the specificity and stability of the staining strategy under the applied culture and imaging conditions. The preserved particle size distribution confirms consistent detection of nuclear structures, while the reductions in circularity and solidity indicate biologically relevant changes in nuclear morphology. Overall, these results suggest that vibratome sectioning induces cellular stress, including increased membrane permeability and activation of apoptotic cell death.

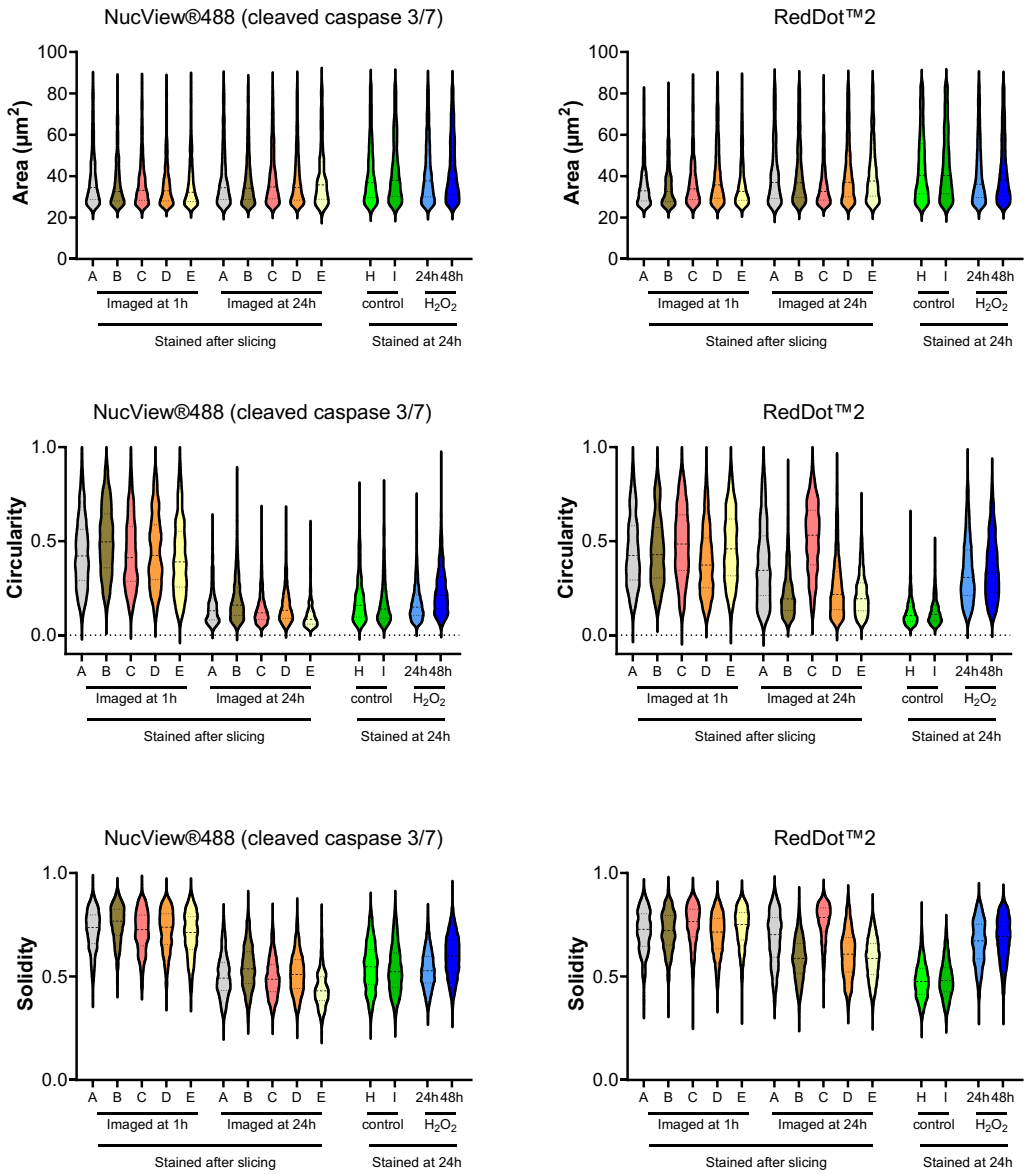

Figure 36. Parameter analysis was performed across PCLS samples and time points for NucView®488 and RedDot™2 staining. The area range was predefined based on previously published stereological analyses of murine lung nuclei and was subsequently validated by post hoc analysis as appropriate for identifying nuclei labeled with both dyes.In addition to size, particle shape descriptors including circularity and solidity were quantified. Figure reproduced from (Nowakowska et al. 2024) with permission.

Live tracking of cellular damage in precision-cut lung slices (PCLS) following O-PTIR imaging

After confirming that the NucView 488 or RedDot2 kit was stable and suitable for detecting different levels of cellular damage over time in organotypic PCLS cultures in Paper II, we next applied this approach to assess potential O-PTIR induced damage In Paper I. Immediately after generating 4 mm PCLS punches, distinct airways were selected in each slice for OPTIR imaging, to allow us to irradiate and subsequently follow the same spot over time (**Figure 37A**). These airway regions were then exposed to O-PTIR imaging using either 22% or 48% IR power. A single-wavenumber hyperspectral map was acquired at 1656 cm^{-1}, corresponding to the amide I region (**Figure 37B**).

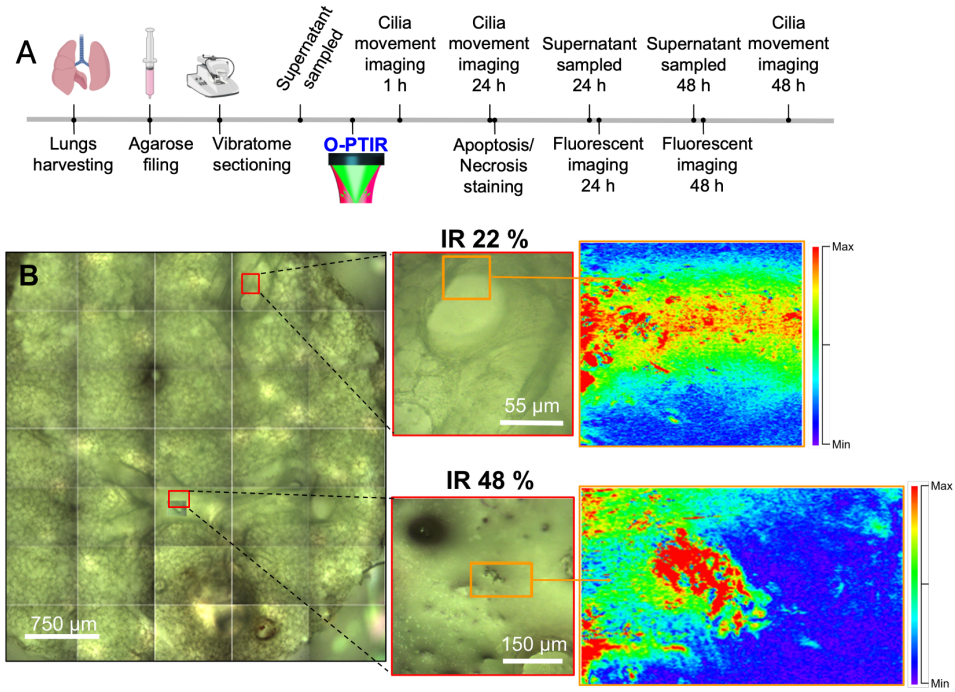

Figure 37. A) Experimental overview (created with BioRender.com) B) Bright-field overview of 4 mm PCLS punch with insets indicating airways subjected to hyperspectral imaging at 1656 cm–1 with different laser intensities. Figure reproduced from (Gvazava et al. 2023) with permission.

Following O-PTIR imaging, the PCLS were allowed to rest for 24 h before staining with the NucView 488 or RedDot2 kit. The same samples were then live-imaged by confocal microscopy at 24 h and 48 h after irradiation (**Figure 38A**).We did not observe differences in membrane damage between control and O-PTIR-irradiated groups, as assessed by RedDot2 nuclear staining. However, a subjective increase in caspase-3/7 activity, detected by NucView 488, was observed in the irradiated groups (**Figure 38B**). This may indicate that O-PTIR exposure induced a mild or localized apoptotic response without progressing to extensive loss of membrane integrity within the analysed time window. However, it is important to consider that live confocal fluorescence imaging was involved. Although confocal microscopy is widely used for live-cell and live-tissue imaging, it can introduce additional phototoxic stress, particularly compared with widefield microscopy. This is especially relevant in the present experiment, as the assessment relied on excitation of fluorescent dyes which repeated excitation of these probes from the same airway region may generate phototoxic effects. Another important consideration is that the same airway regions were imaged repeatedly over time. Especially for airway regions in PCLS, where the ciliated epithelium forms a relatively thin, monolayer-like structure lining the airway lumen. In such regions, cells are directly exposed to the imaging beam and may be more sensitive to local changes. Therefore, even mild imaging-induced stress could be more readily detected in airway epithelial cells than in thicker tissue regions.

To further evaluate tissue viability after O-PTIR imaging, we used additional complementary methods. First, ciliary beating was monitored in irradiated airways using phase-contrast widefield microscopy. Ciliated epithelial cells line the conducting airways and play an essential role in mucociliary clearance by generating highly coordinated beating movements. As shown in the supplementary video in Paper I, ciliary beating was still detectable in irradiated airways even 48 h after O-PTIR exposure, indicating that the airway epithelium remained functionally viable after imaging. However, quantitative assessment was not possible of ciliary beating with available equipment.

In addition, lactate dehydrogenase release was measured in the culture supernatant as a biochemical indicator of cellular damage. We observed a significant increase in LDH release at 48 h in the irradiated groups compared with the same samples after sectioning at 0 h. However, it is important to note that LDH release is a time-dependent process and this likely explains the relatively low LDH levels observed at 0 h (**Figure 38C**). Similar to WST-1, LDH measurements provide a bulk, tissue-level measurements rather than single-cell or spatially resolved information. Therefore, increased LDH levels cannot precisely identify which specific cell types or tissue regions were affected, nor can they distinguish whether the damage originated directly from O-PTIR irradiation, repeated live imaging, or a combination of these factors.

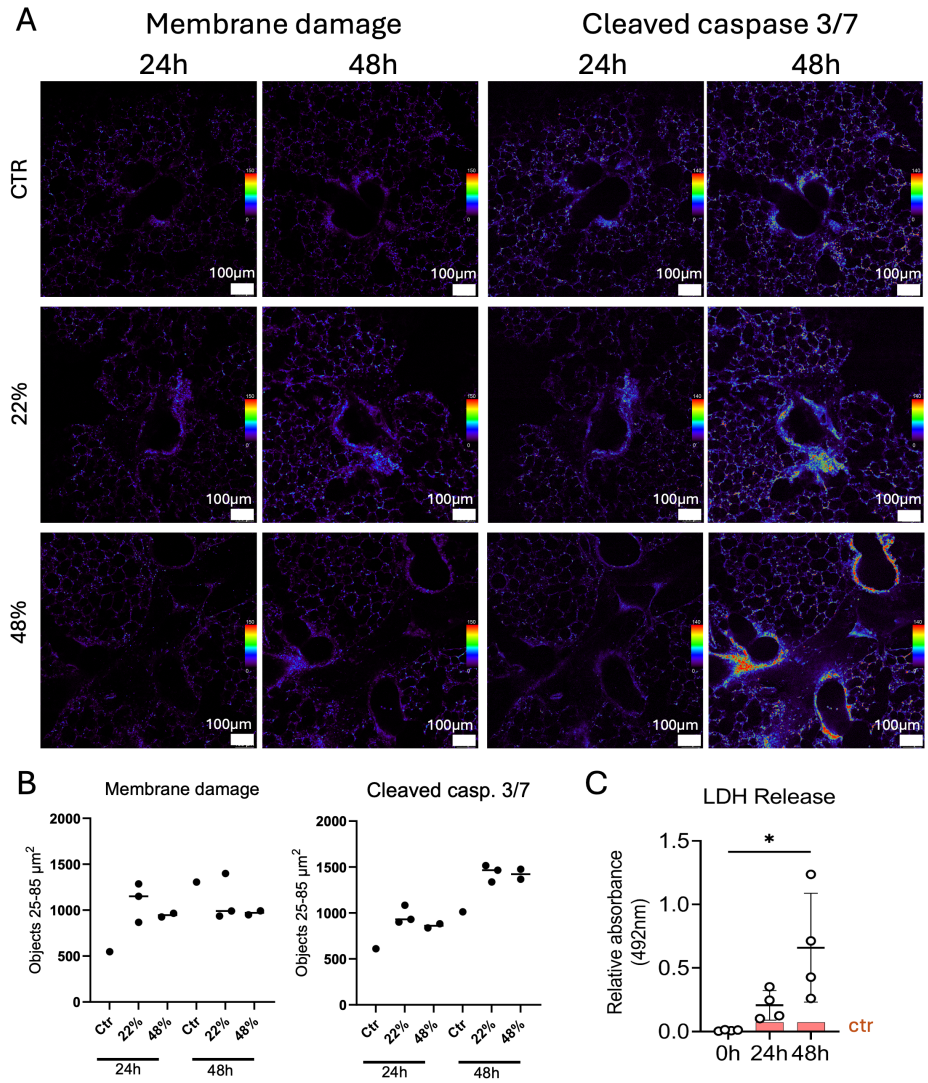

Figure 38. A) Representative single z-plane images acquired with live confocal microscopy and pseudocolored with a multicolor LUT to represent pixel intensity of O-PTIR irradiated and non irradiated (CTR) PCLS. B: quantification of objects corresponding to murine nuclei to assess membrane damage (RedDot2 nuclear stain) and cleaved caspase 3/7 staining (NucView 488 nuclear stain) 24h and 48h of culture. C) Lactate dehydronase release in supernatants for 48h of PCLS culture. A) and B) reanalyzed for this thesis C) reproduced from (Gvazava et al. 2023) with permission

Taken together, these findings suggest that O-PTIR imaging of airway regions in PCLS may induce mild local cellular stress, reflected by increased caspase-3/7 activity and elevated LDH release over time. Nevertheless, the lack of pronounced membrane permeability changes and the maintenance of ciliary beating demonstrate that the tissue remains viable under the applied imaging conditions.

However, live O-PTIR imaging still represents a form of live-tissue imaging and therefore the general requirements associated with maintaining tissue viability during microscopy remains. As discussed previously, live imaging requires careful control of several experimental parameters, including tissue hydration, temperature, CO_2 levels and other environmental conditions as well as duration and intensity of illumination during imaging. If these conditions are not sufficiently optimized, the tissue may undergo drying, mechanical stress and phototoxicity during the imaging process.

Therefore, further implementation of live O-PTIR imaging requires not only optimization of imaging parameters but also appropriate adaptation of the sample-support system. As discussed earlier, the brain slice experiments were performed using a specialized environmental chamber specifically designed to maintain tissue viability. This chamber provided stable physiological conditions throughout imaging and was instrumental in preserving tissue health. In contrast, an equivalent specialized live-imaging chamber was not available during the lung tissue experiments. The PCLS were therefore imaged using standard histological slides that provided less control over the local microenvironment. Although the viability assessments presented above demonstrate that the tissue remained viable under these conditions, the use of a dedicated environmental chamber for future live lung O-PTIR studies could further improve tissue preservation.

Forward and Reverse Optical Clearing of Large Samples for LSFM Imaging

Optical tissue clearing is a groundbreaking technique that has transformed our ability to image large, complex tissues and whole organs with subcellular resolution in 3D using advanced microscopes such as light sheet fluorescence microscopy (LSFM). As discussed in the introduction of this thesis tissue clearing methods can be broadly categorized into one of three categories:

1) Hydrophilic (e.g., CUBIC(242) , SHIELD(243))
2) Hydrophobic (e.g., Solvent-based tissue clearing (3DISCO(199) , iDISCO(195), uDISCO(197))
3) Hydrogel-based.

While hydrophilic techniques such as CLARITY(244) and SeeDB(245) are relatively easy to implement in standard laboratory settings, they often require prolonged incubation times ranging from days to weeks (depending on tissue size). In contrast, organic solvent-based methods have gained widespread application due to their ability to rapidly achieve superior levels of transparency. However, organic solvent approaches suffer from notable drawbacks, including tissue shrinkage caused by extensive dehydration as well as quenching of endogenous fluorescent proteins (e.g., green fluorescent protein (GFP))(246). Therefore, they require antibody labelling which increases both experimental cost and time. To overcome this, alternative strategies have been developed, including the use of longer-chain or branched alcohols as well as heterocyclic compounds for dehydration under controlled pH conditions. For instance, fDISCO(196) utilizes tetrahydrofuran (THF) at +4°C and alkaline pH 9, while 2Eci(205), another solvent-based clearing method, employs 1-propanol under similar environmental conditions. Despite their effectiveness, these methods rely on toxic and costly solvents and have thus far remained limited to endpoint imaging with no possibility for further molecular analyses on the same tissue.

Therefore, there is a growing need for newer organic solvent based optical clearing protocols which preserve endogenous fluorescence, can be more readily implemented in laboratories setup for biomedical science and can be reverted after three-dimensional imaging to support additional molecular analyses. In paper III we present PROTEUS, a novel isopropanol-based tissue clearing approach enabling forward and reverse optical tissue-clearing to increase the usability of samples. PROTEUS: a new low shrinkage and endogenous fluorescence preserving tissue clearing method

Previously published protocols aiming to preserve endogenous fluorescence proteins utilized branched alcohols, heterocyclic compounds or prolonged incubation in the primary alcohol 1-propanol followed by refractive index matching

in hydrophobic imaging solutions such as ethyl cinnamate. However, we noted that despite known differences in lipid extraction efficiency between 1 and 2-propanol, and thus presumed improvement in tissue transparency, there has been no previous assessment of 2-propanol for optical tissue clearing. Therefore, we hypothesized that 2-propanol (commonly referred as Isopropanol) may offer distinct advantages over the other protocols since it is a secondary alcohol and has lower polarity. Further, as mentioned above, organic solvent-based clearing protocols are known to induce substantial volumetric attrition (tissue shrinkage) during dehydration, which can distort anatomical spatial relationships.

We first sought to compare the clearing efficiency of each of the previously published fluorescent-retaining clearing protocols such as uDISCO(197), fDISCO(196) and 2Eci(205) and most commonly used tissue clearing protocols iDISCO, with 2-propanol-based clearing (PROTEUS). For this, we chose 8 mm in diameter bovine liver tissue sliced to a consistent thickness of 1 mm due to the fact that liver is known to be challenging for tissue clearing, due to its dense structure preventing sufficient lipid removal. Further its high levels of pigmentation and hemoglobin contribute to strong light absorption, further hindering optical clearing and large-volume imaging.

Subjectively, all tissue clearing protocols achieved sufficient transparency for LSFM, as evidenced by the ability to visualize grid paper underneath through the samples after incubation in the refractive index matching solution (**Figure 39A**). However, assessment of dimensional changes following tissue clearing showed that uDISCO, fDISCO and 2ECi induced more than 50% shrinkage relative to the initial tissue size, whereas iDISCO and PROTEUS resulted in less than 50% shrinkage on average. Furthermore, iDISCO and PROTEUS protocols caused significantly less tissue shrinkage compared to uDISCO and fDISCO (**Figure 39B**).

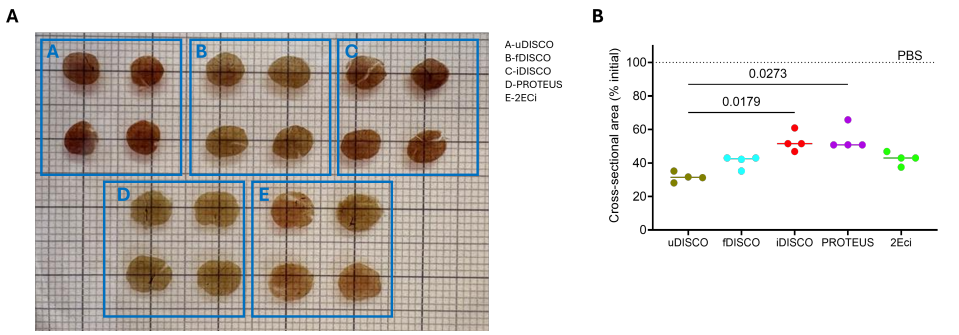

Figure 39. A) Representative images of optically cleared bovine liver. Images were acquired while samples were immersed in the refractive index matching solution, ethyl cinnamate (ECi), after the following tissue clearing protocols were performed a) uDISCO; b) 2Eci; c) fDISCO; d) PROTEUS (described in this paper); e) iDISCO. B) Degree of shrinkage quantification after tissue clearing protocols (n=4 technical replicates). Mean ± s.d. *$p < 0.05$ assessed by one-way ANOVA with Brown-Farsythe and Welch multiple comparisons test. Figure reproduced from (Gvazava et al. Manuscript)

Initially all liver biopsies were randomly selected across experimental groups. Notably in our experimental groups of n=4 PROTEUS resulted in more homogeneous (uniform) shrinkage across samples. A certain degree of shrinkage is expected in solvent-based clearing methods since all such protocols include a dehydration step that leads to volume reduction.

Dimensional changes can be viewed from both negative and positive perspectives. On the one hand, shrinkage may be considered a drawback, as it alters the native size and potentially the spatial relationships within the tissue. On the other hand, this reduction in tissue size can be advantageous, particularly for larger species of organs. Simply these samples can fit in the microscopes and imaging within the field of view of light-sheet fluorescence microscopy (LSFM) consequently reducing imaging time and data volume.

Importantly, the primary goal of tissue clearing is to achieve refractive index homogenization, thereby reducing light scattering and achieving optical transparency after reflective index matching. Therefore, clearing methods that balance effective transparency with limited shrinkage represent a significant advantage.

To quantitatively assess clearing efficiency across all protocols, we performed UV–Vis spectroscopy (**Figure 40A**). To complement the UV-Vis, we quantified total absorbance using area under the curve (AUC) analysis. As an integrated measure of light absorption across the full spectral range, AUC serves as a robust proxy for overall optical clarity. Among all protocols, PROTEUS exhibited the lowest AUC, reflecting reduction in total absorbance and the highest degree of optical transparency (**Figure 40B**).

To further resolve differences between groups, we applied principal component analysis (PCA) to the spectral data. PCA clearly separated non-cleared from cleared tissues into two distinct clusters, confirming that optical clearing induces a measurable and systematic shift in tissue optical properties. Notably, iDISCO, 2ECi, and PROTEUS were positioned furthest from the non-cleared cluster, indicating that these protocols produced the greater spectral deviation from the native (uncleared) state(**Figure 40C**). This is consistent with more efficient removal of absorbing and scattering components and more complete refractive index homogenization.

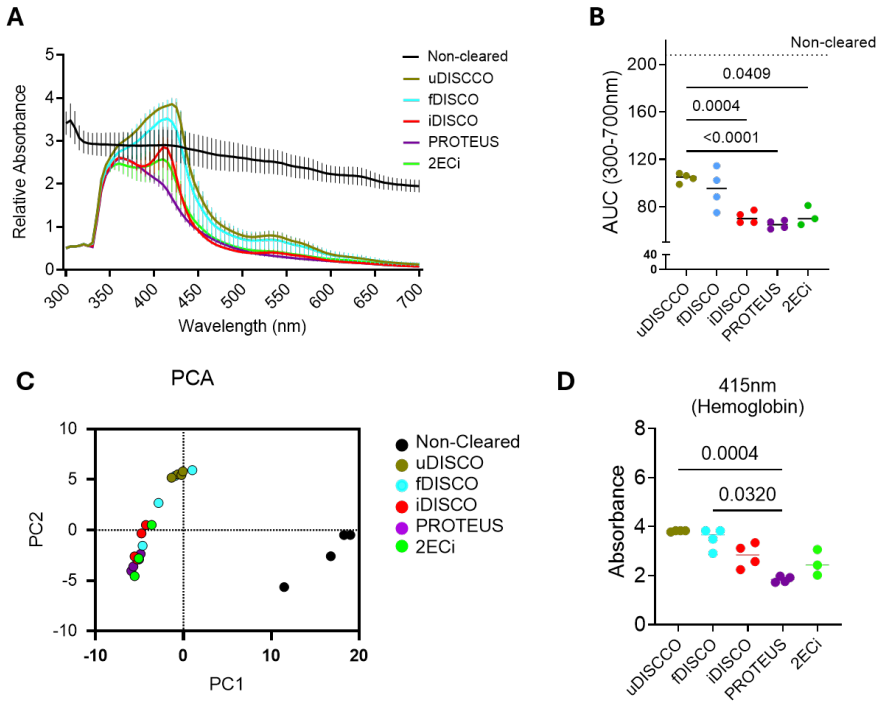

Figure 40. A) Relative absorption spectra (i.e. background corrected for RI matching solution) measured from bovine liver discs after tissue clearing; non-cleared tissue served as a control (wavelength range = 300nm-700nm; 5nm step size). A decrease in overall absorption is observed in samples cleared using the PROTEUS protocol (n=4) B) Area under the curve (AUC) calculated from absorption spectra. Samples cleared using the PROTEUS protocol exhibited the lowest AUC values, indicating a greater overall reduction in light absorption compared with the other clearing methods. Mean ± s.d. *p < 0.05 assessed by one-way ANOVA with Brown-Farsythe and Welch multiple comparisons test. C) PCA D) Extracted 415nm absorption peak (haemoglobin) showing a reduction during PROTEUS tissue clearing. Mean ± s.d. *p < 0.05 assessed by one-way ANOVA with Brown-Farsythe and Welch multiple comparisons test. Figure reproduced from (Gvazava et al. Manuscript)

Interestingly, we observed a marked reduction in the UV-Vis absorbance peak at 415 nm with PROTEUS (**Figure 40D**), which is associated with heme groups present in hemoglobin(247). This reduction in heme may be due to the prolonged contact in 2-propanol used in PROTEUS. 2-propanol is a mild chaotropic agent and has been previously suggested to be useful in removing heme groups from hemoproteins (248). Whether this effect generalizes across organs with distinct biochemical composition will require further study.

For our initial screening approach, we utilized bovine tissue liver from a butcher which contains a high amount of coagulated blood. This mimics research situations where residual, coagulated blood is known to be problematic for optical clearing

and imaging (e.g. post-mortem clinical tissue collection or non-heparinized animals) since it induces significant optical scattering and is highly autofluorescent. In many other optical clearing protocols, bleaching approaches are utilized to minimize the impact of residual blood, including hydrogen peroxide treatment. However, prolonged exposure to such reagents has been shown to damage tissue integrity as well as cause oxidative damage to biological molecules, making them challenging to detect using either label-dependent or independent approaches.

As discussed above, experiments were performed on liver tissue slices. However, most tissue clearing are performed on whole organs, where tissue volume can influence the extent of shrinkage during dehydration. To further address this question, we applied iDISCO and PROTEUS, causing less shrinkage in liver slices, to whole mouse brains (one of the most commonly used in tissue clearing) and we monitored volumetric changes throughout both the dehydration and refractive index matching steps(**Figure 41A**).

We observed that after PROTEUS tissue clearing, ~75% of the initial brain volume was preserved after dehydration with 2-propanol, with no further substantial changes observed following refractive index matching. In contrast, iDISCO-cleared brains exhibited a reduction to ~65% of their initial volume after dehydration with methanol, followed by partial expansion to ~75% upon refractive index matching (**Figure 41B**). This suggests that, in the case of iDISCO, additional structural changes occur between dehydration and refractive index matching, likely reflecting tissue relaxation effects. However, it is important to note that these experiments were conducted with a limited sample size and will require replication to confirm the observed trends.

To further assess long-term stability, the same clear brains were stored under identical conditions in ethyl cinnamate (ECi) at room temperature. Interestingly, after approximately two years of storage, iDISCO-cleared samples developed a milky appearance (**Figure 41C**). While extended shelf life of cleared tissues has been reported, many protocols favor alternative refractive index matching solutions over ECi for long-term storage. The observed milky appearance may result from a presently uknown chemical reaction between residual tissue chemical components and ethyl cinnamate, or from gradual oxidation. However, additional analyses are required to determine the precise reasons.

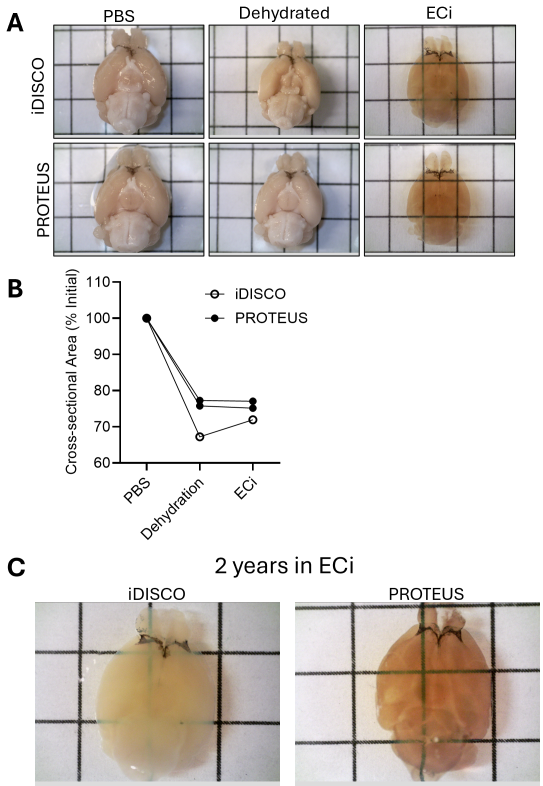

Figure 41. Shrinkage and qualitative assessment of optical tissue clearing of mouse brain using iDISCO and PROTEUS tissue clearing. A) Representative images taken at key intermediate stages using a DinoLite Camera on 5 mm grid paper during the tissue clearing process of mouse brain using iDISCO and PROTEUS protocols. B) Quantification of dimensional changes in percentage during dehydration and after Ethyl cinnamate (Eci) compared to original organ size in PBS. C) Tissue transparency changes after 2 years in ECi . A) and B) reproduced from (Gvazava et al. Manuscript) C) for this thesis

As mentioned above, a major limitation of solvent-based tissue clearing is the rapid quenching of endogenous fluorescent proteins. While techniques such as uDISCO and fDISCO have been developed to better preserve GFP and other endogenous fluorescent proteins, each has distinct limitations. uDISCO is unable to preserve tdTomato fluorescence and fDISCO samples must be imaged within hours after completion of optical tissue clearing due to generation of peroxides in the RI matching solution at room temperature. Therefore, imaging on different LSFMs on different days or transporting samples is not feasible. Furthermore, chemicals used in both protocols require specialized handling due to their high volatility as well as temperature requirements. We also observed that samples treated using the fDISCO protocol (THF) were more fragile, leading to sample loss during routine handling. Owing to these limitations, we did not utilize uDISCO or fDISCO further.

Further, 1-propanol (2Eci) has been previously used for clearing and preservation of endogenous fluorescent proteins in organoids and model organisms(205). Therefore, we sought to compare the ability of 2-propanol and 1-propanol to preserve endogenous fluorescence. We chose to use native GFP due to the fact that it is still widely used in transgenic models and is known to be more prone to denaturation as compared to more stable variants used in previous studies (e.g. EGFP). Methanol (i.e. (iDISCO) was used as a negative control due to the fact that it has been previously reported to quench fluorescence in endogenous fluorescent proteins. We also varied pH and temperature during dehydration as this has been previously shown to play a role in retaining fluorescence for 1-propanol based optical clearing. Recombinant GFP was embedded in agarose hydrogels via chemical fixation with 10% neural buffered formalin (NBF) and gels were thereafter subjected to gradual dehydration in each of the alcohols at pH=7 and pH=9 at room temperature or +4°C. As previously reported, dehydration with methanol resulted in a complete loss of the well-known 508nm GFP emission peak (λ_{ex}=395nm) (**Figure 42**). On the other hand, both 1- and 2-propanol demonstrated retention of the 508nm emission peak at comparable fluorescence levels. Similar to other recent studies aiming to retain fluorescence during optical clearing dehydration at +4°C and alkaline pH of 9 showed the highest preservation of GFP fluorescence in both 1-propanol and 2-propanol. This confirms that alkaline pH and lower temperature, in combination with longer chain alcohols, are both critical for retaining GFP fluorescence.

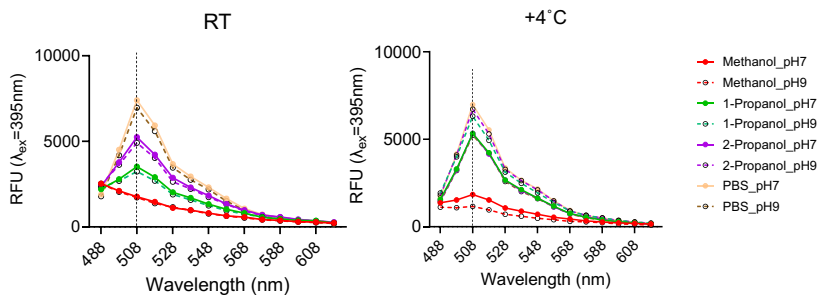

Figure 42. Emission spectra of dehydrated rGFP agarose gels after overnight incubation at room temperature or 4°C, at pH 7 and pH 9, in the respective alcohol solutions (n = 2 technical replicates). Figure reproduced from (Gvazava et al. Manuscript)

To further understand the kinetics of fluorescence quenching and at which percentages of alcohol this occurred, we repeated this same experiment but performed fluorescence readings between each dehydration step. Based on our previous results for these experiments, all dehydration steps were conducted at +4°C and at pH 9. All alcohols demonstrated an initial loss of fluorescent signal in as little as 20% alcohol, but methanol continued to decrease thereafter with increased alcohol concentrations while 1- and 2-propanol were fluorescence were mentioned (**Figure 43A,B**). After the dehydration protocol overnight, there was almost no

detectable fluorescent signal in methanol but 1- and 2-propanol retained around 60% of their baseline fluorescence (**Figure 44A-C**). Based on its lower toxicity, cost and reactivity when compared and improved overall optical transparency compared to 1-propanol, we proceeded to test the effects of 2-propanol in tissue samples containing endogenous fluorescent proteins.

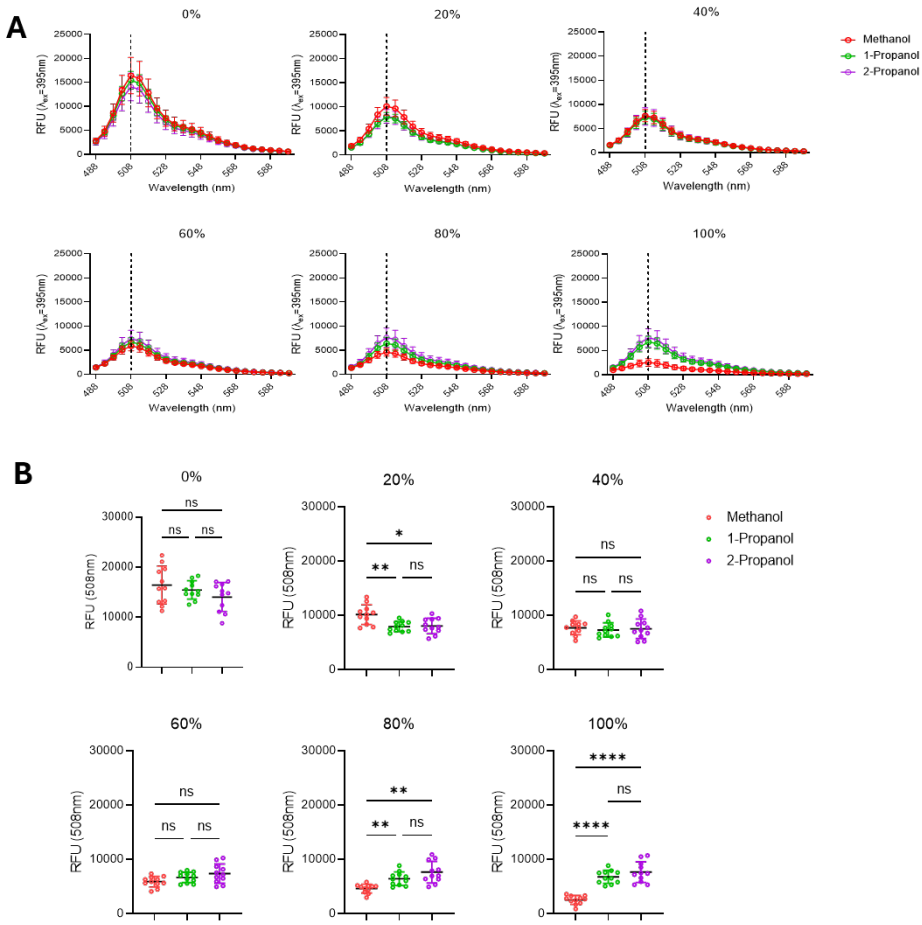

Figure 43. Effect of different linear alcohols used for dehydration during organic solvent-based tissue clearing on the fluorescence emission properties of recombinant green fluorescence protein (rGFP) immobilised in 2% agarose: methanol (MeOH), 1-propanol (1-Prop) and 2-propanol (2-prop). A) Relative fluorescence intensity spectra of rGFP during dehydration with Methano, 1-Propanol and 2-Propanol (dashed line indicates the highest fluorescence emission peak at 508 nm (n = 11 technical replicates) B) Comparison of peak fluorescence emission values at 508 nm during the dehydration process. Statistical significance was assessed using a one-way ANOVA followed by Brown-Farsythe and Welch multiple comparisons test. (n=11 technical replicates per condition). Figure reproduced from (Gvazava et al. Manuscript)

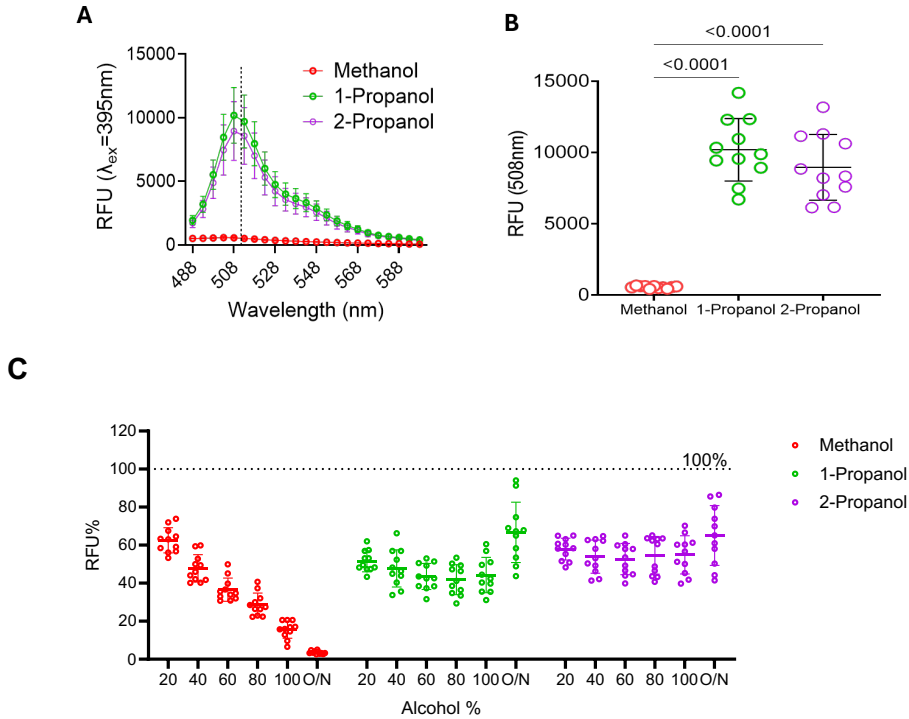

Figure 44. Changes in relative fluorescence intensity during dehydration are shown as percentage loss relative to the same cells in PBS (set as 100%). Figure reproduced from (Gvazava et al. Manuscript)

As tdTomato has been shown to be particularly sensitive to optical tissue clearing protocols. We decided to use a transgenic mouse brain model where tdTomato is expressed under the control of the promoter region for the leptin receptor (*LepR*). This model has been previously shown to label a small population of LepR+ cells located predominantly in the median eminence, a subregion of the hypothalamic area. Due to the location of the median eminence and its small size, this is an otherwise challenging region of the brain to image and is therefore well-suited for whole organ LSFM imaging. We performed optical clearing in whole-brains using the original iDISCO clearing method as well as our protocol containing 2-propanol as the dehydration agent (later referred to as PROTEUS). ECi was used as RI matching solution for both tissue clearing protocols. Next, we imaged whole LepR-TdTomato murine brains which were optically cleared with PROTEUS or iDISCO using a dual illumination and single objective LSFM with identical laser settings (i.e., Miltenyi UltraMicroscope Blaze). We saw that tdTomato was both readily visualized using the PROTEUS protocol and was specific to the previously reported hypothalamic region (**Figure 45, Figure 46**). In contrast, we could not detect any tdTomato signal in brains cleared using the iDISCO protocol.

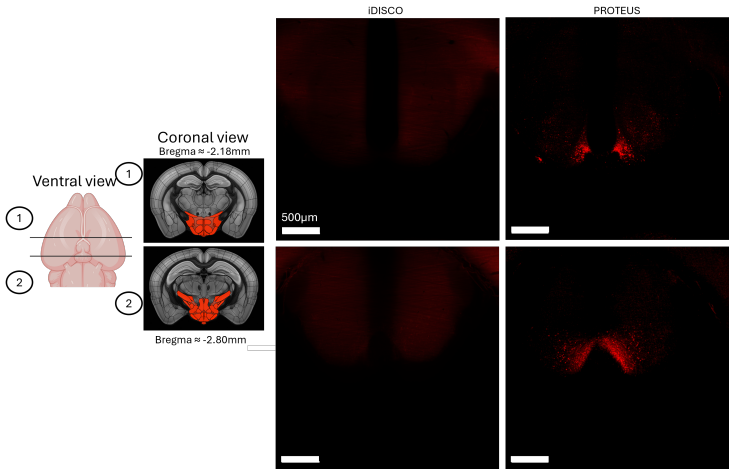

Figure 45. Schematic of the hypothalamic region of interest (red circles) and corresponding light sheet fluorescence microscopy images of the same regions. Representative single plain light sheet fluorescence imaging of the median eminence of a LepR-TdTomato mouse using iDISCO and PROTEUS. Imaging was performed on a UltraMicroscope Blaze with a 4x objective with dual sided illumination and dynamic focusing and laser power of λ568=10%. All images were visualized and pseudocolored using Imaris software. Figure reproduced from (Gvazava et al. Manuscript)

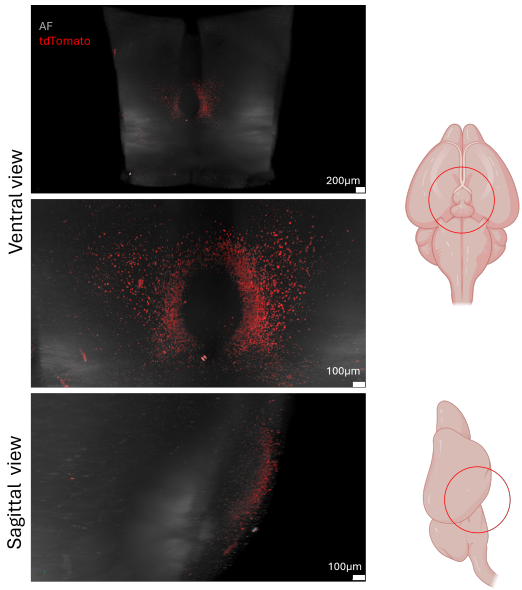

Figure 46. Representative light sheet fluorescence imaging of the median eminence of a LepR-TdTomato mouse using PROTEUS. A) Maximum intensity projections (MIPs) of ventral and saggital views generated in Arivis. Figure reproduced from (Gvazava et al. Manuscript)

Importantly, we imaged the same brain 63 days after optical clearing when stored in the dark at room temperature (**Figure 47**). While we observed some qualitative

decreases in fluorescence intensity over time, similar structures remain visible when similar planes were visualized within the median eminence.

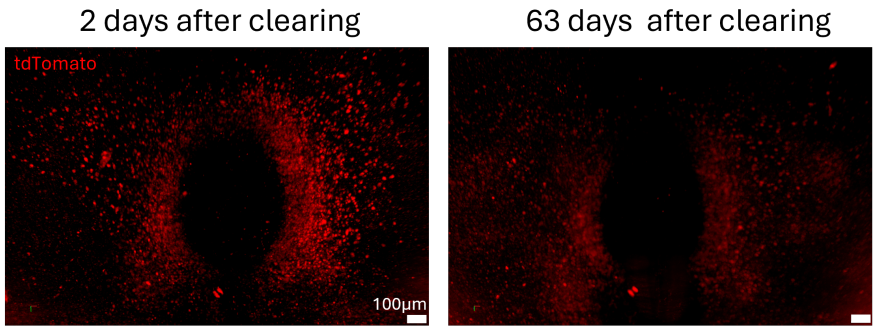

Figure 47. MIP views of a similar field of view 2 and 63 days after PROTEUS clearing showing retention of detectable TdTomato. General loss of fluorescence can still be observed (subjectively assessed based on the number and pattern of fluorescence). Schematics in subpanel A generated using Biorender. Imaging was performed on a Miltenyi Blaze with a 4x objective with dual sided illumination and dynamic focusing. Figure reproduced from (Gvazava et al. Manuscript)

However, it is important to remember that the stability of fluorescent proteins is widely dependent on the surrounding environment. For example tissue-clearing methods such as SHIELD incorporate an additional post-fixation crosslinking step to enhance stabilization, "shielding" fluorescent proteins against chemical and structural degradation. In the case of 2-propanol, the secondary position of the hydroxyl group increases steric hindrance around the functional group, which reduces hydrogen bond accessibility, which may contribute to the stabilization of endogenous fluorescent molecules during the dehydration process. However, following treatment with DCM and RI matching with ECi , 2-propanol is largely "washed out" of the tissue. Additionally, ECi itself can undergo oxidation over time, which may further influence the stability and long-term preservation of fluorescence. Therefore, for stabilization of EFPs additives in ECi may be beneficial for maintaining fluorescence over extended periods.

Imaging complex and intricate tissue structures can be achieved using PROTEUS

While comparing diverse tissue clearing protocols, we observed that superior tissue transperency following tissue clearing by PROTEUS. Therefore, we sought to further test the capability of PROTEUS to be used to visualize anatomical structures which are known to be challenging to visualize due to light scattering caused by imperfect tissue transparency. In particular, high-resolution visualization of ubiquitous and fine tissue structures (e.g. vasculature network or neuronal circuits) is known to be challenging to image at high resolution due to their dense physical

and intertwining nature. Because these structures are present in high amounts and distributed evenly, their signals can overlap with one another, making it difficult to distinguish individual components. Their structural density also results in light scattering as light passes through these regions, resulting in decreased spatial resolution and diminished signal to noise ratio. Combined with inherent tissue autofluorescence, visualization of these structures is challenging. However, it is crucial to study their changes with high spatial resolution and within intact 3D volumes to better understand their physiological function or pathological progression.

Neuronal activity critically depends on an extensive vascular network that delivers oxygen and nutrients. Moreover, malformations in cerebral blood vessels contribute to the pathogenesis of various neurological disorders, such as stroke and epilepsy. The blood–brain barrier (BBB), primarily composed of endothelial tight junctions, maintains the chemical composition of the neuronal environment by preventing the entry of blood-derived substances into the brain. Dysfunction of the BBB leads to the diffusion of these substances into the brain parenchyma, resulting in neuronal damage.

The brain regions located around the ventricles, termed circumventricular organs (CVOs), are often referred to as the "windows of the brain". These regions are characterized by relatively large perivascular spaces, specialized ependymal cells and fenestrated capillaries(249). CVOs allow direct sensing of blood-derived signals and the secretion of hypothalamic neuropeptides via their permeable capillaries. Accumulating evidence highlights the crucial roles of CVOs in various physiological regulatory pathways, including the homeostasis of osmolarity, sodium balance, body temperature, energy metabolism, chemoreception of blood-derived substances, and neuroinflammatory responses (249).

To visualize both continuous and fenestrated capillaries, we administered fluorescent dyes (Dextran-568 and Lectin- lectin-647) into the mouse tail vein and allowed the dyes to circulate prior to euthanasia and extraction of the brain. Lectin dyes are able to cross the BBB after systemic injection and are known to selectively bind to endothelial cells (**Figure 48**). Dextran was administered in order to more readily confirm fenestrated capillaries as these dyes would selectively leak out and be located within regions containing fenestrated capillaries. For these samples, we choose to image in two complementary light-sheet microscopes. First, whole brains were imaged using a Blaze light-sheet microscope to obtain a three-dimensional overview of the entire organ. Subsequently, the median eminence was dissected and imaged using a selective plane illumination microscope (SPIM) equipped with an Airy beam (MSquared Aurora) (**Figure 49**). Owing to its non-diffracting and self-healing properties, this beam is particularly well suited for imaging highly scattering tissues. Using this workflow in combination with PROTEUS-cleared samples, we successfully visualized the vasculature down to the level of single capillaries and

reconstructed these structures in 3D, demonstrating the capability for high-resolution imaging following PROTEUS tissue clearing.

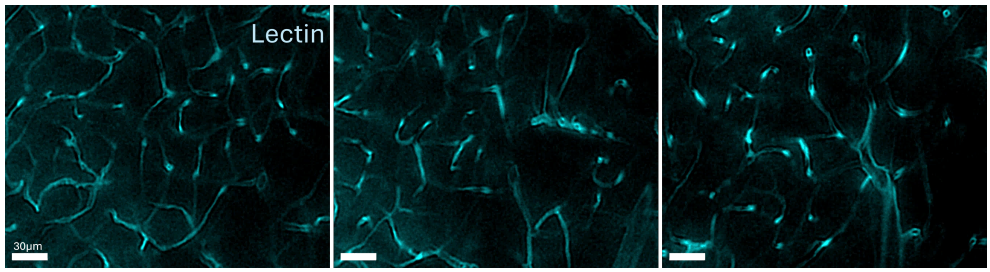

Figure 48. Representative single plane LSFM images of the mouse median eminence demonstrating the ability to detect the vascular network using lectin administered in vivo prior to sacrificing the animal and extracting the brain tissue for LSFM. Lectin labels all endothelial cells while 10kDa-dextran was administered to visualize capillary leakage. Figure reproduced from (Gvazava et al. Manuscript)

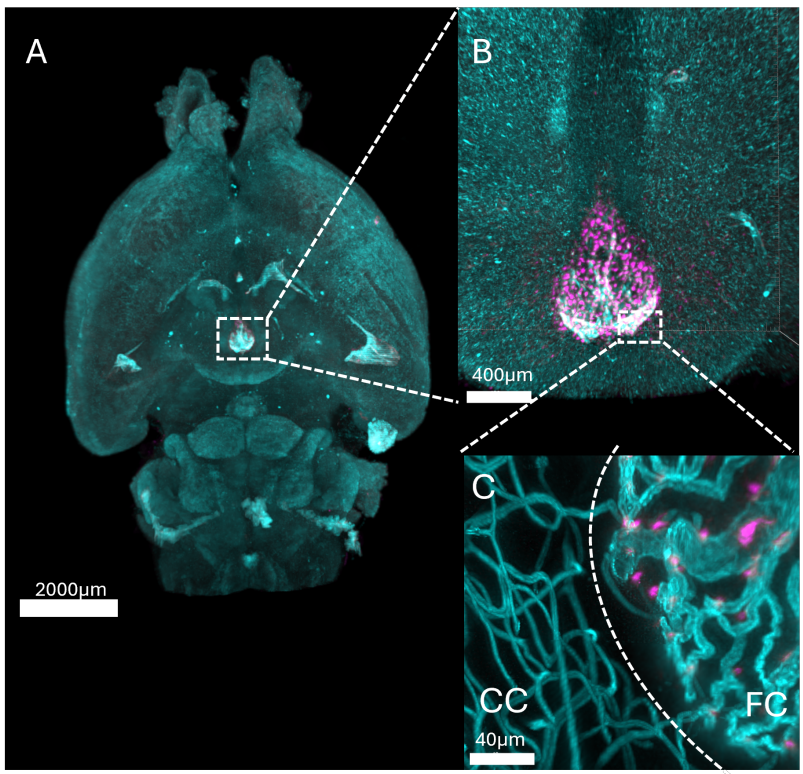

Figure 49. 3D rendering of a mouse brain and highly vascularized region of the median eminence. Cyan (lectin) and magenta (Dextran) signals distinguish the transition zone between continuous capillaries (CC) and fenestrated capillaries (FC). Imaging was performed using 2 light-sheet microscopes A, B) Blaze-Ultramicroscope and C) M-Squared Aurora and pseudocolored using Imaris software. Figure reproduced from (Gvazava et al. Manuscript)

Next, we aimed to visualize another ubiquitously present and structurally complex element in the brain, the fine myelinated network of the human brain which is approximately three to four times more densely myelinated than that of the mouse. Myelin lipid-rich sheath that wraps around axons, for rapid saltatory conduction of action potentials, overall neural circuit efficiency and metabolic support of axons.

Human cortical tissue samples were obtained from epileptic zone resection surgeries and immediately sectioned into 300 µm-thick vibratome slices. After fixation with paraformaldehyde, slices were immunostained with primary antibodies against Myelin Basic Protein (MBP) to label myelinated fibers and Neuronal Nuclei (NeuN) to label neuronal cell bodies (**Figure 50**). Further this tissue was cleared with PROTEUS and imaged using dual-sided illumination and single-objective detection in the Blaze microscope. We were able to visualize both MBP and NeuN with expected spatial distributions consistent with the selected anatomical regions.

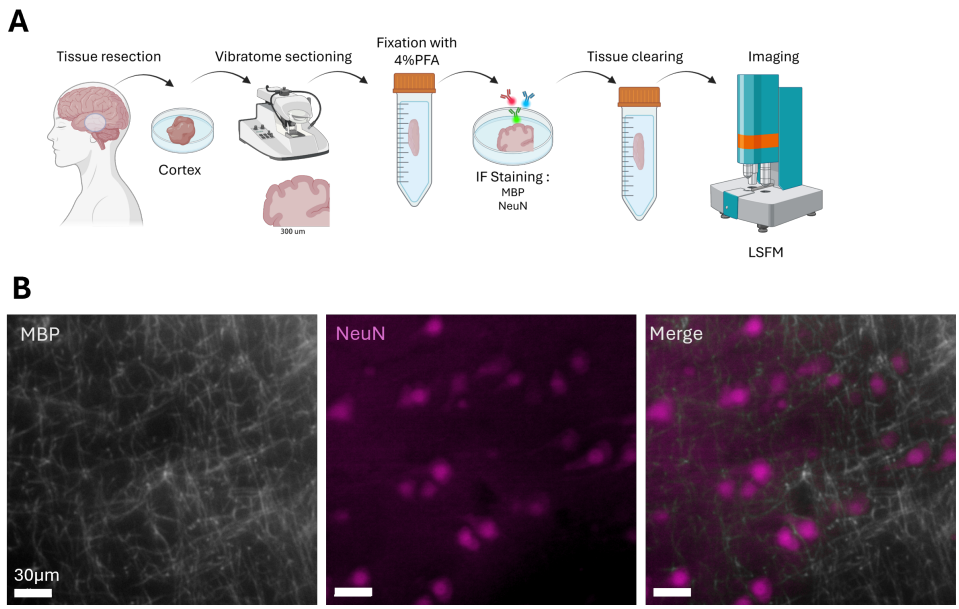

Figure 50. PROTEUS enables visualization of human cortical tissue containing dense neurons. A) Schematic diagram illustrating the methodology for the generation of acute brain slices from human cortical tissue. B) Representative single plane light sheet microscopy images of human cortical tissue. Myelin Basic Protein (MBP) is labeled in gray (to identify myelin/white matter tracts) and Neuron-specific Nuclear Protein (NeuN) is labeled in magenta (to identify neuronal nuclei). The merged image shows the spatial relationship between myelinated structures and neuronal bodies. Imaging was performed on an Ultramicroscope Blaze light sheet microscope with an 12x objective, with dual sided illumination. Figure reproduced from (Gvazava et al. Manuscript)

After confirming retention of EFP's and ability to image complex and intricate tissue structures using PROTEUS, we sought to confirm if our protocol could simultaneously visualize intricate vascular networks in samples which contained

both antibody labelling as well as endogenous fluorescent proteins in mouse skin samples. The skin, comprising epidermis, dermis and subcutaneous adipose tissue and its dense hair follicles and intense hair pigmentation and lipid-rich composition, represents a particularly challenging tissue for optical clearing. We employed a xenotransplantation model in which eGFP-expressing rat microvessels were transplanted subcutaneously under the skin of a immunocompromised mouse model (*Rag1*-/-) and placed within an optical window for visualization of anastomosis with the host using intravital microscopy. Vessels which successfully anastomosed after 7 days were harvested and fixed and immunolabeled for CD31 to visualize the vascular endothelium (**Figure 51A**). Prior to the onset of optical clearing, mouse hair was chemically removed to eliminate optical interference during LSFM imaging. We found that PROTEUS achieved effective transparency across all skin layers enabling visualization of both endogenous fluorescent proteins as well as antibody-labeled CD31 vessels. The retention of endogenous GFP from the donor vessels readily enabled us to distinguish transplanted microvessels from those which were host-derived (**Figure 51B**). These results demonstrate that PROTEUS enables efficient optical clearing of highly pigmented and lipid-dense tissues while preserving both endogenous and antibody-derived fluorescence.

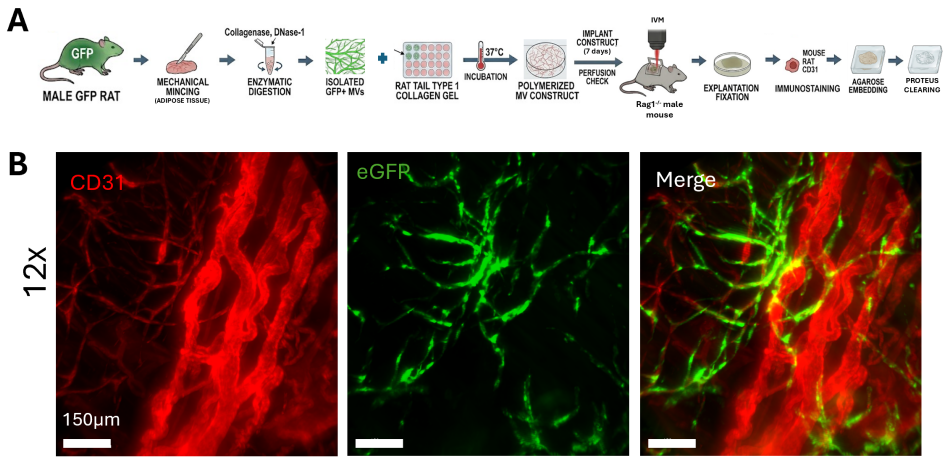

Figure 51. A) Schematic of 3D reconstruction of blood vessels showing endogenous eGFP transplanted micro-vessels (MVs). Schematic created in using Google Gemini under supervision. B) wavelength range that spanned from 300nm to 700nm using a step size of 5nm. Volumetric rendering of explanted skin grafts from RAG1- mouse transplanted with eGFP MVs construct. Imaging was performed on the UltraMicroscope Blaze using 12x magnification, CD31-Red and eGFP-green. All images were visualized and pseudocolored using Imaris software. Figure reproduced from (Gvazava et al. Manuscript)

PROTEUS clearing of tissue heterogeneous Early-stage embryos can be achieved

Given the natural transparency of pre-embryonic development, direct visualization has allowed extensive studies for centuries of fertilization, zygotic activity, cleavage and gastrulation. However as the embryo develops, increasing lipid content, deposition of ECM, pigment accumulation and organogenesis progressively increase opacity and consequently limits the visualization of mid- to late- stage processes in whole specimens without subsequent sectioning. Therefore, tissue clearing combined with 3D imaging provides complex spatial and temporal dynamics underlying development biology. Moreover, developing embryos encompass all tissue types and their relatively small size particularly well suited for light sheet microscopy. However, embryonic tissue is still immature (e.g. ECM maturation, cell differentiation) they are especially vulnerable to damage during tissue clearing. We selected embryos from two species commonly used for studying development: chick and mouse. We found that PROTEUS clearing enabled imaging of entire chick embryos at embryonic day 3 and day 5 and that all major, expected anatomical structures could be visualized using tissue autofluorescence throughout the entire thickness of the embryo (**Figure 52**). Next, we chose to clear and image E10 murine embryos due to the fact that this timepoint marks the critical transition from simple germ layers to organogenesis where major anatomical structures such as the brain, heart and limbs first become visible. For this, we chose to excise entire murine placentas to enable visualization of embryonic development in the spatial context of the placenta. We found that PROTEUS resulted in subjectively well cleared E10 embryos and that we were able to visualize all major anatomical features at this time point (**Figure 52**), including visualization of major organs at E15.5, a developmental timepoint where most major organogenesis has occurred with the exception of calcification (**Figure 52**).

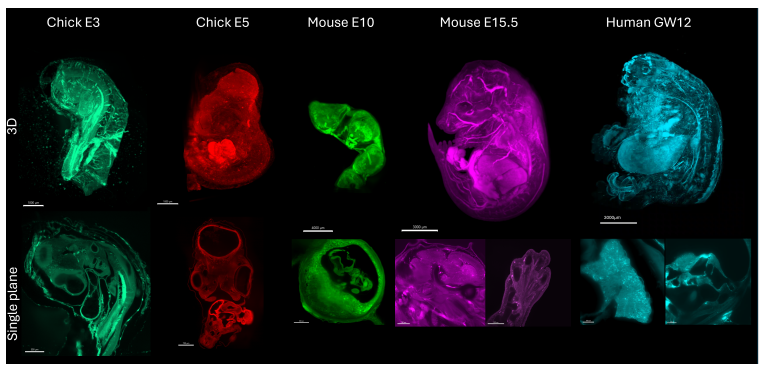

Figure 52. 3D and representative plane LSFM images of cleared chick and mouse embryos and human fetus. Imaging was performed on the UltraMicroscope Blaze with the 1x and 4x objectives. All images were visualized and pseudocolored using Imaris software. Figure reproduced from (Gvazava et al. Manuscript)

Taken together, our ability to clear diverse embryos across multiple developmental stages, combined with the immunolabeling compatibility of the PROTEUS pipeline, we thought extend out tissue clearing protocol to human fetal tissue, specifically gestational week 12 samples (**Figure 53**). At this stage, all major organs are developed, however extensive cellular migration, differentiation and maturation are still ongoing. Importantly, the tissue remains largely non-calcified, making it highly suitable for optical clearing. This developmental window is therefore of considerable interest from both a biological and methodological perspectives. Given the limited availability and high value of human fetal tissue, analyzing samples in their intact three-dimensional context provides critical insight into human developmental processes that cannot be fully recapitulated in 2D.

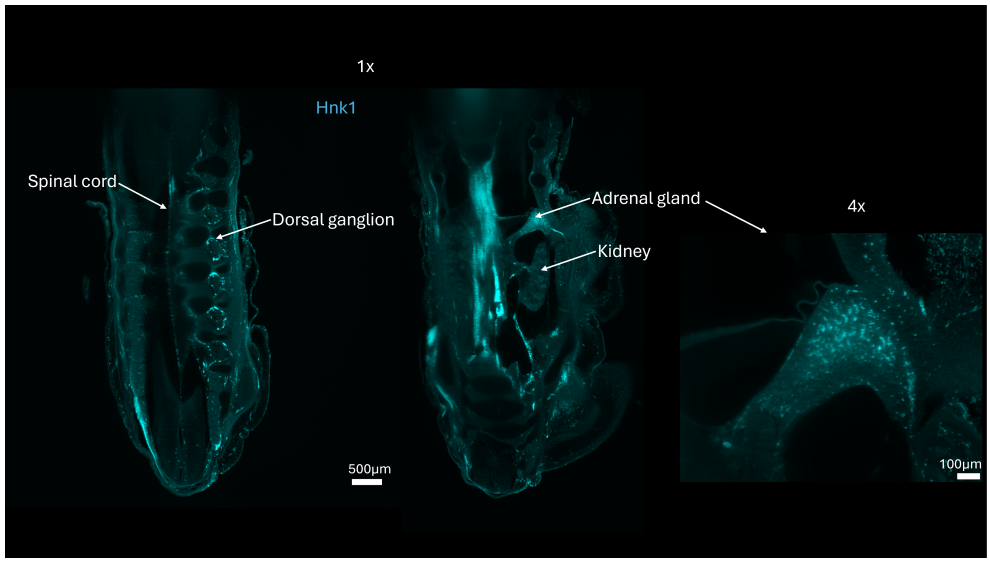

Figure 53. Representative single plane LSFM images of 12week human fetus. HNK-1 umuno staining in cyan, showing neuronal-crest cells. Imaging was performed on the UltraMicroscope Blaze with the 1x and 4x objectives. All images were visualized and pseudocolored using Imaris software. Figure made for this thesis

Our interest was neuronal crest cells, a transient and multipotent stem cell population that originates from the neuroectoderm at the dorsal margins of the neural tube following neurulation (250). Initially epithelial, these cells undergo epithelial-to-mesenchymal transition (EMT), enabling them to migrate extensively throughout the embryo. As they migrate giving rise to a broad range of derivatives across multiple tissue types, including peripheral neurons and glial cells, melanocytes, craniofacial cartilage and bone, as well as endocrine chromaffin cells of the adrenal medulla (250).

To visualize neural crest–derived populations within the human fetal tissue, we performed immunostaining using an HNK1 antibody, followed by PROTEUS tissue

clearing. After clearing and LSFM imaging, we observed prominent HNK1-positive cell populations distributed along the dorsal axis (**Figure 53**) of the fetus, consistent with migratory streams of neural crest cells adjacent to the neural tube. Additionally, strong signal was detected within the adrenal gland region, specifically in the developing adrenal medulla (**Figure 53**), which is composed of densely packed neural crest–derived chromaffin progenitors. This spatial distribution aligns with the established migratory pathways and differentiation trajectories of neural crest cells at this developmental stage, reflecting their ongoing dispersal and integration into multiple organ systems.

PROTEUS is compatible with archival formalin fixed and paraffin embedded tissues

Pathologists routinely evaluate stained tissue sections with bright-field microscopy to assess malignancy, inflammation, fibrosis, tumor invasion, resection margins, and but this conventional approach is limited to planar 2D images and representative sampling of large specimens. Attempts to overcome these limitations through serial sectioning and 3D reconstruction, first explored in the 1960s–70s, have enabled visualization of tumor volume and architecture in biopsy specimens. However, this approach remains discontinuous, labor-intensive, and costly, as it requires processing hundreds of glass slides. In diagnostic pathology and preclinical research, excised tissues from patients or experimental animals are routinely fixed in formaldehyde and macroscopically examined to identify representative pathological regions for further analysis. This process is inherently subjective, and subtle or early pathological alterations e.g. breast ductal carcinoma in situ, may not be detected at this stage. Selected regions are subsequently paraffin-embedded, sectioned and stained, generating tissue blocks that are archived in pathology departments and tissue banks worldwide. Expanding the applicability of tissue-clearing and 3D-imaging technologies to these paraffin-embedded specimens would allow retrospective and large-scale histopathological studies. However, complete paraffin removal is needed, as paraffin is incompatible with ethyl cinnamate and significantly impedes light penetration.

To assess the feasibility of applying PROTEUS tissue clearing to FFPE samples, we first generated PCLS biopsies of identical size using a vibratome and a 4 mm biopsy punch . We chose to use agarose inflated lung tissue since it is easy to macroscopically identify highly similar regions (i.e., regions with or without airways) and their low tissue refractive index allows imaging of nearly full thickness slices without optical clearing. After identifying samples with similar tissue morphology, biopsies were divided into two groups: one underwent standard tissue processing and paraffin embedding, while the other was kept in PBS without processing. Paraffin was subsequently removed from the embedded samples using

one of two different methods: xylene or Histo-clear II. Both deparaffinized and unprocessed biopsies were then immunostained with α-tubulin, a marker of ciliated cells in airways and subjected to PROTEUS clearing followed by LSFM imaging using dual illumination and single objective imaging in the Blaze microscope. First we observe that all PCLS samples achieved sufficient tissue transparency (**Figure 54A),** as demonstrated by the ability to visualize underlying grid paper after incubation in the refractive index (RI) matching solution with minimal shrinkage differences (**Figure 54B**). Autofluorescence imaging using a 488 laser was initially employed to qualitatively assess the uniformity of paraffin removal, since incomplete deparaffinization or insufficient clearing would result in reduced signal-to-noise ratios, we did not noticed differences in autofluorescence between groups (**Figure 54C**), indicating removal of paraffin.

The development of effective deparaffinization and following tissue-clearing techniques opens ability for high-resolution 3D imaging of archival tissue specimens, expanding opportunities for retrospective studies and spatial tissue analysis in higly preciouse biological materials.

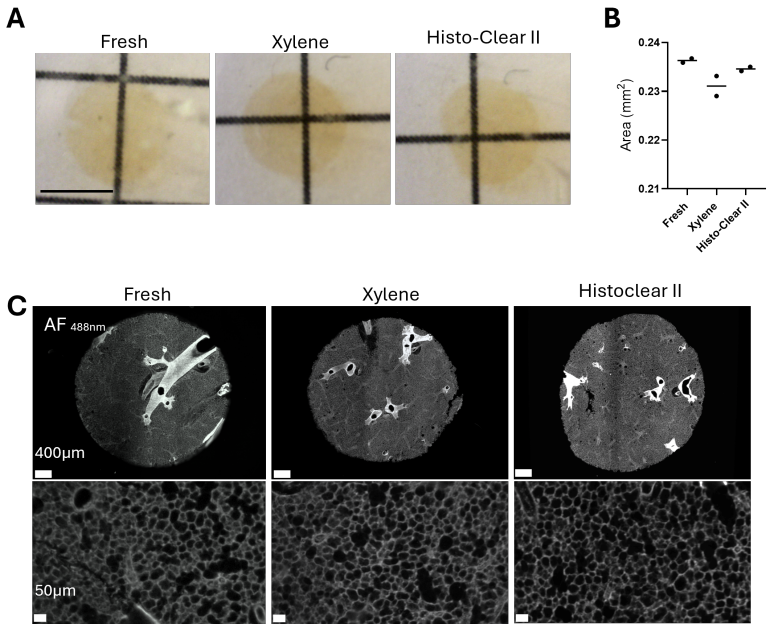

Figure 54. Representative images were captured with a DinoLite camera on 5 mm grid paper following refractive index (RI) matching with ethyl cinnamate (ECi). Comparisons include fresh (unprocessed) samples versus paraffin-removed samples treated with either Xylene or Histo-Clear II. C) Shrinkage assessment of optical tissue clearing of PCLS disks, initial size of all discs was 300µm thick and 4 mm in diameter (n=2). C) Representative 3D rendering using light-sheet fluorescence microscopy (LSFM) showing autofluorescence of PCLS with laser power of λ 488 nm - 7%. Figure reproduced from (Gvazava et al. Manuscript)

Furthermore, distinct and airway specific α-tubulin labelling was observed in all fluorescently stained sample (**Figure 55**) demonstrating preserved antigen epitopes following deparaffinization and confirming that deparaffinized tissues can subsequently be cleared using PROTEUS and imaged using LSFM.

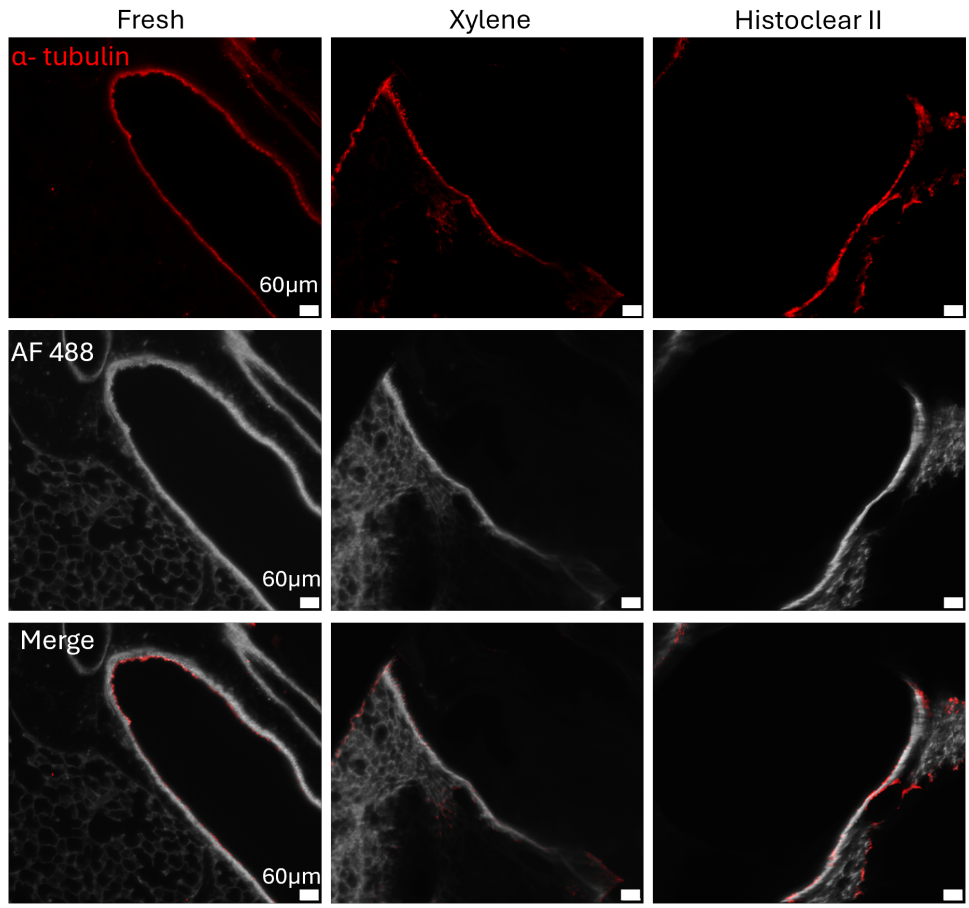

Figure 55. 3D rendering of fluorescently labeled PCLS. Airway ciliated cells are labeled with α-tubulin (red) and merged with autofluorescence images (gray,). Imaging was performed on the UltraMicroscope Blaze with the 1x and 4x objectives. All images were visualized and pseudocolored using Imaris software. Figure reproduced from (Gvazava et al. Manuscript)

Reverse optical clearing preserves chemical, protein and RNA composition for detection

Currently, tissues cleared using organic solvent based methods are often discarded after imaging with LSFM due to the fact that they are imaged in highly hydrophobic solutions for refractive index matching (RI matching). Ethyl cinnamate (ECi) is one of the most widely used RI matching solutions because it is compatible with many solvent-based clearing protocols and macroscope objectives, enables good tissue transparency with almost all tissues and is non-toxic. However, it is highly hydrophobic making downstream aqueous, water-based chemistries (e.g. immunofluorescent staining, in situ RNA hybridisation, etc.) impossible to perform. Therefore in paper III we aimed to develop an efficient and easy to implement ECi removal protocol that would enable subsequent molecular analysis, referred to here as reverse optical clearing (ROC). As we show in the paper III, we performed an initial screening of 7 solvents of reverse clearing candidate chemicals on tissue phantoms of 3% agarose and 5 mg/mL gelatin. We found that all solvents enable transitioning ECi containing phantoms into paraffin blocks which could be sectioned, stained and imaged.

Next, to extend the testing of ROC to native tissues, we utilized WT mouse lungs that were initially cleared and imaged using LSFM. Following LSFM imaging, individual lobes were dissected and subjected to ROC with different solvents similarly to tissue phantoms and subsequently paraffin embedded, sectioned and stained with standard histological techniques such as H&E and Masson's trichrome applied to both ROC and non-cleared controls. Furthermore, we established scoring criteria and asked three independent experts with more than five years of experience in lung histopathology to perform the scoring. Soring revealed that protic solvents (methanol, ethanol, and 2-propanol), which have a hydrogen atom bonded to a highly electronegative atom and therefore can donate protons, consistently outperformed aprotic ROC solvents, which do not have acidic hydrogens and cannot donate protons, in preserving histological architecture and staining quality. This suggests that, because aprotic solvents lack hydrogen-bond donating ability, they may be more reactive and therefore cause greater tissue damage during the incubation periods required for effective ECi removal. We further investigated the preservation of antigen–epitope integrity following ROC by performing immunohistochemical staining for common markers of the respiratory epithelium, including pro–surfactant protein C (pro-SPC) for alveolar type II cells and aquaporin 5 (AQP5) for alveolar type I cells, columnar epithelial cells, and submucosal gland acinar cells. While immunofluorescence signals for both AQP5 and Pro-SPC were detected in all samples the staining quality and predominant location of the staining varied according to the solvent used in the ROC protocol. Notably, samples which underwent ROC in ethanol and 2-propanol had IF staining patterns consistent with control while methanol-treated samples exhibited

nonspecific labelling of Pro-SPC staining within the airway epithelium, despite its expected restriction to type II pneumocytes. This observation is likely attributable to methanol-induced protein dehydration, which can disrupt tertiary structure and alter epitope accessibility. Such denaturation processes may expose linear epitopes that are normally concealed within the folded protein, thereby producing false-positive signals for Pro-SPC.

Further in paper III, to test for RNA integrity in tissue samples after ROC on mouse lung samples. We used in situ hybridization employing the RNAscope technology was performed as it allows quantification of individual RNA molecules (i.e. one dot is equivalent to one RNA molecule). Both control and ROC tissue was stained using three probes commonly used for quality control for RNA detection in tissues due to the fact that they are ubiquitously expressed and represent different levels of expression: *Ppib, Polr2a* and *Ubc* . For the negative control, probes complementary to bacterial RNA were used (*dapB*). We detected similar levels of RNA molecules per cell for the three positive control probes in both control and ROC tissue, as well as no significant staining in the negative control, indicating specific binding and detection. Thus, ROC using 2-propanol enables downstream analysis of both RNA and protein molecules in tissue sections from samples which were imaged with LSFM.

As the main goal of ROC is to take samples which have been imaged using LSFM and embed them in paraffin to enable downstream and complimentary analyses, the choice of solvent used in this process is critical. Considering the favorable solvent properties of 2-propanol, its excellent reverse clearing capacity without compromising tissue integrity and its compatibility with downstream paraffin embedding, we selected 2-propanol as the solvent for ROC.

To further understand the temporal kinetics of ECi removal from tissues using 2-propanol, we again used tissue phantoms comprised of agarose and gelatin and measured chemical composition using ATR-FTIR spectra to assess ECi removal (**Figure 56A**). Tissue phantoms which had been dehydrated and cleared in ECi exhibited prominent bands equivalent to ester C=O stretching (1707 cm^{-1}), C=C/aromatic modes (1636 cm^{-1}) and C–O stretching (1162 cm^{-1}) in comparison to samples dehydrated in 2-propanol. We used these peaks to assess ECi removal during ROC in 2-propanol and found that the intensities of these ECi–associated peaks declined over incubation time with 2-propanol, with a statistically significant reduction observed as soon as 1 h with respect to the ECi immersed tissue phantom controls, with further reductions after 2 h. After 3 h in 2-propanol, we observed minimal ECi-associated peaks and no statistically significant difference in comparison to tissue phantoms which were in 100% 2-propanol (**Figure 56 B,C**). Unsupervised principal component analysis (PCA) of the FTIR spectra in the fingerprint region further confirmed these findings and we were able to readily distinguish samples by solvent and time with 96% of the variance explained by PC1 and PC2. Tissue phantoms dehydrated and immersed in ECi clustered distinctly

from 100% 2-propanol immersed samples as expected. In line with our single peak analysis, the 1 h, 2 h, and 3 h reverse-cleared specimens progressed along the first two principal components and were highly similar to the 100% 2-propanol controls after 2-3 hours for all samples (**Figure 56D**). This trajectory indicates a progressive spectral convergence from ECi-dominated to 2-propanol-dominated profiles as reverse clearing proceeds

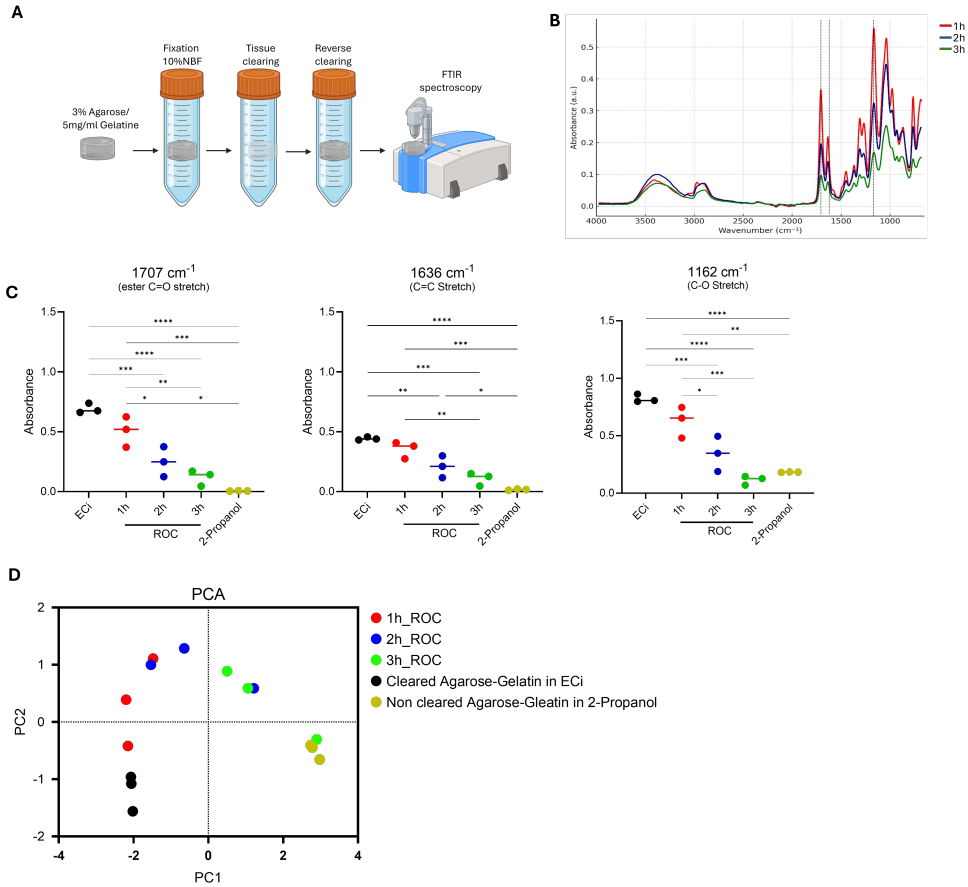

Figure 56. A) Experimental overview of agarose/gelatin disks ROC and FTIR measurements. B) FTIR spectra of agarose/gelatin gels during reverse clearing taking at 1, 2 and 3 hours (n=3). C) Main ECi peaks extracted from FTIR, corresponding to 1707 cm-1, 1636 cm-1, 1162 cm-1. Peaks show a significant decrease of ECi in the gels after 3h of ROC. Mean ± s.d. *p < 0.05 assessed by one-way ANOVA with Brown-Farsythe and Welch multiple comparisons test D) Principal component analysis (PCA) of FTIR spectra, showing gradual removal of ethyl cinnamate (ECi) during ROC. Figure reproduced from (Gvazava et al. Manuscript)

Multimodal imaging and spectroscopic analysis of mouse ROC-treated embryos is possible.

The previous work on reverse clearing was done in tissue phantom or lung samples and we aimed to extend our results to other tissues. To evaluate the impact of reverse clearing on different tissue integrity and biochemical composition, day 15 (E15.5) mouse embryos were analyzed. At this stage, major organs, including liver, lung, heart, kidneys and central nervous system, are established but remain developmentally immature, making them sensitive to experimental processing. Moreover, embryonic tissue is well suited for both LSFM and downstream evaluation, as intact embryos can be readily placed on standard microscopy slides.

Embryos were fixed overnight in 10% neutral buffered formalin (NBF) and bleached with 3% hydrogen peroxide to reduce pigmentation which we previously observed to be associated with high hematopoietic activity in the fetal liver at this developmental stage . Samples were then tissue cleared with PROTEUS and imaged with Blaze LSFM microscope (**Figure 57A**).

To assess the potential impact of ROC across mouse embryonic organs, whole embryos were processed either with the forward clearing and ROC protocol followed by paraffin embedding or directly paraffin-embedded after fixation (i.e. without clearing control). Maintenance of tissue types and general architecture after ROC was then assessed via hematoxylin and eosin (H&E) staining (**Figure 57B**). No differences were qualitatively identified between ROC and control tissues with respect to tissue architecture, nuclear detail (basophilia) or cytoplasmic eosinophilia. In addition, staining intensity and contrast were comparable and no clearing-related artefacts were observed. This indicated preserved morphology following ROC of developing mouse embryo and match our previous findings in adult murine lungs.

To assess potential biochemical alterations, ATR-FTIR spectroscopy was performed on paraffin embedded embryo sections. We were able to detect similar spectra at the bulk ATR-FTIR level between ROC and control tissues, with no evidence of residual ECi or 2-propanol in ROC samples (**Figure 57C**). For spatially resolved analysis, infrared quantum cascade laser (QCL)-based imaging was conducted on 10 μm sections mounted on CaF_2 substrates. Whole-section imaging demonstrated that PROTEUS processing is compatible with IR microspectroscopy and preserves the spatial distribution of key vibrational bands (~1656 cm^{-1}, amide I; ~1740 cm^{-1}, lipid ester C=O). Quantitative analysis of integrated absorbance at these bands revealed no significant differences between ROC and control groups.

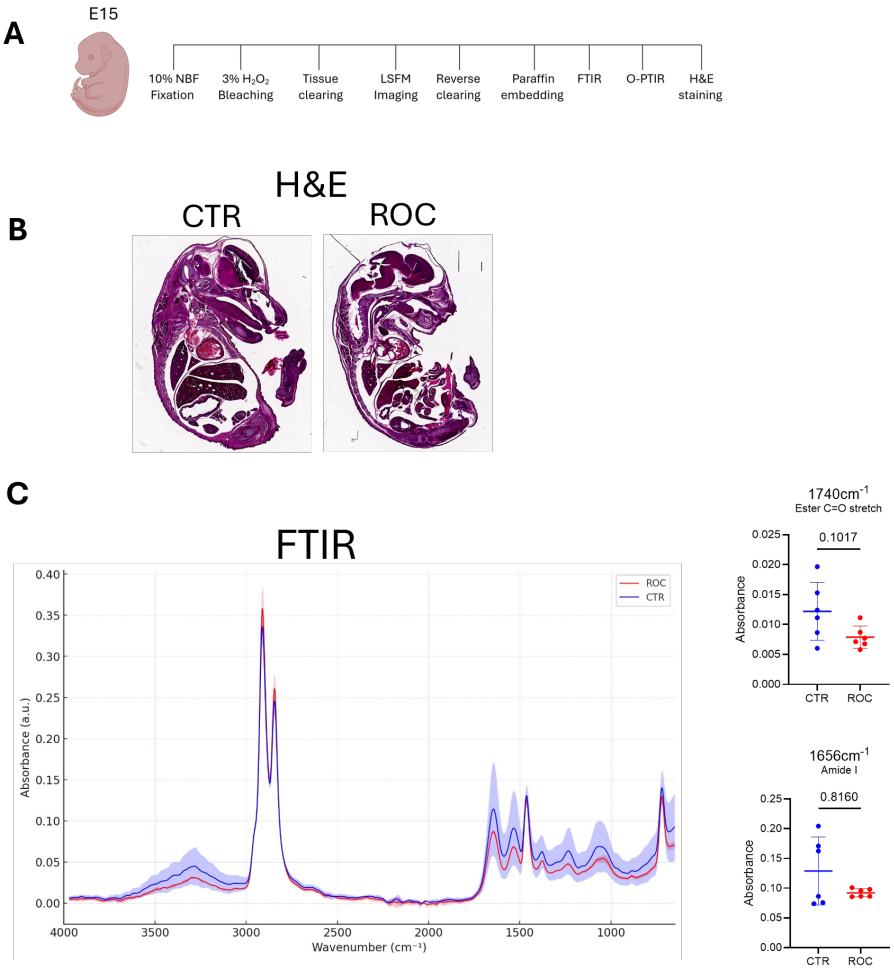

Figure 57. A) Experimental overview of multimodal tissue analysis of E15.5 mouse embryo. B) H&E-staining of paraffin section of a control (non-cleared) embryo compared with an embryo subjected to reverse optical clearing (ROC). C) FTIR full spectra analysis of 5µm paraffin sections (n = 6 technical replicates) from control and ROC embryos. 1740cm-1 (ester stretch) and 1656cm-1 (Amide I) peak extraction and quantification (n=6 technical replicates) . Mean ± s.d. *p < 0.05 assessed by Mann–Whitney U test. Figure reproduced from (Gvazava et al. Manuscript)

However, as discussed previously only IR-based techniques are inherently diffraction-limited, limiting their achievable spatial resolution. Therefore, to achieve sub-micron spatial resolution we employed OPTIR imaging (**Figure 58A**). Hyperspectral imaging of individual regions as well as single energy maps at 1656 cm^{-1} (corresponding to Amide I) showed no qualitative regional differences in IR spectra or signal intensity between ROC and control embryos in corresponding anatomical regions (**Figure58B**). However, we did note significant reductions in the

brain, lungs and skin after ROC. Interestingly, we observed a significant increase in ROC liver tissue in comparison to control, which might be attributed to removal of lipids in PROTEUS cleared tissues which increases the respective contribution of Amide I in OPTIR. Taken together, this indicates that ROC generally retains multiple classes of biological molecules and enables subsequent analysis at high spatial resolution.

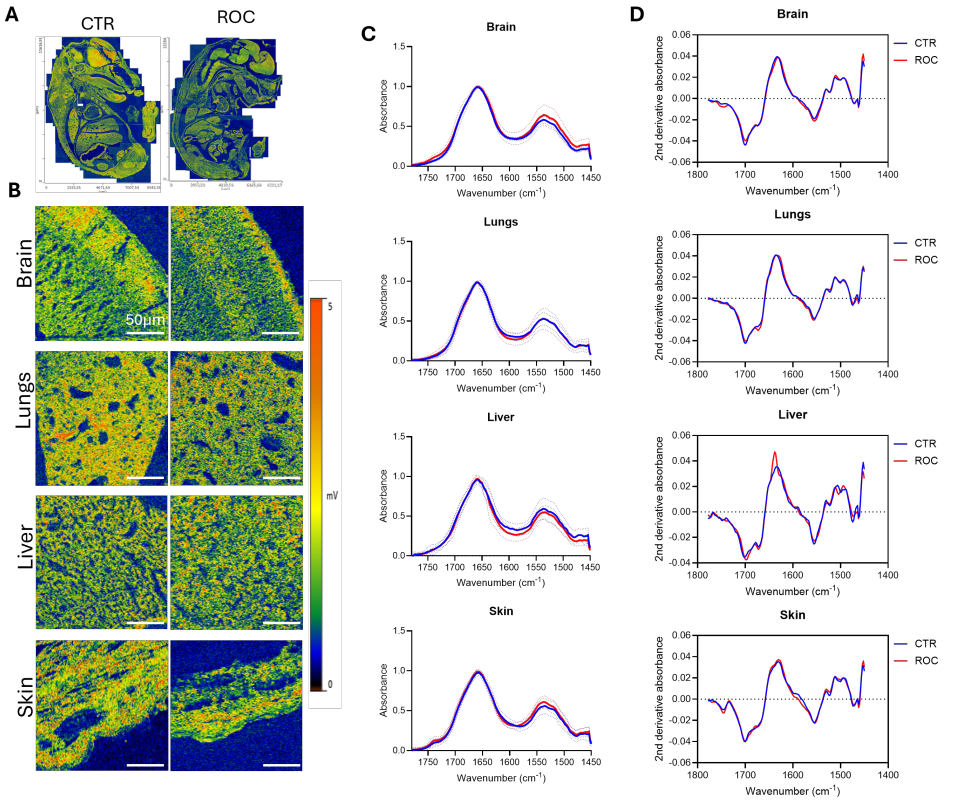

Figure 58. Images of control and ROC whole-embryo O-PTIR at single energy wave (1656 cm^{-1}, Amide 1). E) Representative organ-specific images of O-PTIR single energy wave at 1656 cm^{-1} (Amide 1) from E15.5 mouse embryo. Figure reproduced from (Gvazava et al. Manuscript)

Similar to our analysis of lung samples, we employed RNAscope to assess RNA integrity following ROC in E15.5 mouse embryos. In contrast to the relatively homogeneous structure of the lung, the mouse embryo contains multiple organs and tissue types. Therefore, it was important to evaluate whether RNA integrity was preserved across different embryonic organs. RNAscope signal was detected in all organs examined on the slide, indicating broad preservation of RNA after ROC. In paper III, we highlight the skin and liver as representative tissues. The skin, as the outermost layer of the embryo, is exposed to the solvents for a longer duration,

whereas the liver is located deeper within the embryo. RNAscope signal was observed in both tissues, indicating that RNA integrity was preserved in both superficial and deeper embryonic regions after ROC. Importantly, no obvious subjective differences in RNA detection were observed when compared with uncleared control tissue. This suggests that ROC does not visibly compromise RNA integrity, regardless of tissue depth or duration of exposure to the solvents.

Spatial omics have advanced in recent years to provide cellular and subcellular spatial resolution of RNA transcripts within tissue sections. The spatial context provided by these techniques has provided novel insights into understanding disease development, progression and tissue-level responses to treatment. However, one of the biggest limitations of spatial omics approaches is that they rely on thin tissue sections, omitting potentially valuable spatial information that could be located above or below the section extracted. While in situ RNA detection has been performed in whole-mount samples the number of transcripts detected is limited as of now due to the lasers and filters present in microscopes used for this type of analysis. We reasoned that optical clearing and volumetric imaging with LSFM, followed by ROC using PROTEUS and spatial transcriptomics could be a useful approach to help minimize this issue.

In situ imaging-based approaches such as merFISH utilize cyclical staining to label short RNA sequences during multiple hybridisation rounds to generate a binary barcode which can be subsequently decoded to enable identification of individual RNA molecules. Because merFISH does not rely on the use of individual probes assigned to each RNA molecules, this barcoding approach enables the simultaneous detection of hundreds of RNA molecules with subcellular resolution. Owing to the fact that our previous molecular analyses indicated that ROC using PROTEUS enabled detection of individual RNA molecules, we sought to determine whether spatial omics analyses could still be performed following ROC sample treatment. While ROC indicated retention of RNA molecules at comparable levels to control tissues, in situ imaging approaches require multiple hybridisation rounds. Suboptimal tissue processing or extensive exposure to solvents may make ROC tissue more susceptible to degradation during these multiple rounds of hybridisation.

To investigate this, two embryos, a control embryo directly embedded in paraffin and an ROC-treated E15.5 murine embryo, were subjected to a 900-gene panel covering major genes and transcription factors previously curated for organogenesis during murine embryonic development. While the embryos were tissue processed individually, they were placed onto a single Vizgen slide to ensure that we limited inter-slide/run effects between samples. Embryos were manually segmented for imaging using the DAPI channel within the imaging window. Standard analysis pipelines for quality control and cell segmentation were performed using the in-built Vizgen software for the ROC and control embryo sections. Cell clustering was subsequently performed using a combination of cluster level metrics and anatomical location. Qualitatively, and despite the anatomical cuts not being from identical

sagittal planes, the ROC and control embryo sections contained a similar number of cells for almost all clusters identified (**Figure 59**). However, and in line with our previous data there was a significant reduction in the median number of transcripts per cell in the ROC as compared to the control embryo indicating that the ROC procedure reduces the number of transcripts which can be detected at similar confidence levels. Despite this reduction in transcripts per cell, the markers distinguishing clusters were well conserved between conditions, indicating comparable coverage of the major markers used to determine the transcriptional landscape in the two sections.

At the whole embryo level, we identified 25 clusters which identified all major organs and tissue types expected to be present at this developmental stage (brain, cardiac, lung, olfactory, smooth muscle, skeletal muscle, liver, intestine skin, interstitial fibroblasts, hepatocytes, lymphoid cells, osteoblast precursors, etc). Comprable numbers of cells were detected for nearly all clusters, including clusters with a low number of cells (e.g. Lymphoid, Choroid Plexus Base Cells, and Adipocytes). While a global reduction in transcripts per cell was observed in nearly all clusters for the ROC sample, we noted that cluster 7 (erythroid) and cluster 21 (hepatocytes) had more cells within them as well as more transcripts per cell in the ROC as compared to control sections. These clusters anatomically corresponded to the liver which we had previously observed similar differences for in our OPTIR analysis. Therefore, we re-examined the raw images for presence of DAPI to determine if our sections, by chance, had different cell densities in them. Upon manual evaluation, we saw that the number of cells in the liver of the control tissue was comparable to that of the ROC liver but we subjectively noticed a lower signal to noise ratio in the control liver as compared to the ROC Altogether, PROTEUS enables in situ spatial transcriptomics following optical clearing, LSFM imaging and reverse-clearing; furthermore, it enables the detection of low-abundance transcripts as well as rare cellular populations.

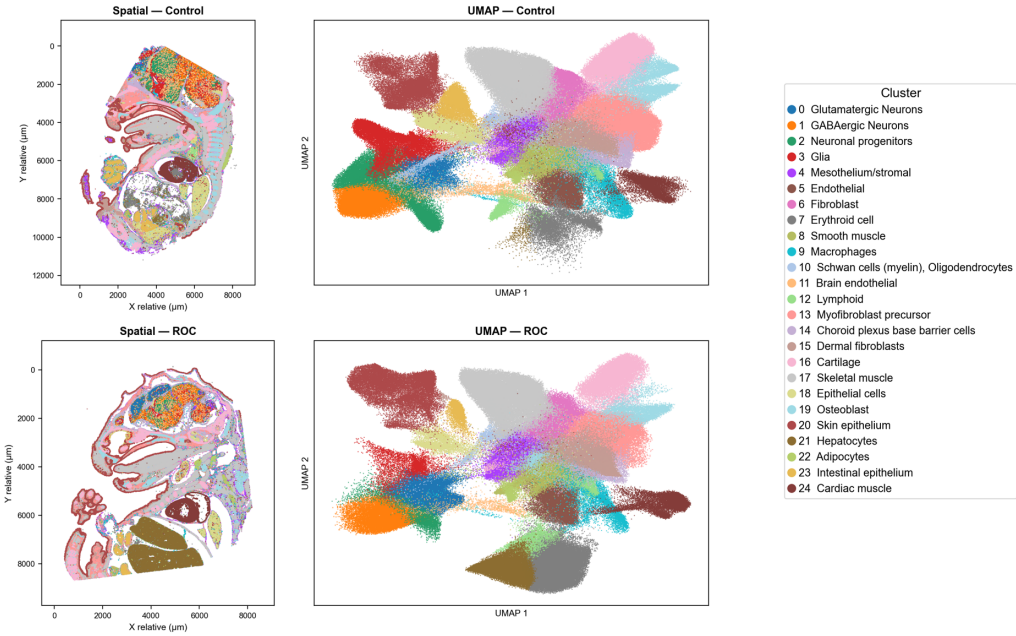

Figure 59. Spatial maps and corresponding in control and ROC embryos. Figure reproduced from (Gvazava et al. Manuscript)

Conclusions and Future perspectives

Multimodal tissue analysis is increasingly utilized in biomedical research to maximize the amount of data extracted from limited biological samples. In this doctoral thesis, spatiotemporal imaging of development, disease, and regeneration was investigated using advanced light-based techniques.

In **Paper I**, we demonstrated that O-PTIR spectra can be acquired from fully hydrated tissue biopsies using optimized laser parameters. Importantly, the tissue samples were not destroyed during imaging and could subsequently undergo standard histopathological examination. Furthermore, lipids were more readily detected in unprocessed, hydrated samples than in samples prepared using standard histological processing, where dehydration and delipidation reduce lipid-related signals.

We further show that O-PTIR can distinguish between normal and pathological tissue states in fully hydrated samples. In brain tissue, O-PTIR enabled discrimination between amyloid plaques and surrounding non-plaque tissue, supporting its potential for label-free identification of disease-associated biochemical changes. Further, we show fixation-induced alterations in protein secondary structure when comparing fresh and 4% PFA-fixed tissue. In particular, an increase in β-sheet content was observed following fixation, accompanied by a shift in the amide I band from 1630 to 1634 cm^{-1}, indicative of changes in protein organization.

The application of O-PTIR was then extended to *P.waltl* embryos, where we investigated whether photothermal imaging affected embryonic development. Our results demonstrated that embryonic development was not impaired following O-PTIR imaging, indicating that optimized imaging conditions are compatible with sensitive developmental models.

To further evaluate potential tissue damage caused by thermal expansion, we investigated two different organotypic tissue models. In acute brain slices, neuronal firing patterns were assessed using patch-clamp recordings after O-PTIR imaging. We did not observe impaired neuronal activity or increased Annexin V staining, indicating no clear induction of apoptosis under the applied imaging conditions. In PCLS, tissue viability and damage were assessed using live confocal imaging, with monitoring of cleaved caspase-3/7 activity and membrane integrity respectively with NucView488 and RedDot2 staining (**Figure 60**). Although increased cleaved

caspase-3/7 staining and LDH release were observed, particularly after 48 hours, ciliary beating was retained, suggesting preservation of functional tissue.

Taken together, the results obtained from P. waltl embryos, acute brain slices, and precision-cut lung slices indicate that O-PTIR induces minimal tissue damage when optimized imaging parameters are used, while preserving tissue morphology and functional properties. These findings support the broader application of O-PTIR as a non-destructive, label-free technique for chemical tissue imaging.

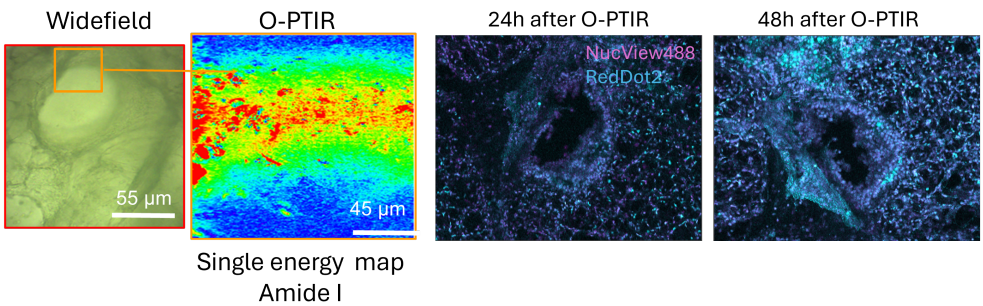

Figure 60. Bright-field image indicating airways subjected to O-PTIR hyperspectral imaging at 1656 cm–1, following the same spot by live confocal imaging represented maximum intensity projection (MIP) images of membrane damage (RedDot2) in cyan and Cleaved caspase 3/7 (NucView488) in magenta.

Overall, this work opens new possibilities for the use of O-PTIR in both research and clinical settings. In the future, O-PTIR may contribute to rapid diagnostic, for example during surgical decision-making, where distinguishing between normal and malignant tissue or defining resection margins is essential. Furthermore, the label-free and nondestructive nature of O-PTIR has potential applications in drug testing and pharmacological screening, where limited sample material and preservation of tissue viability are often major challenges. Another promising area is the analysis of advanced three-dimensional *in vitro* models, such as organoids, assembloids and organs-on-a-chip. These systems are increasingly used to model human development, disease, regeneration and treatment. However, their small size and limited sample availability make non-destructive and chemical imageability of O-PTIR especially useful. In addition, the compatibility of O-PTIR with hydrated samples may expand to bioengineering and characterization of biomaterials. For example, the technique could be used to evaluate cell–material interactions, extracellular matrix deposition, tissue integration, scaffold degradation, and biochemical remodeling in engineered constructs.

Taken together, this thesis demonstrates that O-PTIR is a promising, minimally invasive, label-free, nondestructive imaging technique with broad applicability across basic research, translational medicine, and future clinical diagnostics.

However, for O-PTIR microscopy live-sample imaging, further technical and methodological optimization will be required. While it can label-free molecular imaging of hydrated biological tissues, live imaging introduces additional considerations compared with fixed samples. As discussed above, viability of living cells and tissues depends on the maintenance of a stable and physiologically relevant microenvironment during image acquisition. Therefore, future O-PTIR systems intended for live imaging should incorporate essential live-microscopy features, including an environmental chamber, temperature control, CO_2 regulation, humidity stabilization and if needed controlled perfusion or medium exchange. Additionally, imaging parameters such as laser power, pulse duration, acquisition speed and total imaging time must be carefully optimized to ensure compatibility with living sample

In **Paper II**, we characterized the extent of membrane damage and caspase-3/7 activation immediately after vibratome sectioning of PCLS which is important for evaluating cell damage or death due to experimental perturbations (e.g. in Paper I or as exemplified in Paper II for screening RNA nanoparticles). To assess this, we used a confocal live imaging and staining setup combining RedDot2, a cell membrane-impermeant nuclear dye that labels cells with compromised plasma membrane integrity and NucView 488, a caspase-3/7-sensitive nuclear dye.

Immediately after vibratome sectioning, PCLS showed double positive staining of RedDot2 and NucView 488 nuclear signal, indicating that the slicing procedure induced acute membrane damage and caspase-3/7 activation. However, after 24 h of incubation or when slices were allowed to rest for 24 h before staining, both injury-associated signals were reduced. Moreover, NucView 488 staining significantly decreasing between day 1 and day 2 indicating a reduction in ongoing apoptosis simply due to *ex vivo* culture (**Figure 61**).

Based on these findings, we concluded that an initial resting period after vibratome sectioning is essential for PCLS experiments. Without such a resting period, injury caused by the sectioning procedure itself may act as a major confounding factor, particularly in studies evaluating cellular uptake, delivery efficiency, drug testing and toxicity. Therefore, compromised membrane integrity caused by slicing could alter both delivery efficiency or cellular responses independently of the treatment. More broadly, with the increasing use of organotypic tissue slices as translational *ex vivo* models, defining an appropriate experimental time window after vibratome sectioning is critical as vibratome-induced tissue damage can influence subsequent experiments related to cell viability, inflammation, permeability and treatment response/response. Establishing a standardized post-sectioning recovery period is therefore important to improve reproducibility, reduce technical artifacts and ensure

that observed experimental effects reflect the biological intervention rather than the mechanical trauma introduced during slice preparation.

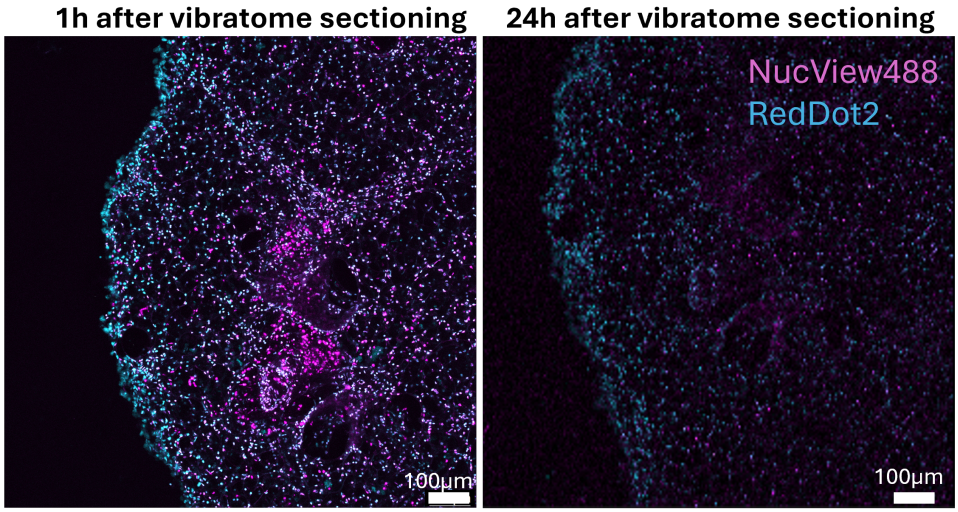

Figure 61. Maximum intensity projection (MIP) of live confocal imaging of PCLS stained immediately after sectioning and after 24 hours in culture.

To overcome limitations associated with solvent based tissue clearing methods, in Paper III, we developed a novel 2-propanol-based tissue clearing method, named PROTEUS. We found that compared to existing tissue clearing protocols, PROTEUS caused less shrinkage while also improving overall optical transparency. Further we observed a marked reduction in the UV-Vis absorbance peak at 415 nm with PROTEUS, which is associated with heme groups present in hemoglobin.

As mentioned above, a major practical limitation of the majority of solvent-based tissue clearing methods is loss of EFPs. PROTEUS preserved fluorescence under alkaline pH9 , low-temperature conditions of +4°C in experiments utilizing rGFP tissue phantoms as well as tdTomato signal in cleared brains for at least two months during storage in ECi at room temperature in the dark. Furthermore, tdTomato structures could still be observed for at least 63 days. This is particularly relevant given the known difficulty of preserving tdTomato during solvent-based clearing (196). Although quantitative signal decay was evident over time, the prolonged retention of usable fluorescence substantially expands experimental flexibility over current protocols by enabling delayed imaging, repeat acquisition on different instruments and sample transport without immediate loss of signal.

Many studies utilizing EFPs are biologically complex and combine endogenous fluorescence with fluorophore-based antibody labeling. In a xenotransplantation model containing eGFP-positive rat microvessels transplanted subcutaneously under the backs of murine animals, PROTEUS preserved EFPs and immunolabeled fluorescence while allowing visualization of fine vascular architecture due to its excellent optical clearing abilities. As the explanted tissue contained the skin and subcutaneous region, these findings indicate that the method is applicable to heterogeneous, pigmented and lipid-rich tissues in which optical scattering and fluorescence instability often compromise imaging quality. More broadly, this suggests that PROTEUS is compatible with multimodal labelling approaches within the same sample.

Improved transparency of PROTEUS was particularly evident in applications requiring visualization of highly dense, overlapping structures. In the mouse brain, we resolved vascular networks down to the single-capillary level and reconstructed in 3D. Similarly, in human cortical tissue, we were able to visualize intricate MBP-positive myelinated fibers together with NeuN-labeled neurons, despite the high myelin content and scattering properties of human brain tissue. Furthermore, we extended the PROTEUS tissue-clearing protocol to chick and mouse embryos at different developmental stages, as well as to human fetal tissues.

In addition to fresh tissues, for forward optical clearing, we also developed a protocol for paraffin removal from archived formalin-fixed paraffin-embedded (FFPE) samples. We show that FFPE samples can be deparaffinized, immunostained, cleared and imaged by LSFM, opening the door to three-dimensional analysis of stored clinical and experimental samples.

Further we established and show that reverse optical clearing (ROC) preserved tissue architecture, as well as protein epitopes and RNA integrity for sufficient downstream analyses using imaging based approaches. Further, ROC tissue was also compatible with label-free and highly sensitive infrared based chemical imaging and analysis, which demonstrates the gentle and highly-selective nature of chemical removal using PROTEUS. The compatibility of reverse-cleared samples with highly multiplexed approaches, such as in situ spatial transcriptomics, further highlights the potential of PROTEUS for multimodal tissue profiling. Using MERFISH in mouse embryos, we found that reverse-cleared samples supported transcript detection across major developmental cell populations and appeared to improve segmentation and transcript recovery in dense and optically challenging regions such as liver and heart.

In conclusion, this study establishes PROTEUS as a new 2-propanol-based forward and reverse tissue-clearing approach, for multimodal analysis on diverse tissues, organs and embryos (**Figure 62**).

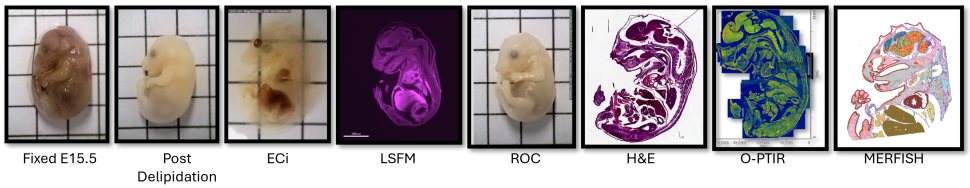

Figure 62. Images of E15.5 mouse embryo during different stages of forward clearing for LSFM imaging and reverse optical clearing (ROC) and following downstream multimodal imaging.

However, several important challenges remain to be addressed in future work in regard of PROTEUS tissue clearing. Although PROTEUS demonstrated compatibility with endogenous fluorescence preservation, further optimization is required to improve signal stability over extended storage time. This is particularly important because cleared tissues are commonly stored for prolonged durations in refractive index-matching media e.g. ethyl cinnamate. Since the tissue remains immersed in ethyl cinnamate after clearing, the long-term chemical environment may influence fluorescence protein stability and overall signal retention. Therefore, future studies should systematically evaluate the addition of protective compounds in reflective index-matching solutions, e.g. vitamin E or other antioxidant additives. Such additives may help reduce oxidative damage or fluorescence quenching and further improve the preservation of endogenous fluorescent proteins during long-term storage and repeated imaging.

Further, important direction concerns the safety and sustainability of solvent-based tissue clearing protocols. The majority of organic solvent-based clearing methods rely on dichloromethane (DCM), primarily because of its strong delipidating capacity. However, DCM is highly toxic, volatile and hazardous to handle, requiring strict safety precautions, appropriate ventilation and specialized waste management. Therefore, future work identifying and validating less hazardous alternatives to DCM are needed.

Further reconstructing and integrating acquired multimodal datasets in paper III back into the original 3D context remains a challenge. Especially when datasets are generated using different microscopes or analytical platforms, as differences in orientation, sectioning plane and tissue deformation complicate accurate spatial registration. Addressing these challenges will require more systematic computational strategies for cross-platform alignment. In this regard, recent advances in deep learning and artificial intelligence may offer powerful tools.

I would like to conclude my thesis with an Australian Aboriginal Proverb:

"We are all visitors to this time, this place. We are just passing through.
Our purpose here is to observe, to learn, to grow, to love…
and then we return home!"

References

1. West JB. Marcello Malpighi and the discovery of the pulmonary capillaries and alveoli. American Journal of Physiology-Lung Cellular and Molecular Physiology. 2013;304(6):L383-L90.
2. Perdicoyianni-Paleologou H. Xavier Bichat and the renovation of the pathological anatomy. J Med Biogr. 2024;32(1):89-96.
3. Neumann PE, Neumann EE. General histological woes: Definition and classification of tissues. Clin Anat. 2021;34(5):794-801.
4. Böhmer F. Zur pathologischen Anatomie der Meningitis cerebromedullaris epidemica. Ärztliches Intelligenzblatt. 1865;12:539-50.
5. Fischer E. Eosin als Tinctionsmittel für mikroskopische Präparate. Archiv für mikroskopische Anatomie. 1876;12(1):349-52.
6. Wissozky N. Ueber das Eosin als Reagens auf Hämoglobin und die Bildung von Blutgefässen und Blutkörperchen bei Säugethier-und Hühnerembryonen. Archiv für mikroskopische Anatomie. 1877;13(1):479-96.
7. Moore S, Seemayer TA, Tremblay G. The career and influence of Pierre Masson (1880-1959). Int J Surg Pathol. 2001;9(3):231-6.
8. Coons AH, Creech HJ, Jones RN. Immunological Properties of an Antibody Containing a Fluorescent Group.∗. Proceedings of the Society for Experimental Biology and Medicine. 1941;47(2):200-2.
9. Avrameas S, Uriel J. [Method of antigen and antibody labelling with enzymes and its immunodiffusion application]. C R Acad Hebd Seances Acad Sci D. 1966;262(24):2543-5.
10. Nakane PK. Simultaneous localization of multiple tissue antigens using the peroxidase-labeled antibody method: a study on pituitary glands of the rat. J Histochem Cytochem. 1968;16(9):557-60.
11. Nakane PK, Pierce GB, Jr. Enzyme-labeled antibodies for the light and electron microscopic localization of tissue antigens. J Cell Biol. 1967;33(2):307-18.
12. Ochs M. "And then I met Ewald Weibel". Am J Physiol Lung Cell Mol Physiol. 2020;319(3):L403-L7.
13. Shaw I, Gregory K. Acid-base balance: a review of normal physiology. BJA Educ. 2022;22(10):396-401.

14. Hopkins E, Sanvictores T, Sharma S. Physiology, Acid Base Balance. StatPearls. Treasure Island (FL)2026.
15. Alvarado A, Arce I. Metabolic Functions of the Lung, Disorders and Associated Pathologies. J Clin Med Res. 2016;8(10):689-700.
16. The lungs at the frontlines of immunity. Nat Immunol. 2015;16(1):17.
17. Rock JR, Hogan BL. Epithelial progenitor cells in lung development, maintenance, repair, and disease. Annu Rev Cell Dev Biol. 2011;27:493-512.
18. Shi T, Denney L, An H, Ho LP, Zheng Y. Alveolar and lung interstitial macrophages: Definitions, functions, and roles in lung fibrosis. J Leukoc Biol. 2021;110(1):107-14.
19. Guillot L, Nathan N, Tabary O, Thouvenin G, Le Rouzic P, Corvol H, et al. Alveolar epithelial cells: master regulators of lung homeostasis. Int J Biochem Cell Biol. 2013;45(11):2568-73.
20. Weibel ER. Morphometry of the human lung: the state of the art after two decades. Bull Eur Physiopathol Respir. 1979;15(5):999-1013.
21. Carlson BM. Chapter 11 - The Respiratory System. The Human Body: Academic Press; 2019. p. 303-19.
22. Travaglini KJ, Nabhan AN, Penland L, Sinha R, Gillich A, Sit RV, et al. A molecular cell atlas of the human lung from single-cell RNA sequencing. Nature. 2020;587(7835):619-25.
23. Drevet G, Conti M, Deslauriers J. Surgical anatomy of the tracheobronchial tree. J Thorac Dis. 2016;8(Suppl 2):S121-9.
24. Marieb EN, Hoehn K. Human Anatomy & Physiology: Pearson New International Edition: Pearson Education Limited; 2013.
25. Davis JD, Wypych TP. Correction: Cellular and functional heterogeneity of the airway epithelium. Mucosal Immunol. 2022;15(3):528.
26. Mercer RR, Russell ML, Roggli VL, Crapo JD. Cell number and distribution in human and rat airways. Am J Respir Cell Mol Biol. 1994;10(6):613-24.
27. Rock JR, Randell SH, Hogan BL. Airway basal stem cells: a perspective on their roles in epithelial homeostasis and remodeling. Dis Model Mech. 2010;3(9-10):545-56.
28. Hong KU, Reynolds SD, Watkins S, Fuchs E, Stripp BR. Basal cells are a multipotent progenitor capable of renewing the bronchial epithelium. Am J Pathol. 2004;164(2):577-88.
29. Rokicki W, Rokicki M, Wojtacha J, Dzeljijli A. The role and importance of club cells (Clara cells) in the pathogenesis of some respiratory diseases. Kardiochir Torakochirurgia Pol. 2016;13(1):26-30.
30. Rogers DF. Airway goblet cells: responsive and adaptable front-line defenders. Eur Respir J. 1994;7(9):1690-706.
31. Kuek LE, Lee RJ. First contact: the role of respiratory cilia in host-pathogen interactions in the airways. Am J Physiol Lung Cell Mol Physiol. 2020;319(4):L603-L19.

32. Ualiyeva S, Lemire E, Aviles EC, Wong C, Boyd AA, Lai J, et al. Tuft cell-produced cysteinyl leukotrienes and IL-25 synergistically initiate lung type 2 inflammation. Sci Immunol. 2021;6(66):eabj0474.
33. Noguchi M, Furukawa KT, Morimoto M. Pulmonary neuroendocrine cells: physiology, tissue homeostasis and disease. Dis Model Mech. 2020;13(12).
34. Luan X, Henao Romero N, Campanucci VA, Le Y, Mustofa J, Tam JS, et al. Pulmonary Ionocytes Regulate Airway Surface Liquid pH in Primary Human Bronchial Epithelial Cells. Am J Respir Crit Care Med. 2024;210(6):788-800.
35. Weibel ER. Chapter II - Organization of the Human Lung. Morphometry of the Human Lung: Academic Press; 1963. p. 4-9.
36. Weibel ER, Sapoval B, Filoche M. Design of peripheral airways for efficient gas exchange. Respir Physiol Neurobiol. 2005;148(1-2):3-21.
37. Ochs M, Nyengaard JR, Jung A, Knudsen L, Voigt M, Wahlers T, et al. The number of alveoli in the human lung. Am J Respir Crit Care Med. 2004;169(1):120-4.
38. Yang J, Hernandez BJ, Martinez Alanis D, Narvaez del Pilar O, Vila-Ellis L, Akiyama H, et al. The development and plasticity of alveolar type 1 cells. Development. 2016;143(1):54-65.
39. Kalina M, Mason RJ, Shannon JM. Surfactant protein C is expressed in alveolar type II cells but not in Clara cells of rat lung. Am J Respir Cell Mol Biol. 1992;6(6):594-600.
40. Adamson IY, Bowden DH. Derivation of type 1 epithelium from type 2 cells in the developing rat lung. Lab Invest. 1975;32(6):736-45.
41. Barkauskas CE, Cronce MJ, Rackley CR, Bowie EJ, Keene DR, Stripp BR, et al. Type 2 alveolar cells are stem cells in adult lung. J Clin Invest. 2013;123(7):3025-36.
42. Langleben D, Fox BD, Orfanos SE, Giovinazzo M, Catravas JD. Pulmonary capillary recruitment and distention in mammalian lungs: species similarities. Eur Respir Rev. 2022;31(163).
43. Trivedi A, Reed HO. The lymphatic vasculature in lung function and respiratory disease. Front Med (Lausanne). 2023;10:1118583.
44. Schraufnagel DE. Lung lymphatic anatomy and correlates. Pathophysiology. 2010;17(4):337-43.
45. Townsley MI. Structure and composition of pulmonary arteries, capillaries, and veins. Compr Physiol. 2012;2(1):675-709.
46. Burstiner L, Al Khalili Y. Anatomy, Thorax, Pleurae. StatPearls. Treasure Island (FL)2026.
47. Zocchi L. Physiology and pathophysiology of pleural fluid turnover. Eur Respir J. 2002;20(6):1545-58.
48. King TE, Pardo A, Selman M. Idiopathic pulmonary fibrosis. The Lancet. 2011;378(9807):1949-61.
49. Tanabe N, McDonough JE, Vasilescu DM, Ikezoe K, Verleden SE, Xu F, et al. Pathology of Idiopathic Pulmonary Fibrosis Assessed by a Combination of Microcomputed Tomography, Histology, and Immunohistochemistry. Am J Pathol. 2020;190(12):2427-35.

50. Raghu G, Remy-Jardin M, Myers JL, Richeldi L, Ryerson CJ, Lederer DJ, et al. Diagnosis of Idiopathic Pulmonary Fibrosis. An Official ATS/ERS/JRS/ALAT Clinical Practice Guideline. Am J Respir Crit Care Med. 2018;198(5):e44-e68.
51. Raghu G, Remy-Jardin M, Richeldi L, Thomson CC, Inoue Y, Johkoh T, et al. Idiopathic Pulmonary Fibrosis (an Update) and Progressive Pulmonary Fibrosis in Adults: An Official ATS/ERS/JRS/ALAT Clinical Practice Guideline. Am J Respir Crit Care Med. 2022;205(9):e18-e47.
52. Jiang P, Gil de Rubio R, Hrycaj SM, Gurczynski SJ, Riemondy KA, Moore BB, et al. Ineffectual Type 2-to-Type 1 Alveolar Epithelial Cell Differentiation in Idiopathic Pulmonary Fibrosis: Persistence of the KRT8(hi) Transitional State. Am J Respir Crit Care Med. 2020;201(11):1443-7.
53. Kathiriya JJ, Wang C, Zhou M, Brumwell A, Cassandras M, Le Saux CJ, et al. Human alveolar type 2 epithelium transdifferentiates into metaplastic KRT5+ basal cells. Nature Cell Biology. 2022;24(1):10-23.
54. Wagner DE, Alsafadi HN, Mitash N, Justet A, Hu Q, Pineda R, et al. Inhibition of epithelial cell YAP-TEAD/LOX signaling attenuates pulmonary fibrosis in preclinical models. Nat Commun. 2025;16(1):7099.
55. Adams TS, Schupp JC, Poli S, Ayaub EA, Neumark N, Ahangari F, et al. Single-cell RNA-seq reveals ectopic and aberrant lung-resident cell populations in idiopathic pulmonary fibrosis. Sci Adv. 2020;6(28):eaba1983.
56. Habermann AC, Gutierrez AJ, Bui LT, Yahn SL, Winters NI, Calvi CL, et al. Single-cell RNA sequencing reveals profibrotic roles of distinct epithelial and mesenchymal lineages in pulmonary fibrosis. Sci Adv. 2020;6(28):eaba1972.
57. Jun JI, Lau LF. The matricellular protein CCN1 induces fibroblast senescence and restricts fibrosis in cutaneous wound healing. Nat Cell Biol. 2010;12(7):676-85.
58. Willis BC, Liebler JM, Luby-Phelps K, Nicholson AG, Crandall ED, du Bois RM, et al. Induction of epithelial-mesenchymal transition in alveolar epithelial cells by transforming growth factor-beta1: potential role in idiopathic pulmonary fibrosis. Am J Pathol. 2005;166(5):1321-32.
59. Uhl FE, Vierkotten S, Wagner DE, Burgstaller G, Costa R, Koch I, et al. Preclinical validation and imaging of Wnt-induced repair in human 3D lung tissue cultures. Eur Respir J. 2015;46(4):1150-66.
60. Martin-Medina A, Lehmann M, Burgy O, Hermann S, Baarsma HA, Wagner DE, et al. Increased Extracellular Vesicles Mediate WNT5A Signaling in Idiopathic Pulmonary Fibrosis. Am J Respir Crit Care Med. 2018;198(12):1527-38.
61. Jaeger N, Gamini R, Cella M, Schettini JL, Bugatti M, Zhao S, et al. Single-cell analyses of Crohn's disease tissues reveal intestinal intraepithelial T cells heterogeneity and altered subset distributions. Nat Commun. 2021;12(1):1921.
62. Hippius H, Neundörfer G. The discovery of Alzheimer's disease. Dialogues Clin Neurosci. 2003;5(1):101-8.
63. Maurer K, Volk S, Gerbaldo H. Auguste D and Alzheimer's disease. Lancet. 1997;349(9064):1546-9.

64. Klementieva O, Willen K, Martinsson I, Israelsson B, Engdahl A, Cladera J, et al. Pre-plaque conformational changes in Alzheimer's disease-linked Abeta and APP. Nat Commun. 2017;8:14726.
65. Paulus A, Engdahl A, Yang Y, Boza-Serrano A, Bachiller S, Torres-Garcia L, et al. Amyloid Structural Changes Studied by Infrared Microspectroscopy in Bigenic Cellular Models of Alzheimer's Disease. Int J Mol Sci. 2021;22(7).
66. Klementieva O, Sandt C, Martinsson I, Kansiz M, Gouras GK, Borondics F. Super-Resolution Infrared Imaging of Polymorphic Amyloid Aggregates Directly in Neurons. Adv Sci (Weinh). 2020;7(6):1903004.
67. DeTure MA, Dickson DW. The neuropathological diagnosis of Alzheimer's disease. Mol Neurodegener. 2019;14(1):32.
68. Wang D, Munoz DG. Qualitative and quantitative differences in senile plaque dystrophic neurites of Alzheimer's disease and normal aged brain. J Neuropathol Exp Neurol. 1995;54(4):548-56.
69. Thal DR, Capetillo-Zarate E, Del Tredici K, Braak H. The development of amyloid beta protein deposits in the aged brain. Sci Aging Knowledge Environ. 2006;2006(6):re1.
70. Chen GF, Xu TH, Yan Y, Zhou YR, Jiang Y, Melcher K, et al. Amyloid beta: structure, biology and structure-based therapeutic development. Acta Pharmacol Sin. 2017;38(9):1205-35.
71. Kosik KS, Joachim CL, Selkoe DJ. Microtubule-associated protein tau (tau) is a major antigenic component of paired helical filaments in Alzheimer disease. Proc Natl Acad Sci U S A. 1986;83(11):4044-8.
72. Grundke-Iqbal I, Iqbal K, Quinlan M, Tung YC, Zaidi MS, Wisniewski HM. Microtubule-associated protein tau. A component of Alzheimer paired helical filaments. J Biol Chem. 1986;261(13):6084-9.
73. Moloney CM, Lowe VJ, Murray ME. Visualization of neurofibrillary tangle maturity in Alzheimer's disease: A clinicopathologic perspective for biomarker research. Alzheimers Dement. 2021;17(9):1554-74.
74. Hong X, Huang L, Lei F, Li T, Luo Y, Zeng M, et al. The Role and Pathogenesis of Tau Protein in Alzheimer's Disease. Biomolecules. 2025;15(6).
75. Medeiros R, Baglietto-Vargas D, LaFerla FM. The role of tau in Alzheimer's disease and related disorders. CNS Neurosci Ther. 2011;17(5):514-24.
76. Castellani RJ, Jamshidi P, Plascencia-Villa G, Perry G. The Amyloid Cascade Hypothesis: A Conclusion in Search of Support. Am J Pathol. 2025;195(11):1988-97.
77. Karran E, Mercken M, De Strooper B. The amyloid cascade hypothesis for Alzheimer's disease: an appraisal for the development of therapeutics. Nat Rev Drug Discov. 2011;10(9):698-712.
78. Crain SM. Development of “organotypic” bioelectric activities in central nervous tissues during maturation in culture. International review of neurobiology. 1966;9:1-43.

79. Carter M, Shieh J. Chapter 14 - Cell Culture Techniques. Guide to Research Techniques in Neuroscience (Second Edition). San Diego: Academic Press; 2015. p. 295-310.
80. Dionne KR, Tyler KL. Slice culture modeling of central nervous system (CNS) viral infection. Methods Mol Biol. 2013;1078:97-117.
81. Humpel C. Organotypic brain slice cultures: A review. Neuroscience. 2015;305:86-98.
82. Buskila Y, Breen PP, Tapson J, van Schaik A, Barton M, Morley JW. Extending the viability of acute brain slices. Scientific Reports. 2014;4(1):5309.
83. AlaylioĞlu M, Dursun E, Yilmazer S, Ak DG. A Bridge Between in vitro and in vivo Studies in Neuroscience: Organotypic Brain Slice Cultures. Noro Psikiyatr Ars. 2020;57(4):333-7.
84. Joseph K, Vasilikos I, Grauvogel J, Shah MJ, Reinacher PC, Nakagawa JM, et al. Human brain slice cultures: translational applications and ethical considerations. Life Science Alliance. 2025;8(12):e202403160.
85. Humpel C. Three-dimensional organotypic mouse brain slices to study Alzheimer's disease pathologies: a review. Frontiers in Dementia. 2025;Volume 4 - 2025.
86. Partiot E, Gorda B, Lutz W, Lebrun S, Khalfi P, Mora S, et al. Organotypic culture of human brain explants as a preclinical model for AI-driven antiviral studies. EMBO molecular medicine. 2024;16(4):1004.
87. Stegmayr J, Alsafadi HN, Langwiński W, Niroomand A, Lindstedt S, Leigh ND, et al. Isolation of high-yield and -quality RNA from human precision-cut lung slices for RNA-sequencing and computational integration with larger patient cohorts. Am J Physiol Lung Cell Mol Physiol. 2021;320(2):L232-l40.
88. Akram KM, Yates LL, Mongey R, Rothery S, Gaboriau DCA, Sanderson J, et al. Live imaging of alveologenesis in precision-cut lung slices reveals dynamic epithelial cell behaviour. Nat Commun. 2019;10(1):1178.
89. Cossar D, Bell J, Lang M, Hume R. Development of human fetal lung in organ culture compared with in utero ontogeny. In Vitro Cell Dev Biol Anim. 1993;29A(4):319-24.
90. Warburton D, Seth R, Shum L, Horcher PG, Hall FL, Werb Z, et al. Epigenetic role of epidermal growth factor expression and signalling in embryonic mouse lung morphogenesis. Dev Biol. 1992;149(1):123-33.
91. Geng Y, Li L, Dong Y, Liu X, Li XH, Ning W. Impaired elastin deposition in Fstl1-/- lung allograft under the renal capsule. PLoS One. 2013;8(11):e81368.
92. Del Moral PM, Warburton D. Explant culture of mouse embryonic whole lung, isolated epithelium, or mesenchyme under chemically defined conditions as a system to evaluate the molecular mechanism of branching morphogenesis and cellular differentiation. Methods Mol Biol. 2010;633:71-9.
93. Ballard PL, Gonzales LW, Williams MC, Roberts JM, Jacobs MM. Differentiation of type II cells during explant culture of human fetal lung is accelerated by endogenous prostanoids and adenosine 3',5'-monophosphate. Endocrinology. 1991;128(6):2916-24.

94. Sucre JMS, Vickers KC, Benjamin JT, Plosa EJ, Jetter CS, Cutrone A, et al. Hyperoxia Injury in the Developing Lung Is Mediated by Mesenchymal Expression of Wnt5A. Am J Respir Crit Care Med. 2020;201(10):1249-62.
95. Taglauer ES, Fernandez-Gonzalez A, Willis GR, Reis M, Yeung V, Liu X, et al. Antenatal Mesenchymal Stromal Cell Extracellular Vesicle Therapy Prevents Preeclamptic Lung Injury in Mice. Am J Respir Cell Mol Biol. 2022;66(1):86-95.
96. Gawlik KI, Bölükbas DA, Daoud F, Peruzzi N, Welinder E, Wendt TS, et al. Laminin γ1 chain is essential for the cardiorespiratory and muscular systems. Matrix Biology. 2025;141:47-66.
97. Alsafadi HN, Uhl FE, Pineda RH, Bailey KE, Rojas M, Wagner DE, et al. Applications and Approaches for Three-Dimensional Precision-Cut Lung Slices. Disease Modeling and Drug Discovery. Am J Respir Cell Mol Biol. 2020;62(6):681-91.
98. Rupaimoole R, Slack FJ. MicroRNA therapeutics: towards a new era for the management of cancer and other diseases. Nature reviews Drug discovery. 2017;16(3):203-22.
99. Ahangari F, Price NL, Malik S, Chioccioli M, Bärnthaler T, Adams TS, et al. microRNA-33 deficiency in macrophages enhances autophagy, improves mitochondrial homeostasis, and protects against lung fibrosis. JCI insight. 2023;8(4):e158100.
100. Chioccioli M, Roy S, Newell R, Pestano L, Dickinson B, Rigby K, et al. A lung targeted miR-29 mimic as a therapy for pulmonary fibrosis. EBioMedicine. 2022;85.
101. Aramesh K. History of attitudes toward death: a comparative study between Persian and western cultures. J Med Ethics Hist Med. 2016;9:20.
102. Virchow R. Die cellularpathologie: Primento Digital sprl; 2025.
103. Majno G, Joris I. Apoptosis, oncosis, and necrosis. An overview of cell death. Am J Pathol. 1995;146(1):3-15.
104. Reed JC. Dysregulation of apoptosis in cancer. Journal of clinical oncology. 1999;17(9):2941-.
105. Fuchs Y, Steller H. Programmed cell death in animal development and disease. Cell. 2011;147(4):742-58.
106. Lowe SW, Lin AW. Apoptosis in cancer. Carcinogenesis. 2000;21(3):485-95.
107. Kroemer G, Galluzzi L, Kepp O, Zitvogel L. Immunogenic cell death in cancer therapy. Annual review of immunology. 2013;31(1):51-72.
108. Kanduc D, Mittelman A, Serpico R, Sinigaglia E, Sinha AA, Natale C, et al. Cell death: apoptosis versus necrosis (review). Int J Oncol. 2002;21(1):165-70.
109. Galluzzi L, Vitale I, Aaronson SA, Abrams JM, Adam D, Agostinis P, et al. Molecular mechanisms of cell death: recommendations of the Nomenclature Committee on Cell Death 2018. Cell Death Differ. 2018;25(3):486-541.
110. Guicciardi ME, Leist M, Gores GJ. Lysosomes in cell death. Oncogene. 2004;23(16):2881-90.
111. Kroemer G, Levine B. Autophagic cell death: the story of a misnomer. Nat Rev Mol Cell Biol. 2008;9(12):1004-10.

112. Jangamreddy JR, Los MJ. Mitoptosis, a novel mitochondrial death mechanism leading predominantly to activation of autophagy. Hepat Mon. 2012;12(8):e6159.
113. Lee D, Kim IY, Saha S, Choi KS. Paraptosis in the anti-cancer arsenal of natural products. Pharmacol Ther. 2016;162:120-33.
114. Fang Y, Tian S, Pan Y, Li W, Wang Q, Tang Y, et al. Pyroptosis: A new frontier in cancer. Biomed Pharmacother. 2020;121:109595.
115. David KK, Andrabi SA, Dawson TM, Dawson VL. Parthanatos, a messenger of death. Front Biosci (Landmark Ed). 2009;14(3):1116-28.
116. Yipp BG, Kubes P. NETosis: how vital is it? Blood, The Journal of the American Society of Hematology. 2013;122(16):2784-94.
117. Linkermann A, Green DR. Necroptosis. New England Journal of Medicine. 2014;370(5):455-65.
118. Galluzzi L, Buque A, Kepp O, Zitvogel L, Kroemer G. Immunogenic cell death in cancer and infectious disease. Nat Rev Immunol. 2017;17(2):97-111.
119. Sun Q, Luo T, Ren Y, Florey O, Shirasawa S, Sasazuki T, et al. Competition between human cells by entosis. Cell Res. 2014;24(11):1299-310.
120. Maltese WA, Overmeyer JH. Methuosis: nonapoptotic cell death associated with vacuolization of macropinosome and endosome compartments. Am J Pathol. 2014;184(6):1630-42.
121. Li J, Cao F, Yin HL, Huang ZJ, Lin ZT, Mao N, et al. Ferroptosis: past, present and future. Cell Death Dis. 2020;11(2):88.
122. Liu Y, Shoji-Kawata S, Sumpter Jr RM, Wei Y, Ginet V, Zhang L, et al. Autosis is a Na+, K+-ATPase–regulated form of cell death triggered by autophagy-inducing peptides, starvation, and hypoxia–ischemia. Proceedings of the National Academy of Sciences. 2013;110(51):20364-71.
123. Liu J, Kuang F, Kang R, Tang D. Alkaliptosis: a new weapon for cancer therapy. Cancer Gene Ther. 2020;27(5):267-9.
124. Holze C, Michaudel C, Mackowiak C, Haas DA, Benda C, Hubel P, et al. Oxeiptosis, a ROS-induced caspase-independent apoptosis-like cell-death pathway. Nat Immunol. 2018;19(2):130-40.
125. Tang D, Chen X, Kroemer G. Cuproptosis: a copper-triggered modality of mitochondrial cell death. Cell Res. 2022;32(5):417-8.
126. Ciesielski HM, Nishida H, Takano T, Fukuhara A, Otani T, Ikegawa Y, et al. Erebosis, a new cell death mechanism during homeostatic turnover of gut enterocytes. PLoS Biol. 2022;20(4):e3001586.
127. Elmore S. Apoptosis: a review of programmed cell death. Toxicol Pathol. 2007;35(4):495-516.
128. Vitale I, Pietrocola F, Guilbaud E, Aaronson SA, Abrams JM, Adam D, et al. Apoptotic cell death in disease—Current understanding of the NCCD 2023. Cell Death & Differentiation. 2023;30(5):1097-154.
129. Hengartner MO. The biochemistry of apoptosis. Nature. 2000;407(6805):770-6.

130. Huang Z. The Chemical Biology of Apoptosis: Exploring Protein-Protein Interactions and the Life and Death of Cells with Small Molecules. Chemistry & Biology. 2002;9(10):1059-72.
131. Carneiro BA, El-Deiry WS. Targeting apoptosis in cancer therapy. Nat Rev Clin Oncol. 2020;17(7):395-417.
132. Adams JM, Cory S. Bcl-2-regulated apoptosis: mechanism and therapeutic potential. Curr Opin Immunol. 2007;19(5):488-96.
133. Vogelstein B, Kinzler KW. Cancer genes and the pathways they control. Nat Med. 2004;10(8):789-99.
134. Li J, Yuan J. Caspases in apoptosis and beyond. Oncogene. 2008;27(48):6194-206.
135. Jin L, Bao B, Huang XT, Tao JH, Duan JX, Zhong WJ, et al. MEOX1 triggers myofibroblast apoptosis resistance, contributing to pulmonary fibrosis in mice. J Cell Physiol. 2024;239(12):e31442.
136. Ju X, Wang K, Wang C, Zeng C, Wang Y, Yu J. Regulation of myofibroblast dedifferentiation in pulmonary fibrosis. Respir Res. 2024;25(1):284.
137. Korfei M, Ruppert C, Mahavadi P, Henneke I, Markart P, Koch M, et al. Epithelial endoplasmic reticulum stress and apoptosis in sporadic idiopathic pulmonary fibrosis. Am J Respir Crit Care Med. 2008;178(8):838-46.
138. Mahavadi P, Korfei M, Henneke I, Liebisch G, Schmitz G, Gochuico BR, et al. Epithelial stress and apoptosis underlie Hermansky-Pudlak syndrome-associated interstitial pneumonia. Am J Respir Crit Care Med. 2010;182(2):207-19.
139. Tang HL, Tang HM, Mak KH, Hu S, Wang SS, Wong KM, et al. Cell survival, DNA damage, and oncogenic transformation after a transient and reversible apoptotic response. Mol Biol Cell. 2012;23(12):2240-52.
140. Tang HM, Talbot CC, Jr., Fung MC, Tang HL. Transcriptomic study of anastasis for reversal of ethanol-induced apoptosis in mouse primary liver cells. Sci Data. 2022;9(1):418.
141. Roychoudhuri C, Creath K. The Nature of Light: What is a Photon? Proc SPIE. 2005;5866.
142. Piazza L, Lummen TTA, Quiñonez E, Murooka Y, Reed BW, Barwick B, et al. Simultaneous observation of the quantization and the interference pattern of a plasmonic near-field. Nature Communications. 2015;6(1):6407.
143. Li J-K, Sun K, Wang Y, Hao Z-Y, Liu Z-H, Zhou J, et al. Experimental demonstration of separating the wave–particle duality of a single photon with the quantum Cheshire cat. Light: Science & Applications. 2023;12(1):18.
144. Gest H. The discovery of microorganisms by Robert Hooke and Antoni Van Leeuwenhoek, fellows of the Royal Society. Notes Rec R Soc Lond. 2004;58(2):187-201.
145. Wollman AJ, Nudd R, Hedlund EG, Leake MC. From Animaculum to single molecules: 300 years of the light microscope. Open Biol. 2015;5(4):150019.
146. Rochow TG, Tucker PA. A Brief History of Microscopy. In: Rochow TG, Tucker PA, editors. Introduction to Microscopy by Means of Light, Electrons, X Rays, or Acoustics. Boston, MA: Springer US; 1994. p. 1-21.

147. Shribak M, Inoué S. Orientation-independent differential interference contrast microscopy. Collected Works of Shinya Inoué. p. 953-62.
148. Gao G, Jiang Y-W, Sun W, Wu F-G. Fluorescent quantum dots for microbial imaging. Chinese Chemical Letters. 2018;29(10):1475-85.
149. Chalfie M, Tu Y, Euskirchen G, Ward WW, Prasher DC. Green Fluorescent Protein as a Marker for Gene Expression. Science. 1994;263(5148):802-5.
150. Miller DM, Shakes DC. Chapter 16 Immunofluorescence Microscopy. In: Epstein HF, Shakes DC, editors. Methods in Cell Biology. 48: Academic Press; 1995. p. 365-94.
151. Shashkova S, Leake MC. Single-molecule fluorescence microscopy review: shedding new light on old problems. Biosci Rep. 2017;37(4).
152. Stokes GG. XXX. On the change of refrangibility of light. Philosophical Transactions of the Royal Society of London. 1852(142):463-562.
153. Albani JR. Structure and Dynamics of Macromolecules: Absorption and Fluorescence Studies: Elsevier Science; 2011.
154. Santos EM, Sheng W, Esmatpour Salmani R, Tahmasebi Nick S, Ghanbarpour A, Gholami H, et al. Design of Large Stokes Shift Fluorescent Proteins Based on Excited State Proton Transfer of an Engineered Photobase. Journal of the American Chemical Society. 2021;143(37):15091-102.
155. Eggeling C, Widengren J, Rigler R, Seidel CAM. Photobleaching of Fluorescent Dyes under Conditions Used for Single-Molecule Detection: Evidence of Two-Step Photolysis. Analytical Chemistry. 1998;70(13):2651-9.
156. Wustner D, Christensen T, Solanko LM, Sage D. Photobleaching kinetics and time-integrated emission of fluorescent probes in cellular membranes. Molecules. 2014;19(8):11096-130.
157. Laissue PP, Alghamdi RA, Tomancak P, Reynaud EG, Shroff H. Assessing phototoxicity in live fluorescence imaging. Nat Methods. 2017;14(7):657-61.
158. Combs CA. Fluorescence microscopy: a concise guide to current imaging methods. Curr Protoc Neurosci. 2010;Chapter 2:Unit2.1.
159. Mayerich D, Sun R. Chapter Twelve - Superresolution Image Processing. In: Merchant FA, Castleman KR, editors. Microscope Image Processing (Second Edition): Academic Press; 2023. p. 319-34.
160. Born M, Wolf E. Principles of optics: electromagnetic theory of propagation, interference and diffraction of light: Elsevier; 2013.
161. Beyond the diffraction limit. Nature Photonics. 2009;3(7):361-.
162. Pohl DW, Denk W, Lanz M. Optical stethoscopy: Image recording with resolution λ/20. Applied Physics Letters. 1984;44(7):651-3.
163. Swaminathan S. GFP: the green revolution. Nature Cell Biology. 2009;11(1):S20-S.
164. Shimomura O, Johnson FH, Saiga Y. Extraction, purification and properties of aequorin, a bioluminescent protein from the luminous hydromedusan, Aequorea. J Cell Comp Physiol. 1962;59:223-39.
165. Chalfie M, Tu Y, Euskirchen G, Ward WW, Prasher DC. Green fluorescent protein as a marker for gene expression. Science. 1994;263(5148):802-5.

166. Heim R, Prasher DC, Tsien RY. Wavelength mutations and posttranslational autoxidation of green fluorescent protein. Proc Natl Acad Sci U S A. 1994;91(26):12501-4.
167. Goedhart J, von Stetten D, Noirclerc-Savoye M, Lelimousin M, Joosen L, Hink MA, et al. Structure-guided evolution of cyan fluorescent proteins towards a quantum yield of 93%. Nat Commun. 2012;3:751.
168. Heim R, Cubitt AB, Tsien RY. Improved green fluorescence. Nature. 1995;373(6516):663-4.
169. Dietrich C, Maiss E. Red fluorescent protein DsRed from Discosoma sp. as a reporter protein in higher plants. Biotechniques. 2002;32(2):286, 8-90, 92-3.
170. Shaner NC, Lambert GG, Chammas A, Ni Y, Cranfill PJ, Baird MA, et al. A bright monomeric green fluorescent protein derived from Branchiostoma lanceolatum. Nat Methods. 2013;10(5):407-9.
171. Paddock SW, Eliceiri KW. Laser scanning confocal microscopy: history, applications, and related optical sectioning techniques. Methods Mol Biol. 2014;1075:9-47.
172. Jonkman J, Brown CM, Wright GD, Anderson KI, North AJ. Tutorial: guidance for quantitative confocal microscopy. Nature Protocols. 2020;15(5):1585-611.
173. Masters BR. Richard Zsigmondy and Henry Siedentopf's Ultramicroscope. In: Masters BR, editor. Superresolution Optical Microscopy: The Quest for Enhanced Resolution and Contrast. Cham: Springer International Publishing; 2020. p. 165-72.
174. Voie AH, Burns DH, Spelman FA. Orthogonal-plane fluorescence optical sectioning: three-dimensional imaging of macroscopic biological specimens. J Microsc. 1993;170(Pt 3):229-36.
175. Huisken J, Swoger J, Del Bene F, Wittbrodt J, Stelzer EHK. Optical Sectioning Deep Inside Live Embryos by Selective Plane Illumination Microscopy. Science. 2004;305(5686):1007-9.
176. Sykora D, Jindrich J, Kral V, Jakubek M, Tatar A, Kejik Z, et al. Formaldehyde Reacts with Amino Acids and Peptides with a Potential Role in Acute Methanol Intoxication. J Anal Toxicol. 2020;44(8):880-5.
177. Kiernan JA. Formaldehyde, Formalin, Paraformaldehyde And Glutaraldehyde: What They Are And What They Do. Microscopy Today. 2000;8(1):8-13.
178. Sabatini DD, Bensch K, Barrnett RJ. Cytochemistry and electron microscopy. The preservation of cellular ultrastructure and enzymatic activity by aldehyde fixation. J Cell Biol. 1963;17(1):19-58.
179. Smith JE, Reese TS. Use of aldehyde fixatives to determine the rate of synaptic transmitter release. J Exp Biol. 1980;89:19-29.
180. Howat WJ, Wilson BA. Tissue fixation and the effect of molecular fixatives on downstream staining procedures. Methods. 2014;70(1):12-9.
181. Hewlett BR. Penetration Rates of Formaldehyde. Microscopy Today. 2002;10(6):30-1.

182. Da Silva IA, Gvazava N, Putra Wendi I, Guinea R, García Giménez F, Stegmayr J, et al. Formalin-free fixation and xylene-free tissue processing preserves cell-hydrogel interactions for histological evaluation of 3D calcium alginate tissue engineered constructs. Frontiers in Biomaterials Science. 2023;Volume 2 - 2023.
183. Hobro AJ, Smith NI. An evaluation of fixation methods: Spatial and compositional cellular changes observed by Raman imaging. Vibrational Spectroscopy. 2017;91:31-45.
184. Chen Y, Zou X, Wang L, Gao Y, Fu H, Liu B, et al. Systematic comparison of the effects of various fixatives on the stability of the cellular proteome. Journal of Proteomics. 2026;323:105567.
185. Aziz SJ, Zeman-Pocrnich CE. Tissue Processing. Methods Mol Biol. 2022;2422:47-63.
186. Richardson DS, Lichtman JW. Clarifying Tissue Clearing. Cell. 2015;162(2):246-57.
187. Richardson DS, Guan W, Matsumoto K, Pan C, Chung K, Ertürk A, et al. TISSUE CLEARING. Nat Rev Methods Primers. 2021;1(1).
188. Tian T, Yang Z, Li X. Tissue clearing technique: Recent progress and biomedical applications. J Anat. 2021;238(2):489-507.
189. Spalteholz W. Über das Durchsichtigmachen von menschlichen und tierischen Präparaten und seine theoretischen Bedingungen, nebst Anhang: Über Knochenfärbung: S. Hirzel; 1914.
190. Steinke H, Wolff W. A modified Spalteholz technique with preservation of the histology. Ann Anat. 2001;183(1):91-5.
191. Acar M, Kocherlakota KS, Murphy MM, Peyer JG, Oguro H, Inra CN, et al. Deep imaging of bone marrow shows non-dividing stem cells are mainly perisinusoidal. Nature. 2015;526(7571):126-30.
192. Rong Z, Mai H, Ebert G, Kapoor S, Puelles VG, Czogalla J, et al. Persistence of spike protein at the skull-meninges-brain axis may contribute to the neurological sequelae of COVID-19. Cell Host Microbe. 2024;32(12):2112-30 e10.
193. Ou Z, Duh Y-S, Rommelfanger NJ, Keck CHC, Jiang S, Brinson K, et al. Achieving optical transparency in live animals with absorbing molecules. Science. 2024;385(6713):eadm6869.
194. Inagaki S, Nakagawa-Tamagawa N, Huynh NZ, Kambe Y, Yagasaki R, Manita S, et al. Isotonic and minimally invasive optical clearing media for live cell imaging ex vivo and in vivo. Nature Methods. 2026;23(4):839-53.
195. Renier N, Wu Z, Simon DJ, Yang J, Ariel P, Tessier-Lavigne M. iDISCO: a simple, rapid method to immunolabel large tissue samples for volume imaging. Cell. 2014;159(4):896-910.
196. Qi Y, Yu T, Xu J, Wan P, Ma Y, Zhu J, et al. FDISCO: Advanced solvent-based clearing method for imaging whole organs. Sci Adv. 2019;5(1):eaau8355.
197. Pan C, Cai R, Quacquarelli FP, Ghasemigharagoz A, Lourbopoulos A, Matryba P, et al. Shrinkage-mediated imaging of entire organs and organisms using uDISCO. Nat Methods. 2016;13(10):859-67.

198. Dent JA, Polson AG, Klymkowsky MW. A whole-mount immunocytochemical analysis of the expression of the intermediate filament protein vimentin in Xenopus. Development. 1989;105(1):61-74.
199. Erturk A, Becker K, Jahrling N, Mauch CP, Hojer CD, Egen JG, et al. Three-dimensional imaging of solvent-cleared organs using 3DISCO. Nat Protoc. 2012;7(11):1983-95.
200. Habart M, Lio G, Soumier A, Demily C, Sirigu A. An optimized iDISCO+ protocol for tissue clearing and 3D analysis of oxytocin and vasopressin cell network in the developing mouse brain. STAR Protoc. 2023;4(1):101968.
201. Li Y, Xu J, Wan P, Yu T, Zhu D. Optimization of GFP Fluorescence Preservation by a Modified uDISCO Clearing Protocol. Front Neuroanat. 2018;12:67.
202. Pechtimaldjian L, Cario M, Teillon J, Marais S, Dupichaud S, Rezvani HR, et al. Skin-iDISCO(+): An optimized tissue-clearing and labeling protocol for morphometric analysis of human cutaneous vasculature. STAR Protoc. 2025;6(1):103524.
203. Cai R, Kolabas ZI, Pan C, Mai H, Zhao S, Kaltenecker D, et al. Whole-mouse clearing and imaging at the cellular level with vDISCO. Nat Protoc. 2023;18(4):1197-242.
204. Klingberg A, Hasenberg A, Ludwig-Portugall I, Medyukhina A, Mann L, Brenzel A, et al. Fully Automated Evaluation of Total Glomerular Number and Capillary Tuft Size in Nephritic Kidneys Using Lightsheet Microscopy. J Am Soc Nephrol. 2017;28(2):452-9.
205. Masselink W, Reumann D, Murawala P, Pasierbek P, Taniguchi Y, Bonnay F, et al. Broad applicability of a streamlined ethyl cinnamate-based clearing procedure. Development. 2019;146(3).
206. Jing D, Zhang S, Luo W, Gao X, Men Y, Ma C, et al. Author Correction: Tissue clearing of both hard and soft tissue organs with the PEGASOS method. Cell Res. 2019;29(6):506.
207. Mai H, Rong Z, Zhao S, Cai R, Steinke H, Bechmann I, et al. Scalable tissue labeling and clearing of intact human organs. Nat Protoc. 2022;17(10):2188-215.
208. Li W. Encyclopedia of Life Sciences (ELS). (No Title). 2008.
209. Pandi Chelvam S, Ng AJY, Huang J, Lee E, Baranski M, Yong D, et al. Machine learning aided UV absorbance spectroscopy for microbial contamination in cell therapy products. Scientific Reports. 2025;15(1):7631.
210. Perera AGU. Editorial for the Special Issue on Semiconductor Infrared Devices and Applications. Micromachines (Basel). 2021;12(9).
211. Fundamentals of Infrared Thermal Imaging. Infrared Thermal Imaging2017. p. 1-106.
212. Barth A. Infrared spectroscopy of proteins. Biochimica et Biophysica Acta (BBA) - Bioenergetics. 2007;1767(9):1073-101.
213. Suryadevara V, Nazeer SS, Sreedhar H, Adelaja O, Kajdacsy-Balla A, Natarajan V, et al. Infrared spectral microscopy as a tool to monitor lung fibrosis development in a model system. Biomed Opt Express. 2020;11(7):3996-4007.

214. Miller LM, Bourassa MW, Smith RJ. FTIR spectroscopic imaging of protein aggregation in living cells. Biochim Biophys Acta. 2013;1828(10):2339-46.
215. Zhang D, Li C, Zhang C, Slipchenko MN, Eakins G, Cheng JX. Depth-resolved mid-infrared photothermal imaging of living cells and organisms with submicrometer spatial resolution. Sci Adv. 2016;2(9):e1600521.
216. Prater CB, Kansiz M, Cheng JX. A tutorial on optical photothermal infrared (O-PTIR) microscopy. APL Photonics. 2024;9(9):091101.
217. Bai Y, Yin J, Cheng J-X. Bond-selective imaging by optically sensing the mid-infrared photothermal effect. Science Advances. 2021;7(20):eabg1559.
218. Xia Q, Yin J, Guo Z, Cheng JX. Mid-Infrared Photothermal Microscopy: Principle, Instrumentation, and Applications. J Phys Chem B. 2022;126(43):8597-613.
219. Spadea A, Denbigh J, Lawrence MJ, Kansiz M, Gardner P. Analysis of fixed and live single cells using optical photothermal infrared with concomitant Raman spectroscopy. Analytical chemistry. 2021;93(8):3938-50.
220. DeFalco J, Tomishima M, Liu H, Zhao C, Cai X, Marth JD, et al. Virus-assisted mapping of neural inputs to a feeding center in the hypothalamus. Science. 2001;291(5513):2608-13.
221. Madisen L, Zwingman TA, Sunkin SM, Oh SW, Zariwala HA, Gu H, et al. A robust and high-throughput Cre reporting and characterization system for the whole mouse brain. Nat Neurosci. 2010;13(1):133-40.
222. Sun X, Aghazadeh Y, Nunes SS. Isolation of ready-made rat microvessels and its applications in effective in vivo vascularization and in angiogenic studies in vitro. Nat Protoc. 2022;17(12):2721-38.
223. Aghazadeh Y, Poon F, Sarangi F, Wong FTM, Khan ST, Sun X, et al. Microvessels support engraftment and functionality of human islets and hESC-derived pancreatic progenitors in diabetes models. Cell Stem Cell. 2021;28(11):1936-49 e8.
224. Gvazava N, Wagner D. Visualization of cellular membrane damage and apoptosis in murine precision cut lung slices after vibratome slicing. 2024.
225. Stone KC, Mercer RR, Gehr P, Stockstill B, Crapo JD. Allometric relationships of cell numbers and size in the mammalian lung. American journal of respiratory cell and molecular biology. 1992;6(2):235-43.
226. Berridge MV, Herst PM, Tan AS. Tetrazolium dyes as tools in cell biology: new insights into their cellular reduction. Biotechnology annual review. 2005;11:127-52.
227. Alsafadi HN, Staab-Weijnitz CA, Lehmann M, Lindner M, Peschel B, Königshoff M, et al. An ex vivo model to induce early fibrosis-like changes in human precision-cut lung slices. American Journal of Physiology-Lung Cellular and Molecular Physiology. 2017;312(6):L896-L902.
228. Farhana A, Lappin SL. Biochemistry, Lactate Dehydrogenase. StatPearls. Treasure Island (FL)2026.
229. Benseny-Cases N, Klementieva O, Cotte M, Ferrer I, Cladera J. Microspectroscopy (μFTIR) reveals co-localization of lipid oxidation and amyloid plaques in human Alzheimer disease brains. Analytical Chemistry. 2014;86(24):12047-54.

230. Le Naour F, Bralet M-P, Debois D, Sandt C, Guettier C, Dumas P, et al. Chemical imaging on liver steatosis using synchrotron infrared and ToF-SIMS microspectroscopies. PLoS One. 2009;4(10):e7408.
231. Orphanou C-M. The detection and discrimination of human body fluids using ATR FT-IR spectroscopy. Forensic science international. 2015;252:e10-e6.
232. Sasaguri H, Nilsson P, Hashimoto S, Nagata K, Saito T, De Strooper B, et al. APP mouse models for Alzheimer's disease preclinical studies. Embo j. 2017;36(17):2473-87.
233. Klementieva O, Willén K, Martinsson I, Israelsson B, Engdahl A, Cladera J, et al. Pre-plaque conformational changes in Alzheimer's disease-linked Aβ and APP. Nature communications. 2017;8(1):14726.
234. Koike BDV, Farias KS, Billwiller F, Almeida-Filho D, Libourel PA, Tiran-Cappello A, et al. Electrophysiological Evidence That the Retrosplenial Cortex Displays a Strong and Specific Activation Phased with Hippocampal Theta during Paradoxical (REM) Sleep. J Neurosci. 2017;37(33):8003-13.
235. Logue SE, Elgendy M, Martin SJ. Expression, purification and use of recombinant annexin V for the detection of apoptotic cells. Nat Protoc. 2009;4(9):1383-95.
236. Wilkens R, Hoffrichter A, Kleinsimlinghaus K, Bohl B, Haag C, Lehmann N, et al. Diverse maturity-dependent and complementary anti-apoptotic brakes safeguard human iPSC-derived neurons from cell death. Cell Death Dis. 2022;13(10):887.
237. Annis RP, Swahari V, Nakamura A, Xie AX, Hammond SM, Deshmukh M. Mature neurons dynamically restrict apoptosis via redundant premitochondrial brakes. Febs j. 2016;283(24):4569-82.
238. Shi D, Boucaut J. The chronological development of the urodele amphibian Pleurodeles waltl (Michah). Int J Dev Biol. 1995;39(3):427-41.
239. Azeez OI, Meintjes R, Chamunorwa JP. Fat body, fat pad and adipose tissues in invertebrates and vertebrates: the nexus. Lipids Health Dis. 2014;13:71.
240. Uhl FE, Vierkotten S, Wagner DE, Burgstaller G, Costa R, Koch I, et al. Preclinical validation and imaging of Wnt-induced repair in human 3D lung tissue cultures. European Respiratory Journal. 2015;46(4):1150-66.
241. Stone KC, Mercer RR, Gehr P, Stockstill B, Crapo JD. Allometric relationships of cell numbers and size in the mammalian lung. Am J Respir Cell Mol Biol. 1992;6(2):235-43.
242. Matsumoto K, Mitani TT, Horiguchi SA, Kaneshiro J, Murakami TC, Mano T, et al. Advanced CUBIC tissue clearing for whole-organ cell profiling. Nat Protoc. 2019;14(12):3506-37.
243. Park YG, Sohn CH, Chen R, McCue M, Yun DH, Drummond GT, et al. Protection of tissue physicochemical properties using polyfunctional crosslinkers. Nat Biotechnol. 2018.
244. Tomer R, Ye L, Hsueh B, Deisseroth K. Advanced CLARITY for rapid and high-resolution imaging of intact tissues. Nat Protoc. 2014;9(7):1682-97.
245. Ke MT, Fujimoto S, Imai T. SeeDB: a simple and morphology-preserving optical clearing agent for neuronal circuit reconstruction. Nat Neurosci. 2013;16(8):1154-61.

246. Alnuami AA, Zeedi B, Qadri SM, Ashraf SS. Oxyradical-induced GFP damage and loss of fluorescence. Int J Biol Macromol. 2008;43(2):182-6.
247. Werle J, Dunovska K, Podhajsky J, Cerny M, Cepova J, Parikesit AA, et al. Characterization of Hemoglobin Variants by Capillary Electrophoresis, UV-Vis, and FTIR Spectroscopy. Electrophoresis. 2025;46(16):1165-73.
248. Ellis-Guardiola K, Soule J, Clubb RT. Methods for the Extraction of Heme Prosthetic Groups from Hemoproteins. Bio Protoc. 2021;11(18):e4156.
249. Ganong WF. Circumventricular organs: definition and role in the regulation of endocrine and autonomic function. Clin Exp Pharmacol Physiol. 2000;27(5-6):422-7.
250. Achilleos A, Trainor PA. Neural crest stem cells: discovery, properties and potential for therapy. Cell Research. 2012;22(2):288-304.